NATIONAL INSTITUTE OF AEROSPACE

Influence of Finite Element Software on Energy Release Rates Computed Using the Virtual Crack Closure Technique

Ronald Krueger
National Institute of Aerospace (NIA), Hampton, Virginia

Dirk Goetze
University of Stuttgart, Stuttgart, Germany

Since its founding, NASA has been dedicated to the advancement of aeronautics and space science. The NASA Scientific and Technical Information (STI) Program Office plays a key part in helping NASA maintain this important role.

The NASA STI Program Office is operated by Langley Research Center, the lead center for NASA's scientific and technical information. The NASA STI Program Office provides access to the NASA STI Database, the largest collection of aeronautical and space science STI in the world. The Program Office is also NASA's institutional mechanism for disseminating the results of its research and development activities. These results are published by NASA in the NASA STI Report Series, which includes the following report types:

- TECHNICAL PUBLICATION. Reports of completed research or a major significant phase of research that present the results of NASA programs and include extensive data or theoretical analysis. Includes compilations of significant scientific and technical data and information deemed to be of continuing reference value. NASA counterpart of peer-reviewed formal professional papers, but having less stringent limitations on manuscript length and extent of graphic presentations.

- TECHNICAL MEMORANDUM. Scientific and technical findings that are preliminary or of specialized interest, e.g., quick release reports, working papers, and bibliographies that contain minimal annotation. Does not contain extensive analysis.

- CONTRACTOR REPORT. Scientific and technical findings by NASA-sponsored contractors and grantees.

- CONFERENCE PUBLICATION. Collected papers from scientific and technical conferences, symposia, seminars, or other meetings sponsored or co-sponsored by NASA.

- SPECIAL PUBLICATION. Scientific, technical, or historical information from NASA programs, projects, and missions, often concerned with subjects having substantial public interest.

- TECHNICAL TRANSLATION. English-language translations of foreign scientific and technical material pertinent to NASA's mission.

Specialized services that complement the STI Program Office's diverse offerings include creating custom thesauri, building customized databases, organizing and publishing research results ... even providing videos.

For more information about the NASA STI Program Office, see the following:

- Access the NASA STI Program Home Page at *http://www.sti.nasa.gov*

- E-mail your question via the Internet to help@sti.nasa.gov

- Fax your question to the NASA STI Help Desk at (301) 621-0134

- Phone the NASA STI Help Desk at (301) 621-0390

- Write to:
  NASA STI Help Desk
  NASA Center for AeroSpace Information
  7121 Standard Drive
  Hanover, MD 21076-1320

Influence of Finite Element Software on Energy Release Rates Computed Using the Virtual Crack Closure Technique

Ronald Krueger
National Institute of Aerospace (NIA), Hampton, Virginia

Dirk Goetze
University of Stuttgart, Stuttgart, Germany

October 2006

INFLUENCE OF FINITE ELEMENT SOFTWARE ON ENERGY RELEASE RATES COMPUTED USING THE VIRTUAL CRACK CLOSURE TECHNIQUE

Ronald Krueger[*] and Dirk Goetze[+]

ABSTRACT

Strain energy release rates were computed along straight delamination fronts of Double Cantilever Beam, End-Notched Flexure and Single Leg Bending specimens using the Virtual Crack Closure Technique (VCCT). The results were based on finite element analyses using ABAQUS® and ANSYS® and were calculated from the finite element results using the same post-processing routine to assure a consistent procedure. Mixed-mode strain energy release rates obtained from post-processing finite element results were in good agreement for all element types used and all specimens modeled. Compared to previous studies, the models made of solid twenty-node hexahedral elements and solid eight-node incompatible mode elements yielded excellent results. For both codes, models made of standard brick elements and elements with reduced integration did not correctly capture the distribution of the energy release rate across the width of the specimens for the models chosen. The results suggested that element types with similar formulation yield matching results independent of the finite element software used. For comparison, mixed-mode strain energy release rates were also calculated within ABAQUS®/Standard using the *VCCT for ABAQUS®* add on. For all specimens modeled, mixed-mode strain energy release rates obtained from ABAQUS® finite element results using post-processing were almost identical to results calculated using the *VCCT for ABAQUS®* add on.

1. INTRODUCTION

One of the most common failure modes for composite structures is delamination [1-4]. The remote loadings applied to composite components are typically resolved into interlaminar tension and shear stresses at discontinuities that create mixed-mode I, II and III delaminations. To characterize the onset and growth of these delaminations, the use of fracture mechanics has become common practice over the past two decades [4-6]. The total strain energy release rate, G_T, the mode I component due to interlaminar tension, G_I, the mode II component due to interlaminar sliding shear, G_{II}, and the mode III component, G_{III}, due to interlaminar scissoring shear, as shown in Figure 1, have to be calculated when a methodology based on fracture mechanics is used. In order to predict delamination onset or growth for two-dimensional problems, these calculated G components are compared to interlaminar fracture toughness properties measured over a range from pure mode I loading to pure mode II loading [7-9]. A quasi static mixed-mode fracture criterion is determined by plotting the interlaminar fracture toughness, G_c, versus the mixed-mode ratio, G_{II}/G_T, determined from data generated using Double Cantilever Beam (DCB) (G_{II}/G_T=0), End Notched Flexure (ENF) (G_{II}/G_T=1), and Mixed Mode Bending (MMB) tests of varying ratios, as shown in Figure 2 for T300/914C [10]. A curve fit of these data is performed to determine a mathematical relationship between G_c and G_{II}/G_T.

---

[*] Senior Research Scientist, National Institute of Aerospace (NIA), 100 Exploration Way, Hampton, VA 23666

[+] University of Stuttgart, Stuttgart, Germany

[11]. Failure is expected when, for a given mixed-mode ratio G_{II}/G_T, the calculated total energy release rate, G_T, exceeds the interlaminar fracture toughness, G_c. An interaction criterion incorporating the scissoring shear (mode III), however, has not yet been established. The edge-cracked torsion test (ECT) is being considered for standardization [12, 13].

The virtual crack closure technique (VCCT) is widely [14, 15] used for computing energy release rates based on results from continuum (2D) and solid (3D) finite element analyses to supply the mode separation required when using the mixed-mode fracture criterion. Although the original publication on VCCT dates back a quarter century [14], the virtual crack closure technique has only recently been implemented into ABAQUS® [16]. Currently the virtual crack closure technique (VCCT) is used mainly by scientists in universities, research institutions and government laboratories and is usually implemented in specialized codes or used in post-processing routines in conjunction with general-purpose finite element software.

Lately, an increased interest in using a fracture mechanics based approach to assess the damage tolerance of composite structures in the design phase and during certification has also renewed the interest in the virtual crack closure technique. Reliability and repeatability of results are required to ensure that methodologies based on fracture mechanics will be incorporated into the design and certification process. Computed energy release rates as shown in Figure 3 for the two-dimensional finite element analysis of a hybrid composite tapered flex-beam have shown that energy release rates computed from results obtained from different finite element codes are in good agreement [17].

The first objective of this study was to compare computed strain energy release rates using VCCT based on results obtained from three-dimensional analyses using different finite element codes. For comparison, the finite element codes ANSYS® and ABAQUS® were chosen which were run on different platforms. For this investigation, simple specimens like the double cantilever beam (DCB) specimen and the End-Notched Flexure (ENF) specimen with unidirectional layup and the Single Leg Bending (SLB) specimen with multi-directional layup were chosen for full three-dimensional finite element simulations. The specimens were modeled with different types of solid brick elements. Mixed-mode strain energy release rates were calculated using a user written post-processing routine. Computed strain energy release rates across the width of the specimens were compared with results from previous analyses [18, 19].

The second objective of this study was to test and study the implementation of the virtual crack closure technique in ABAQUS® [16]. Analyses using models of DCB and ENF specimens with unidirectional layup and models of a SLB specimen with multi-directional layup were performed. Computed mixed-mode strain energy release rates across the width of the specimens were compared with results obtained from a user written post-processing routine and with results from previous analyses [18, 19].

2. SPECIMEN DESCRIPTION

For the current numerical investigation simple specimens such as the Double Cantilever Beam (DCB), the End-Notched Flexure (ENF) and the Single Leg Bending (SLB) specimens, as shown in Figure 4, were chosen. The DCB specimen is used to determine the mode I interlaminar fracture toughness, G_{IC} (G_{II}/G_T=0), the ENF specimen is used for mode II

(G_{II}/G_T=1) fracture toughness testing. The SLB specimen was introduced for the determination of fracture toughness as a function of mixed-mode I/II ratio [20, 21]. This test may be performed in a standard three point bending fixture such as that used for the ENF test. By varying the relative thickness of the delaminated regions (t_1 and t_2) various mode mixities may be achieved. This type of specimen was chosen to study mode separation. Previously, a number of combined experimental and numerical studies of these specimens had been performed where the critical strain energy release rates were evaluated under mode I, mode II and mixed-mode conditions [18-20, 22, 23].

In general, mode I, mode II and mixed-mode tests are performed on unidirectionally reinforced laminates, which means that delamination growth occurs at a [0/0] interface and crack propagation is parallel to the fibers. For the current study, DCB and ENF specimens made of T300/1076 graphite/epoxy and unidirectional layup $[0]_{24}$ (UD24) were modeled. One SLB-specimen modeled was made of C12K/R6376 graphite/epoxy and unidirectional layup $[0]_{32}$ (UD32). Although this unidirectional layup is desired for standard test methods to characterize fracture toughness, this kind of delamination growth will rarely occur in real structures. Previously, a number of combined experimental and numerical studies on specimens with multidirectional layup were performed where the critical strain energy release rates of various interfaces were evaluated under mode I, mode II and mixed-mode conditions [20, 22, 23]. Therefore, another SLB-specimen made of C12K/R6376 graphite/epoxy with a multidirectional layup was also modeled. The stacking sequence [$\pm30/0/-30/0/30/0_4/30/0/-30/0/-30/30/_\uparrow$-30/30/0/30/0/ -30/0_4/30/0/30/0/±30] was designated D±30, where the arrow denotes the location of the delamination. The material properties are given in Table 1 and the layups modeled are summarized in Table 2.

3. ANALYSIS TOOLS
3.1 Virtual Crack Closure Technique

For delaminations in laminated composite materials where the failure criterion is highly dependent on the mixed-mode ratio (as shown in Figure 2), the virtual crack closure technique (VCCT) has been widely used for computing energy release rates [14, 15]. Results based on continuum (2-D) and solid (3-D) finite element analyses provide the mode separation required when using the mixed-mode fracture criterion.

The mode I and mode II components of the strain energy release rate, G_I, G_{II} are computed as shown in Figure 5(a) for a 2-D four-node element as an example of VCCT. The terms X'_i, Z'_i are the forces at the crack tip at nodal point i and u'_ℓ, w'_ℓ ($u'_{\ell*}$, $w'_{\ell*}$) are the displacements at the corresponding nodal points ℓ and ℓ^* behind the crack tip. For geometric nonlinear analysis where large deformations may occur, both forces and displacements obtained in the global coordinate system need to be transformed into a local coordinate system (x', z') which originates at the crack tip as shown in Figure 5(a). The local crack tip system defines the tangential (x' or mode II) and normal (z' or mode I) coordinate directions at the crack tip in the deformed configuration. The total energy release rate G_T is calculated from the individual mode components as $G_T = G_I + G_{II} + G_{III}$, where $G_{III} = 0$ for the two-dimensional case shown in Figure 5(a). The extension to 3-D is

straight forward as shown in Figure 5(b). Equations and additional details about VCCT for higher order solid elements and shell elements can be found in the literature [14, 15].

3.2 User Written VCCT Post-Processing Routines

Although the original publication on VCCT dates back a quarter century [14], the virtual crack closure technique has only recently been implemented into ABAQUS® [16]. Currently, the virtual crack closure technique (VCCT) is used mainly by scientists in universities, research institutions, government laboratories and research groups in industry who use their own user written subroutines. The subroutines may either interface directly with the finite element code during its execution, provided this option has been made available for this particular software, or operate as an entirely separate post-processing step.

3.2.1 Post-Processing Routine for ABAQUS®

The application of the virtual crack closure technique based on results from finite element analysis requires access to the element forces at nodes, the nodal point displacements and the nodal point coordinates. The flow chart, depicted in Figure 6, shows an independent post-processing routine where input data for VCCT is extracted directly from an ABAQUS® binary result file (.fil):

1. Establish interface with finite element software ABAQUS®.

2. Provide input interface to read variable problem-specific external data such as crack length, Young's modulus, etc., and control parameters such as element type, etc., which is generally not hard coded into the subroutine.

3. Create output file to store echo print of control parameters, input data, and retrieved data as well as intermediate and final results.

4. Read element forces, or forces at constraints, nodal point coordinates, and nodal displacements from binary result file (.fil).

5. Store the data retrieved in step 4 in internal common blocks and arrays for further access during the calculation.

6. Calculate area virtually closed, ΔA, using nodal point coordinates.

7. Calculate local coordinate system x', y' and z' at crack tip for geometrically nonlinear analysis and arbitrarily shaped delamination front as discussed in section 3.1 or related references [14, 15].

8.
    a. Obtain the forces at the crack tip and in front of the crack tip from the forces at element nodes by summing the forces at common nodes from elements belonging to the upper surface.

b. Obtain relative displacements between the surfaces from the nodal point displacements.

c. Transform forces and displacements to local crack tip coordinate system.

9. Calculate mixed-mode strain energy release rates using the equations given for the individual element type and correct for different element lengths and widths if necessary.

10. Repeat steps 6 through 9 for all nodes along the delamination front and write results to output file.

3.2.2 Post-Processing Routine for ANSYS Mechanics^{TM}

The basic strategy to implement VCCT in a post-processing routine is the same regardless of data retrieved from a binary data file such as the ABAQUS$^®$ .fil file or a data file in ASCII format such as a PATRAN$^®$ neutral file. The original post-processing routine to calculate energy release rates was modified to allow more flexibility. It is finite element software independent and uses three ASCII files as input which need to be provided by the user. The modified approach shown in Figure 7 can be used with any finite element software as long as the input data files required can be created. It was tested in conjunction with the finite element software ANSYS$^®$, for which a macro (*vcct-dat.mac*) was written to create the data files required. In a first step, the model data was written to the file *model.dat*. The nodal coordinates for elements at the delamination front are written to the file *topbot.dat*, the displacements and the forces are written to the file *result.dat*.

In the post-processing routine, the software specific interface to the binary output file in step 1 of the procedure became obsolete as shown in Figure 7. Major changes were also made to allow the routine to interface with the ASCII data files *model.dat*, *topbot.dat* and *result.dat* and to read the data. Additional changes were also required to allow for the conversion of special element designations unique to ANSYS$^®$ to a generic designation used in the user written post-processing routine.

3.3 VCCT for ABAQUS$^®$

Currently, *VCCT for ABAQUS$^®$* is an add-on capability to ABAQUS$^®$/Standard Versions 6.5 and 6.6 that provides a specific implementation of the virtual crack closure technique within ABAQUS$^®$. This new capability enhances ABAQUS$^®$ to solve delamination and debonding problems in composite materials. The implementation is compatible with all the features in ABAQUS$^®$ such as large-scale nonlinear, models of composite structures including continuum shells, composite materials, cohesive elements, buckling, and contact. The bond line in two-dimensional analyses or the plane of delamination in three-dimensional analyses is modeled using the existing ABAQUS$^®$/Standard crack propagation capability based on the contact pair capability. Additional element definitions are not required, and the underlying finite element mesh and model does not have to be modified [16].

Beyond simple calculation of the mixed-mode strain energy release rates at the crack tip or

along the delamination front, the implementation also offers a crack propagation capability in ABAQUS®. It is implied that the energy release rate at the crack tip is calculated at the end of a converged increment. Once the energy release rate exceeds the critical strain energy release rate (including the user-specified mixed-mode criteria as shown in Figure 2), the node at the crack tip is released in the following increment, which allows the crack to advance. To avoid sudden loss of stability when the crack tip is advanced, the force at the crack tip before advance is released gradually during succeeding increments in such a way that the force is brought to zero no later than the time at which the next node along the crack path begins to open. The propagation capability was not tested since it exceeded the scope of the current study.

4 FINITE ELEMENT MODELING AND ANALYSIS
4.1 Analysis Procedure
The goal of this investigation was to compare computed strain energy release rates based on results obtained from different finite element codes. For comparison, the finite element codes ANSYS® and ABAQUS® were chosen. The input files for both codes were generated by a user written FORTRAN routine (`genmesh.f`) as shown in the flow chart of Figure 8. This approach was used to avoid user interference with input data and ensure that nodal point coordinates, element topology and material data as well as load and boundary conditions of the models were identical for both codes. Results from ABAQUS® were saved in the binary .fil results file, results from ANSYS® were written to three output files (`model.dat, results.dat` and `topbot.dat`) using a user written ANSYS® macro as mentioned above. For both codes, mixed-mode strain energy release rates were calculated from finite element results using the same user written post-processing routine for VCCT to assure a consistent procedure. For comparison, mixed-mode strain energy release rates were also calculated within ABAQUS®/Standard using the *VCCT for ABAQUS®* add on mentioned above.

4.2 Finite Element Selection
To study the influence of element selection on the computed mixed-mode strain energy release rates, several three-dimensional solid element types were used in the past to model the specimens [18, 19]. In ABAQUS®, the use of standard solid eight-node brick element C3D8, incompatible mode element C3D8I, reduced integration element C3D8R as well as solid twenty-node hexahedral elements C3D20 and reduced integration element C3D20R was studied [19]. Shear locking is common in first-order, fully integrated elements, such as C3D8, that are subject to bending. The numerical formulation of this element gives rise to shear strains that do not really exist. Therefore, these elements are too stiff in bending, and many elements over the thickness are required to obtain acceptable results. Elements where a lower-order, reduced integration is used to form the element stiffness such as the C3D8R and C3D20R elements usually provide more accurate results in bending and reduce running time. Incompatible mode elements, such as C3D8I are also recommended for bending and contact problems. In these elements, internal deformation modes are added to the standard displacement modes of the element in order to eliminate the parasitic shear stresses that occur in bending [24]. The use of

continuum shell elements was also investigated. The continuum shell elements SC8R provided in ABAQUS® allow the user to discretize the entire three-dimensional body. The elements look like three-dimensional solids from a modeling standpoint and have only displacement degrees of freedom. The continuum shell elements can be stacked to provide more refined through-thickness response. Due to the kinematic and constitutive formulation of the element and the first-order layer-wise composite theory used for layered elements, the continuum shell elements appear attractive for modeling [24].

Three different eight-node elements were chosen from the ANSYS® element library [25, 26]. The solid elements SOLID45, SOLID46, and SOLID185 were used for three-dimensional modeling of the specimen. Analyses with elements SOLID45 and SOLID46 can be performed with extra displacement shapes. The element formulation introduces extra internal degrees of freedom (inaccessible to ANSYS® users) to modify the displacement/velocity gradient tensor. All internal degrees of freedom are introduced automatically at the element level and are condensed. Element SOLID46 additionally allows up to 250 different material layers. Element SOLID185 does not have extra shapes and therefore can exhibit shear locking in bending types of applications. In such situations, the use of a uniform reduced integration technique with hourglass stiffness for controlling hourglass modes is recommended (SOLID185R). which is also available for element SOLID45 (SOLID45R). The analysis, however, cannot capture the bending behavior with a single layer of elements. For example, in the case of a fixed-end cantilever with a lateral point load four elements over the thickness are usually recommended. Element 185 also has an enhanced strain mode (185E). This mode prevents shear locking in bending-dominated problems and volumetric locking in nearly incompressible cases.

Two twenty-node elements were chosen from the ANSYS® element library. The solid elements used in this study are 95 and 186 which are higher order versions of the 45 and 185 types mentioned above and exhibit quadratic displacement behavior. The elements can tolerate irregular shapes without as much loss of accuracy and are well suited to model curved boundaries. Element 186 is available as a structural solid and layered solid [25, 26].

4.3 Finite Element Models

Typical three-dimensional finite element models of double cantilever beam (DCB), End-Notched Flexure (ENF) and Single Leg Bending (SLB) specimens are shown in Figures 9 through 14. For the DCB and SLB specimen made with unidirectional layup only half of the specimen width (*B/2*) was modeled as shown in Figure 9, and symmetry conditions were applied in the *xz*-plane (*y*=0). Along the length, all models were divided into different sections with different mesh refinement as shown in Figure 9(a). A refined mesh of length *d*=5 mm with 20 elements as used for the UD24 layup is shown in the detail of Figure 9(b), This section length, *d*, had been selected in previous studies [18, 19] and was also used during the current investigations. Across the width, all models were divided into a center section of width, *i*, and a refined edge section, *j*, to capture local edge effects and steep gradients. These sections appear as dark areas in the full view of the specimen as shown in Figure 9. The specimens with unidirectional layup were modeled with six elements through the specimen thickness (*2h*) as shown in the detail of Figure 9(b). The delamination was modeled as a discrete discontinuity in

the center of the specimen, with separate, unconnected nodes (with identical coordinates) on the upper and lower surfaces of the delaminated section. For the DCB with unidirectional layup, finite element meshes were also developed to model the full width B as shown in Figures 10 and 11. A model with a refined mesh near the edges is shown in Figure 10(a) (j=1.0 mm, 8 elements) and a model with uniform mesh across the width is shown in Figure 10(b). The difference in the model shown in Figure 11 is a refined zone along the length near the delamination front (d=10 mm, 20 elements).

For the analysis of the ENF specimen, a model with refined edges was used as shown in Figure 12. Interpenetration of the cantilever arms was prevented by introducing multi-point constraints in the plane of delamination along a line of nodes above the support as discussed in a previous study [19]. The use of multi-point constraints appears advantageous as less modeling effort is required, and a computationally expensive contact analysis is avoided.

For the SLB specimen, a length of d=3.0 mm with 12 elements in the vicinity of the delamination front was chosen as shown in Figure 13. This section length, d, had been selected in previous studies [18] and remained unchanged during the current investigations. For the specimen with D±30 layup, two plies on each side of the delamination were modeled individually using one element for each ply as shown in the detail of Figure 13. The adjacent four plies were modeled by one element with material properties smeared using the rule of mixtures [27, 28]. This procedure did not calculate the full A-B-D stiffness matrix contributions of the plies [27, 28]; however, it appeared suitable to enforce a reasonable model size. The adjacent element extended over the four 0˚ plies. The six outermost plies were modeled by one element with smeared material properties. Additionally, two models with a finer mesh across the width were created a shown in Figure 14. A model with a refined mesh near the edges is shown in Figure 14(a) (j=2.0 mm, 8 elements) and a model with uniform mesh across the width is shown in Figure 14(b).

5. COMPUTED MIXED-MODE ENERGY RELEASE RATES
5.1 Results Obtained from ABAQUS® and ANSYS® Using Post-Processing

The first objective of this study was to compare computed strain energy release rates using VCCT based on results obtained from three-dimensional analyses using different finite element codes. For comparison, the finite element codes ANSYS® and ABAQUS® were chosen. For this investigation, double cantilever beam (DCB) specimens and the Single Leg Bending (SLB) specimens with unidirectional and multi-directional layup were chosen for full three-dimensional finite element simulations [26]. Mixed-mode strain energy release rates were calculated using a user written post-processing routine as discussed above. Computed strain energy release rates across the width of the specimens were compared with results from previous analyses [18, 19].

5.1.1 Mode I Energy Release Rates Distribution Across the Width of a DCB Specimen

The computed mode I strain energy release rate values across the width of a DCB specimen with unidirectional layup were normalized with respect to the value from beam theory,

$$G_{\text{I,beam}}(a) = \frac{12 \cdot a^2 \cdot P^2}{B^2 \cdot h^3 \cdot E_1}$$

where a denotes the delamination length, P the external load, B the specimen width, h the thickness of the cantilever arms as shown in Figure 4 and E_1 the modulus of elasticity [8]. The normalized values were plotted versus the normalized width, y/B, of the specimen as shown in Figure 15 for results obtained from ABAQUS®. Strain energy release rates obtained from the model shown in Figure 9 using C3D8I, C3D20 and C3D20R elements are in excellent agreement with the values from previous analyses, which were added for comparison [18]. The mode I strain energy release rate is fairly constant in the center part of the specimen progressively decreasing towards the edges as explained earlier which will cause the initial straight front to grow into a curved front as explained in detail in the literature [29-32]. As expected, the mode II and mode III strain energy release rates were computed to be nearly zero and hence are not shown. The model made of C3D8 elements yielded results, which did not correctly capture the decrease of the mode I strain energy release rate towards the edge. The mode I strain energy release rate computed from the model made of C3D8R elements was noticeably higher across the entire width compared to the other results.

The results of a brief mesh refinement study for the standard eight-node brick element (C3D8) and eight node brick elements with reduced integration and hourglass control (C3D8R) are shown in Figures 16 to 18 for a uniform mesh across the width of the specimen. Two elements over the thickness of one arm were used to compute the distributions shown in Figure 16. Three elements over the thickness of one arm yielded the results in Figure 17, and four elements over the thickness of one arm yielded the results shown in Figure 18. With increasing number of elements, the strain energy release rates distributions approach the reference results. Hence, a minimum number of four elements across the thickness is recommended when using these elements. Results obtained from models using eight node incompatible mode elements were included in the plots of Figures 16 to 18. The distributions suggest that as few as two elements across the thickness are sufficient to obtain a good agreement with reference results.

Mode I energy release rates obtained from the model shown in Figure 9 using the finite element software ANSYS® are shown in Figure 19 for all element types used in this study. Strain energy release rates obtained using SOLID186, SOLID95, SOLID45, SOLID46 and SOLID185E type elements were in excellent agreement with the values from previous analyses, which were added for comparison [18]. The model made of SOLID185 elements yielded results, which did not correctly capture the decrease of the mode I strain energy release rate towards the edge. The mode I strain energy release rate computed from the model made of SOLID45R and SOLID185R elements was noticeably higher across the entire width compared to the other results.

Strain energy release rates obtained from analyses using ABAQUS® and ANSYS® are plotted in Figures 20 to 23 for corresponding element types and compared to results obtained from previous analyses [18]. For both finite element codes, mode I energy release rates obtained from the models using higher order twenty-node elements are in excellent agreement with the

values from previous analyses as shown in Figure 20. The models made of standard eight node brick elements yielded results that did not correctly capture the decrease of the mode I strain energy release rate towards the edge as shown in Figure 21. The mode I strain energy release rate computed from models made of eight node brick elements with reduced integration were noticeably higher across the entire width compared to the other results obtained from previous analyses [18] as shown in Figure 22. For both finite element codes, mode I energy release rates obtained from the models using solid eight node incompatible mode elements are in excellent agreement with the values from previous analyses as shown in Figure 23. The results obtained from the model shown in Figure 9 suggest that element types with similar formulation yield matching results independent of the software used. Further, mode I energy release rates obtained from the models using higher order twenty-node elements and eight node incompatible mode elements are in excellent agreement with the values from previous analyses.

5.1.2 Mixed-Mode Energy Release Rate Distributions Across the Width of a Unidirectional SLB Specimen

For this investigation, the symmetry of the SLB specimen was taken into account, and only one half of the specimen width $B/2$ was modeled as shown in Figure 9. The finite element model is basically identical to the one used for the DCB specimens discussed in the previous section, except for the boundary conditions. The influence of element selection on the computed mixed-mode strain energy release rates was studied using ABAQUS® C3D8, C3D8I, C3D8R, C3D20 and C3D20R type elements as well as ANSYS® SOLID45 and 45R, SOLID185, 185R and 185E and SOLI46, SOLID95 and SOLID186 type elements [26].

In Figures 24 to 26, the computed mode I, II and mode III strain energy release rates from ABAQUS® analyses are plotted versus the normalized width, y/B, of the specimen. Computed strain energy release rates obtained from models using C3D8I, C3D20 and C3D20R elements are in excellent agreement with the values from previous analyses [18]. As shown in Figure 24, the mode I strain energy release rate is fairly constant in the center part of the specimen and progressively decreases towards the edges as previously discussed for the DCB specimen. The model made of C3D8 elements yields results that do not correctly capture the decrease of the mode I strain energy release rate towards the edge. The values computed from the model made of C3D8R elements appear excessively high. The mode II strain energy release rate as shown in Figure 25 is fairly constant across almost the entire width of the specimen, peaking in the immediate vicinity of the edges. As shown in Figure 26, the mode III contribution is zero in the center of the specimen peaking to about only 8% of G_{II} at the edges. The model made of C3D8 elements yields results that do not correctly capture the mode II and III distribution. The mode II values computed from the model made of C3D8R elements appear excessively high across the entire width of the specimen. These observations support the results obtained from the study of the UD24 DCB specimen discussed above. Compared to the model made of C3D20 elements, the models made of C3D8I elements yield nearly the same results and provide a reduced model size.

Computed mode I, II and mode III strain energy release rates from ANSYS® analyses are plotted in Figures 27 to 29 versus the normalized width, y/B, of the specimen. Computed strain energy release rates obtained from models using SOLID186, SOLID95, elements are in excellent

agreement with the values from a previous analysis models [18] as shown in Figure 27. The model made of SOLID185 elements yields results that do not correctly capture the decrease of the mode I strain energy release rate towards the edge. The values computed from the model made of SOLID45R and SOLID185R elements appear excessively high. The mode II strain energy release rate, as shown in Figure 28, is fairly constant across almost the entire width of the specimen, peaking in the immediate vicinity of the edges. As shown in Figure 29, the mode III contribution is zero in the center of the specimen peaking to about only 8% of G_{II} at the edges. The model made of SOLID185 elements yields results that do not correctly capture the mode II and III distribution. The mode II values computed from the model made of SOLID45R and SOLID185R elements appear excessively high across the entire width of the specimen. These observations support the results obtained from the study of the UD24 DCB specimen discussed above. Compared to the models made of SOLID186, SOLID95 type elements, the models made of SOLID45, SOLID46 and SOLID185E type elements yield nearly the same results that are also in excellent agreement with reference results [18].

Mixed-mode strain energy release rates obtained from analyses using ABAQUS® and ANSYS® are plotted in Figures 30 to 41 for corresponding element types and compared to results obtained from previous analyses [18]. For both finite element codes, mode I, II and III energy release rates obtained from the models using higher order twenty-node elements are in excellent agreement with the values from previous analyses as shown in Figures 30 to 32. The models made of standard eight node brick elements yielded results that did not correctly capture the distribution of the energy release rates across the width as shown in Figure 33 to 35 for the individual fracture modes. The strain energy release rates computed from models made of eight node brick elements with reduced integration were noticeably higher across the entire width compared to the other results obtained from previous analyses [18] as shown in Figure 36 to 38 for the individual fracture modes. For both finite element codes, mixed-mode energy release rates obtained from the models using solid eight node incompatible mode elements are in excellent agreement with the values from previous analyses as shown for the individual models in Figures 39 to 41. The results suggest that element types with similar formulation yield matching results independent of the finite element software used. Further energy release rates obtained from the models using higher order twenty-node elements and eight node incompatible mode elements are in excellent agreement with the values from previous analyses. Therefore, solid eight node incompatible mode type elements (ABAQUS® C3D8I and ANSYS® SOLID46) were chosen for the following study.

5.1.3 Mixed-Mode Energy Release Rate Distributions Across the Width of a Multidirectional SLB Specimen

In this study, SLB specimens with a multidirectional layup (D±30) were modeled entirely with solid elements as shown in Figure 13. The model was made of eight node ABAQUS® C3D8I or ANSYS® SOLID46 elements. It was shown above that compared to the models made of twenty-node elements, the models made of incompatible mode elements yielded nearly the same results and provide a reduced model size. Therefore, these element types were chosen for this and the following studies. Section widths and mesh sizes used in the current investigation

were taken from a previous study where the effect of mesh size across the width on computed mixed-mode energy release had been investigated [18, 19].

The computed mode I, II and mode III strain energy release rates, as shown in Figures 42 to 44, were compared with values from previous analyses [18]. As shown in Figure 42, the zone with a constant G_I distribution in the center becomes smaller compared to the UD32 case and the decrease towards the edges is more pronounced. The decrease is caused by increased anticlastic bending due to the lower values of bending rigidities in the individual arms. Results obtained from ABAQUS® and ANSYS® are in excellent agreement and also agree well with the reference results. The mode II and mode III distributions are shown in Figures 43 and 44. The mode II strain energy release rate is fairly constant across almost the entire width of the specimen and peaks near the edges accompanied by local mode III contribution. Compared to the UD32 layup these peaks become more visible for specimens with the D±30 layup caused by increased anticlastic bending. Results obtained from ABAQUS® follow closely the distributions from the reference results. Results obtained from ANSYS® are in good agreement in the center of the specimen and also peak towards the edges, however values for *y/B< 0* are below and for *y/B>0* above values from ABAQUS® and published the reference values [18].

5.2 Results Obtained from ABAQUS® Using Post-Processing and *VCCT for ABAQUS*®

The second objective of this study was to test and study the implementation of the virtual crack closure technique in ABAQUS® [16]. Analyses using models of DCB and ENF specimens with unidirectional layup and models of a SLB specimen with multi-directional layup were performed. Computed mixed-mode strain energy release rates across the width of the specimens were compared with results obtained from a user written post-processing routine and with results from previous analyses [18, 19].

5.2.1 Mode I Energy Release Rates Distribution Across the Width of a DCB Specimen

Strain energy release rates were computed from finite element results obtained from the model of a full specimen as shown in Figure 10(a) using C3D8I elements. The incompatible mode elements (C3D8I) were chosen since models consistently yielded the best results in the studies described above and were least sensitive to mesh refinement. The computed mode I strain energy release rate values across the width of a DCB specimen with unidirectional layup were normalized with respect to the value from beam theory as above and plotted versus the normalized width, *y/B*, of the specimen as shown in Figure 45. Plotted are results obtained for different load increments from *VCCT for ABAQUS*® and from the user written post-processing routine as shown in the flow chart of Figure 8. Strain energy release rates obtained from both methods are practically identical across the entire width and for all load increments.

Additional analyses were performed using models shown in Figures 10 and 11 which allowed a discretization study of the effect of different mesh densities as well as mesh transition from coarse in the center to fine at edge. The results plotted in Figure 46 indicate that irrespective of mesh density, energy release rates obtained from *VCCT for ABAQUS*® are almost identical to results obtained through post-processing.

Analyses were repeated with models where the new continuum shell element SC8R was used. The computed mode I strain energy release rates are shown in Figure 47 for a uniform mesh across the width and a mesh where the edge region had been refined as shown in Figure 10. For both models, energy release rates obtained from *VCCT for ABAQUS*® are almost identical to results obtained through post-processing. The results obtained from the model with a uniform mesh across the width are in good agreement with previous results, which were included for comparison [18]. The model made of SC8R elements however yields different results in the refined region near the edge of the specimen when a non-uniform mesh is used. The cause is related to the element formulation and the associated problem has been fixed by ABAQUS®. After solving the problem, ABAQUS® provided a computed mode I strain energy release rate distribution obtained from the non-uniform mesh, which is in good agreement with previous results. The problem has been fixed for ABAQUS®/Standard 6.6.2 and higher.

5.2.2 Mode II Energy Release Rates Distribution Across the Width of an ENF Specimen

For this investigation, the entire ENF specimen was modeled across the width as shown in Figure 12. Incompatible mode elements (C3D8I) were chosen since models consistently yielded the best results in the studies described above and were least sensitive to mesh refinement. In Figure 48, the computed mode II and mode III strain energy release rates are normalized with the reference value, $G_{II,beam}$, from classical beam theory (not accounting for transverse shear)

$$G_{II,beam}(a) = \frac{9 \cdot a^2 \cdot P^2}{16 \cdot B^2 \cdot h^3 \cdot E_1} \quad .$$

Here, a denotes the delamination length, P the external load, B the specimen width, h the thickness of the cantilever arms as shown in Figure 4 and E_1 the modulus of elasticity. The results are plotted versus the normalized width, y/B, of the specimen. The mode II strain energy release rate is fairly constant across almost the entire width of the specimen, peaking in the immediate vicinity of the edges. The mode III contribution is zero in the center of the specimen peaking to about only 5% of $G_{II,beam}$ at the edges. The computed G_I values are nearly zero and therefore are not shown. The results confirm that energy release rates obtained from VCCT for ABAQUS® are almost identical to results obtained through post-processing.

5.2.3 Mixed-Mode Energy Release Rate Distributions Across the Width of a Multidirectional SLB Specimen

For the investigation of the SLB specimen with multidirectional layup (D±30), the finite element models shown in Figures 13 and 14 were used. The model was made of eight node ABAQUS® incompatible mode C3D8I elements. The computed mode I, II and III strain energy release rate distributions across the width of the specimen are shown in Figures 49 to 51. The zone with a constant G_I distribution in the center is smaller compared to the SLB specimen with unidirectional layup discussed earlier, and the decrease towards the edges is more pronounced as shown in Figure 49. The decrease is caused by increased anticlastic bending due to the lower values of bending rigidities in the individual arms. The mode II distribution, as shown in Figures 50, is fairly constant across almost the entire width of the specimen and peaks near the

edges. The mode III contribution is zero in the center of the specimen peaking at the edges as shown in Figure 51. Compared to the unidirectional layup (UD32), these peaks become more visible for specimens with the multidirectional layup (D±30) caused by increased anticlastic bending. The results plotted in Figure 49 to 51 indicate that irrespective of mesh size mixed-mode energy release rates obtained from *VCCT for ABAQUS*® are almost identical to results obtained through post-processing.

6. SUMMARY AND CONCLUDING REMARKS

Simple fracture toughness specimens such as the Double Cantilever Beam (DCB) specimen and the End-Notched Flexure (ENF) specimen with unidirectional layup and the Single Leg Bending (SLB) specimen with unidirectional and multi-directional layup were modeled with full three-dimensional solid finite elements and analyzed using the finite element codes ANSYS® and ABAQUS®. Model data such as nodal point coordinates, element topology and material data as well as load and boundary conditions were generated using a user written routine to guarantee that the models were identical for both codes and to avoid interference with input data. Different element types were used to model the specimens. Delaminations were modeled as discrete discontinuities. Strain energy release rates were calculated along a straight front using the virtual crack closure technique. For finite element results based on ABAQUS® and ANSYS®, mixed-mode strain energy release rates were calculated from finite element results using the same post-processing routine to assure a consistent procedure. For comparison, mixed-mode strain energy release rates were also calculated within ABAQUS®/Standard using the *VCCT for ABAQUS*® add on.

Mixed-mode strain energy release rates obtained from post processing ANSYS® and ABAQUS® finite element results were in good agreement with results from previous analyses for all specimens modeled. Compared to previous studies, the models made of solid twenty-node hexahedral elements (ABAQUS® types C3D20 and C3D20R with reduced integration, ANSYS® types SOLID95 and SOLID186) and solid eight-node incompatible mode elements (ABAQUS® type C3D8I, ANSYS® types SOLID45, SOLID46 and SOLID185E) yielded excellent results. The models made of standard brick elements (ABAQUS® type C3D8, ANSYS® type SOLID185) yielded results, which were in agreement but compared to reference results did not correctly capture the distribution of the energy release rate across the width of the specimen for the model chosen. The values computed from the model made of elements with reduced integration (ABAQUS® type C3D8R, ANSYS® types SOLID45R and SOLID185R) were also in good agreement however appeared consistently higher than the reference results. The results suggest that element types with similar formulation yield matching results independent of the finite element software used.

For all specimens modeled, mixed-mode strain energy release rates obtained from ABAQUS® finite element results using post processing were almost identical to results calculated within ABAQUS®/Standard using the *VCCT for ABAQUS*® add on. For identical models, almost identical results were computed which indicates that the post-processing routine is redundant and may be entirely replaced by the *VCCT for ABAQUS*® routine. The results also

14

imply that results computed by the *VCCT for ABAQUS®* routine can readily be compared to existing results computed previously using a post-processing routine.

ACKNOWLEDGEMENTS

REFERENCES

[1]   A.C. Garg, *Delamination - A Damage Mode in Composite Structures*, Eng. Fracture Mech., vol. 29, pp. 557-584, 1988.

[2]   V.V. Bolotin, *Delaminations in Composite Structures: Its origin, Buckling, Growth and Stability*, Composites Part B: Engineering, vol. 27B, pp. 129-145, 1996.

[3]   T.E. Tay, *Characterization and Analysis of Delamination Fracture in Composites - An Overview of Developments from 1990 to 2001*, Applied Mechanics Reviews, vol. 56, pp. 1-32, 2003.

[4]   T.K. O'Brien, *Characterization of Delamination Onset and Growth in a Composite Laminate*, in Damage in Composite Materials, ASTM STP 775,: American Society for Testing and Materials, 1982, pp. 140-167.

[5]   T.K. O'Brien, *Fracture Mechanics of Composite Delamination*, in ASM Handbook, Volume 21, Composites: ASM International, 2001, pp. 241-245.

[6]   R.H. Martin, *Incorporating Interlaminar Fracture Mechanics into Design*, in International Conference on Designing Cost-Effective Composites: IMechE Conference Transactions, London, U.K., 1998, pp. 83-92.

[7]   *ASTM D 6671-01, Standard Test Method for Mixed Mode I-Mode II Interlaminar Fracture Toughness of Unidirectional Fiber Reinforced Polymer Matrix Composites*, in Annual Book of ASTM Standards, vol. 15.03: American Society for Testing and Materials, 2000.

[8]   *ASTM D 5528-94a, Standard Test Method for Mode I Interlaminar Fracture Toughness of Unidirectional Fiber-Reinforced Polymer Matrix Composites*, in Annual Book of ASTM Standards, vol. 15.03: American Society for Testing and Materials, 2000.

[9]   T.K. O'Brien, *Composite Interlaminar Shear Fracture Toughness, G_{IIc}: Shear Measurement or Sheer Myth ?*, in Composite Materials: Fatigue and Fracture, Seventh Volume, ASTM STP 1330, 1998, pp. 3-18.

[10]   M. König, R. Krüger, K. Kussmaul, M. v. Alberti, and M. Gädke, *Characterizing Static and Fatigue Interlaminar Fracture Behaviour of a First Generation Graphite/Epoxy Composite*, in Composite Materials: Testing and Design - (13th Vol.), ASTM STP 1242, S.J. Hooper, Ed.: American Society for Testing and Materials, 1997, pp. 60-81.

[11]   M.L. Benzeggagh and M. Kenane, *Measurement of Mixed-Mode Delamination Fracture Toughness of Unidirectional Glass/Epoxy Composites with Mixed-Mode Bending Apparatus*, Composites Science and Technology, vol. 56, pp. 439-449, 1996.

[12]   S.M. Lee, *An Edge Crack Torsion Method for Mode III Delamination Fracture Testing*, J. of Composite Technology and Research., pp. 193-201, 1993.

[13]   J.G. Ratcliffe, *Characterization of the Edge Crack Torsion (ECT) Test for Mode III Fracture Toughness Measurement of Laminated Composites*, NASA/TM-2004-213269 September 2004 2004.

[14]   E.F. Rybicki and M.F. Kanninen, *A Finite Element Calculation of Stress Intensity Factors by a Modified Crack Closure Integral*, Eng. Fracture Mech., vol. 9, pp. 931-938, 1977.

[15]   R. Krueger, *Virtual Crack Closure Technique: History, Approach and Applications*, Applied Mechanics Reviews, vol. 57, pp. 109-143, 2004.

[16]   *VCCT for ABAQUS - User's Manual*, ABAQUS 2005.

[17]   G.B. Murri, J.R. Schaff, and A.L. Dobyns, *Fatigue Life Analysis of Tapered Hybrid Composite Flexbeams*, presented at ICCM-14, San Diego, 2003.

[18]   R. Krüger, *Three Dimensional Finite Element Analysis of Multidirectional Composite DCB, SLB and ENF Specimens*, Institute for Statics and Dynamics of Aerospace Structures, University of Stuttgart ISD-Report No. 94/2, 1994.

[19]   R. Krueger and T.K. O'Brien, *A Shell/3D Modeling Technique for the Analysis of Delaminated Composite Laminates*, NASA/TM-2000-210287, ARL-TR-2207, June 2000.

[20]   B.D. Davidson, R. Krüger, and M. König, *Three Dimensional Analysis of Center Delaminated Unidirectional and Multidirectional Single Leg Bending Specimens*, Composites Science and Technology, vol. 54, pp. 385-394, 1995.

[21]   A. Pieracci, B.D. Davidson, and V. Sundararaman, *Nonlinear Analyses of Homogeneous, Symmetrically Delaminated Single Leg Bending Specimens*, Journal Composite Tech. Res., vol. 20, pp. 170-178, 1998.

[22]   B.D. Davidson, R. Krüger, and M. König, *Effect of Stacking Sequence on Energy Release Rate Distributions in Multidirectional DCB and ENF Specimens*, Eng. Fracture Mech., vol. 55, pp. 557-569, 1996.

[23]   B.D. Davidson, R. Krüger, and M. König, *Three Dimensional Analysis and Resulting Design Recommendations for Unidirectional and Multidirectional End-Notched Flexure Tests*, J. Composite Materials, vol. 29, pp. 2108-2133, 1995.

[24]   *ABAQUS 6.5, Analysis User's Manual, Volume IV: Elements*, ABAQUS 2005.

[25]   *ANSYS Elements Reference*, ANSYS Inc., Canonsburg, PA 15317 2005.

[26]   D. Goetze, *Bruchanalyse von Faserverbundwerkstoff-Proben mit Finiten Elementen und der Virtuellen Rißschließungsmethode (Computational Fracture Analysis of Composite Specimens Based on Three-Dimensional Finite Element Analysis and the Virtual Crack Closure Technique)*, Institut fuer Statik und Dynamik der Luft- und Raumfahrtkonsturktionen, Universitaet Stuttgart, Germany, Diplomarbeit 2003.

[27]   S.W. Tsai, *Theory of Composite Design*: Think Composites, 1992.

[28]   S.W. Tsai and H.T. Hahn, *Introduction to Composite Materials*: Technomic Publishing Co., Inc., 1980.

[29]   I.S. Raju, K.N. Shivakumar, and J.H. Crews Jr., *Three-Dimensional Elastic Analysis of a Composite Double Cantilever Beam Specimen*, AIAA J., vol. 26, pp. 1493-1498, 1988.

[30]   R. Krüger, M. König, and T. Schneider, *Computation of Local Energy Release Rates Along Straight and Curved Delamination Fronts of Unidirectionally Laminated DCB- and ENF - Specimens*, in Proceedings of the 34th AIAA/ASME/ASCE/AHS/ASC SSDM

Conference, La Jolla, CA: American Institute of Aeronautics and Astronautics, Washington, 1993, pp. 1332-1342.

[31] B.D. Davidson and R.A. Schapery, *Effect of Finite Width on Deflection and Energy Release Rate of an Orthotropic Double Cantilever Specimen*, J. Composite Mat., vol. 22, pp. 640--656, 1988.

[32] B.D. Davidson, *An Analytical Investigation of Delamination Front Curvature in Double Cantilever Beam Specimens*, J. Composite Mat., vol. 24, pp. 1124--1137, 1990.

Table 1.

Material Properties.

T300/1076 Unidirectional Graphite/Epoxy Prepreg		
E_{11} = 139.4 GPa	E_{22} = 10.16 GPa	E_{33} = 10.16 GPa
v_{12} = 0.30	v_{13} = 0.30	v_{23} = 0.436
G_{12} = 4.6 GPa	G_{13} = 4.6 GPa	G_{23} = 3.54 GPa
C12K/R6376 Unidirectional Graphite/Epoxy Prepreg		
E_{11} = 146.9 GPa	E_{22} = 10.6 GPa	E_{33} = 10.6 GPa
v_{12} = 0.33	v_{13} = 0.33	v_{23} = 0.33
G_{12} = 5.45 GPa	G_{13} = 5.45 GPa	G_{23} = 3.99 GPa

The material properties are given with reference to the ply coordinate axes where index 11 denotes the ply principal axis that coincides with the direction of maximum in-plane Young's modulus (fiber direction). Index 22 denotes the direction transverse to the fiber in the plane of the lamina and index 33 the direction perpendicular to the plane of the lamina.

Table 2.

Stacking Sequence.

Layup-ID	Stacking Sequence	Material
UD24	$[0]_{24}$	T300/1076
UD32	$[0]_{32}$	C12K/R6376
D±30	$[\pm30/0/\text{-}30/0/30/0_4/30/0/\text{-}30/0/\text{-}30/30/_\uparrow\text{-}30/30/30/0/30/0/\text{-}30/0_4/\text{-}30/0/30/0/\pm30]$	C12K/R6376

Interlaminar tension
Mode I

Interlaminar sliding shear
Mode II

Interlaminar scissoring shear
Mode II

Figure 1: *Fracture Modes.*

DCB, Mode I

MMB, Mode I and II

ENF, Mode II

$G_{IIc} = 493.6$

G_C, J/m^2

$G_{Ic} = 170.3$

curve fit: $G_c = G_{Ic} + (G_{IIc} - G_{Ic})(G_{II}/G_T)$

$= 1.62$

○ experimental data
● mean values

Mixed Mode Ratio G_{II}/G_T
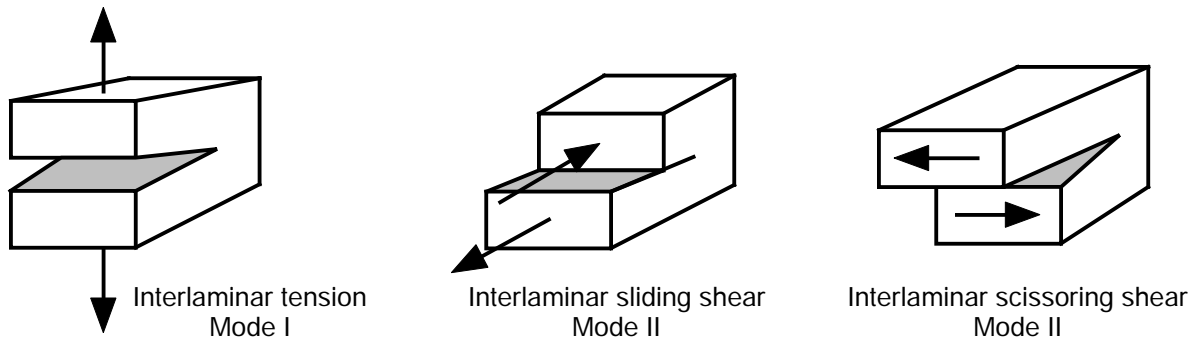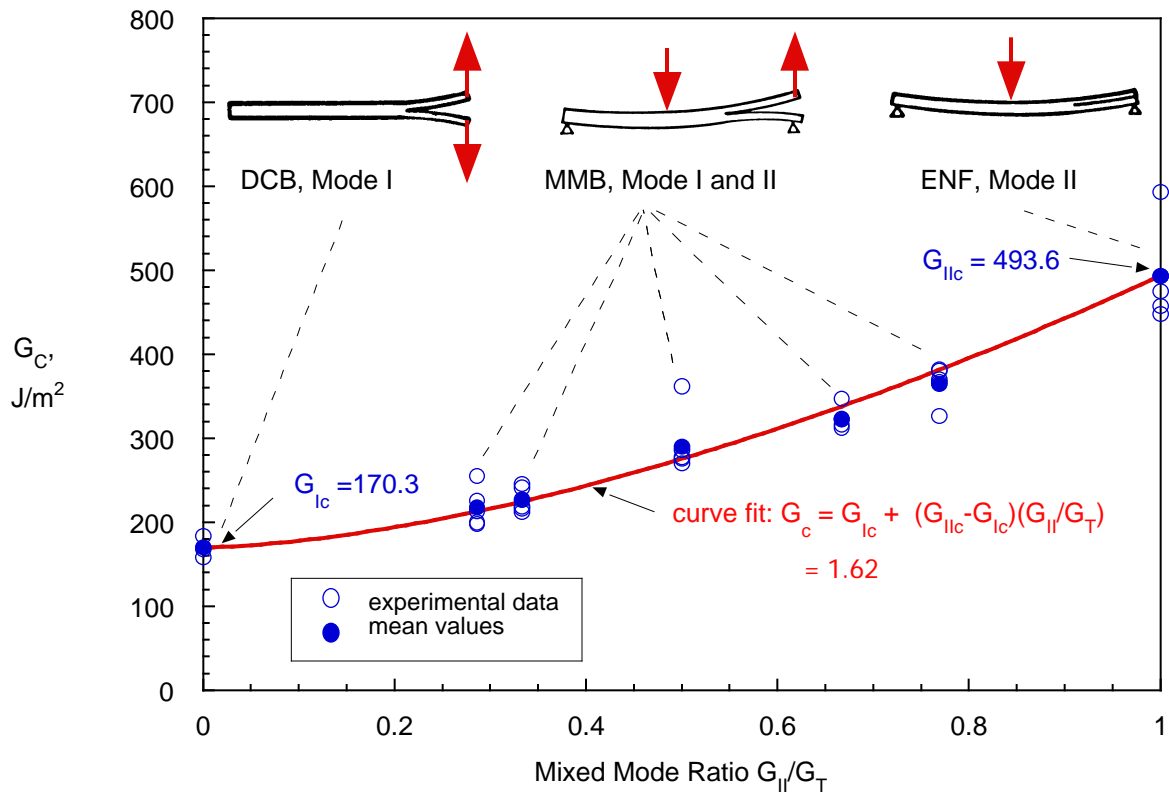
Figure 2. *Mixed-mode fracture criterion for T300/914C*
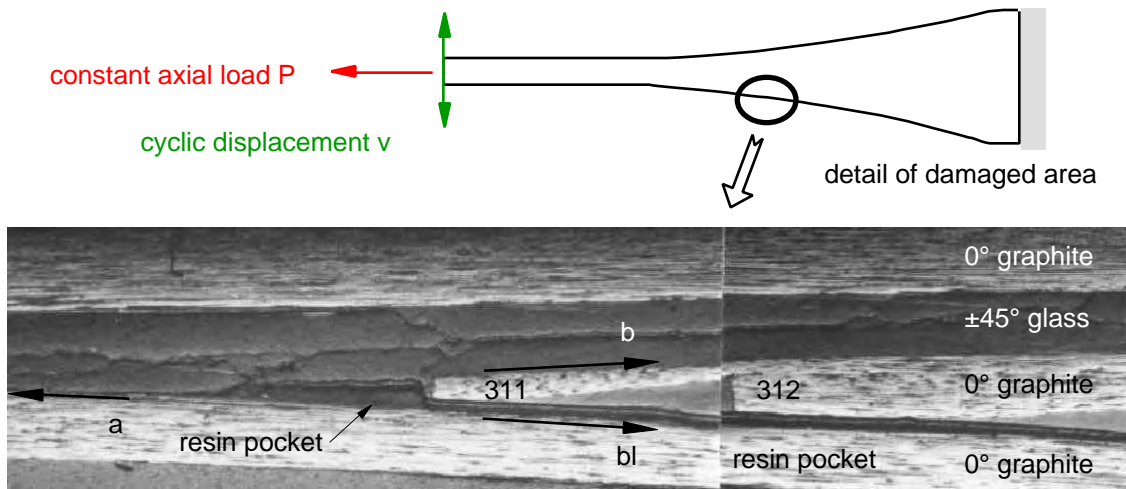
(a) Flexbeam specimen with loading and micrograph of observed damage
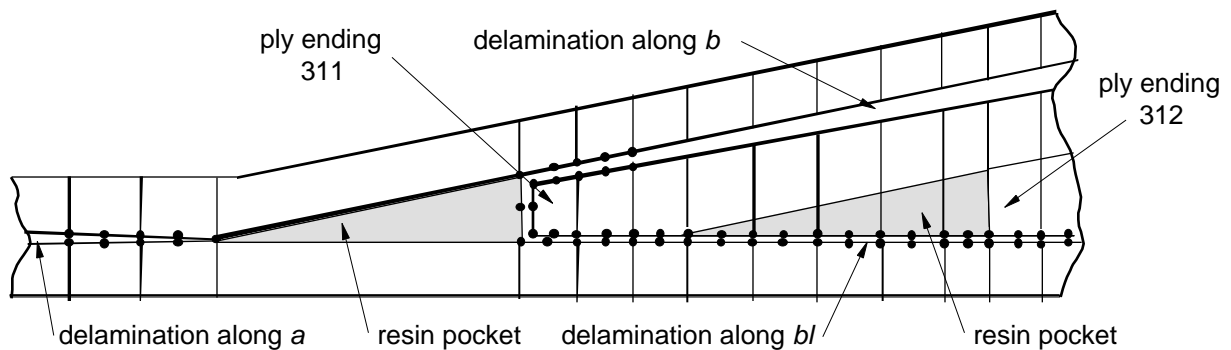
(b) Finite element mesh of the damaged zone
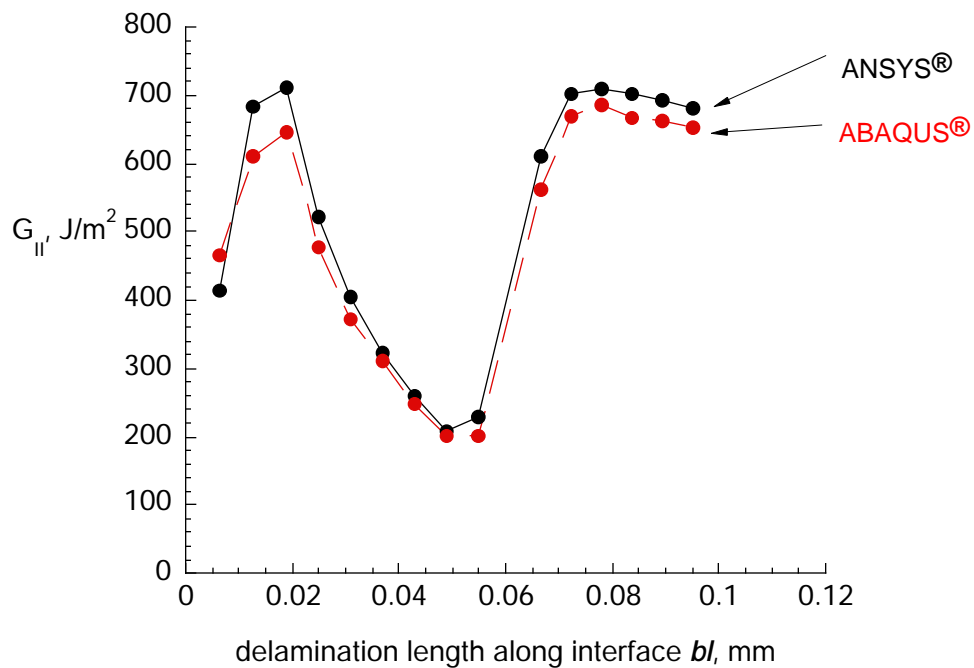
(b) Computed energy release rate G_{II} along delaminated interface
Figure 3. *Investigation of hybrid flex-beam specimen [17].*

(a) **D**ouble **C**antilever **B**eam Specimen (DCB)
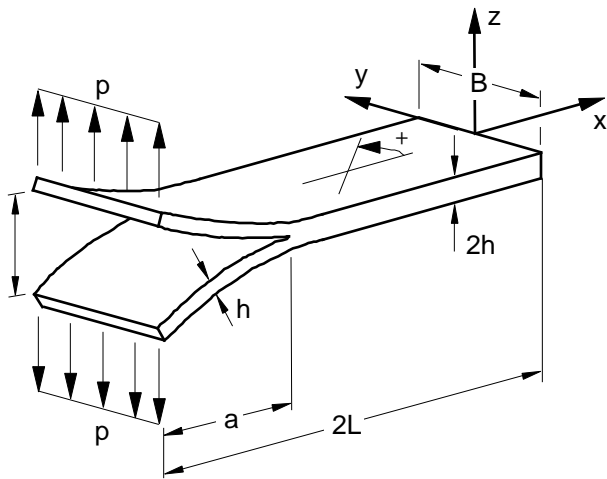
layup UD24

B	25.0 mm
2h	3.0 mm
2L	150.0 mm
a	111.5 mm
P	12.66 N

(b) **E**nd **N**otched **F**lexure Specimen (ENF)
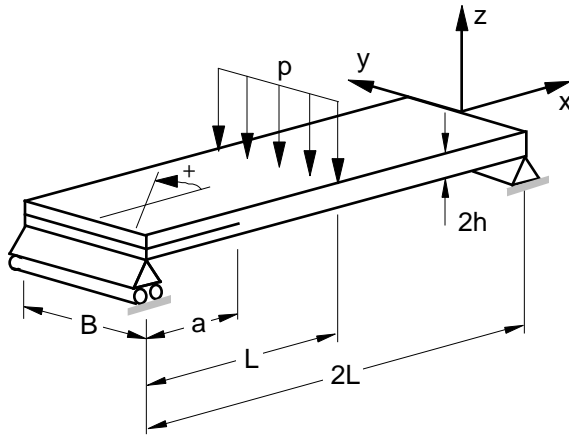
layup UD24

B	25.0 mm
2h	3.0 mm
2L	150.0 mm
a	30.0 mm
P	503.0 N

(c) **S**ingle **L**eg **B**ending Specimen (SLB)
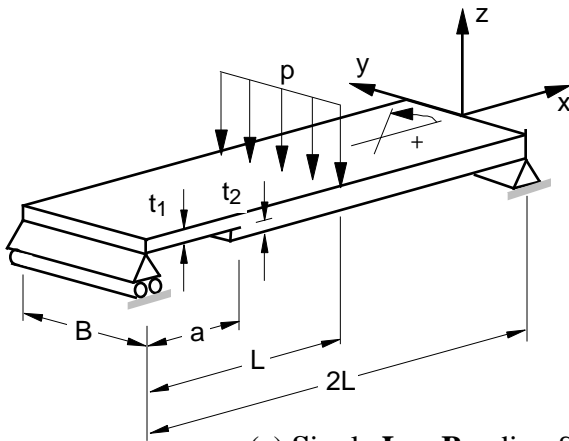
	layup UD32	layup D±30
B	25.0 mm	25.4 mm
t_1	2.03 mm	2.03 mm
t_2	2.03 mm	2.03 mm
2L	177.8 mm	177.8 mm
a	34.3 mm	34.3 mm
P	100.0 N	100.0 N

Figure 4. *Specimen configurations.*

local crack tip system
z',w',Z'

a

crack closed

undeformed state
(outline)

a

a

x',u',X'

Z'_i

W'_ℓ

i

k

U'_ℓ

X'_i

ℓ

W'_{ℓ^*}

z,w,Z

global system

ℓ^*

U'_{ℓ^*}

x,u,X

X,Y,Z: forces
u,v,w: displacements

deformed state

$G_I = - Z'_i (w'_I - w'_{I^*}) / (2 \ a)$

$G_{II} = - X'_i (u'_I - u'_{I^*}) / (2 \ a)$

(a): *VCCT for geometrically nonlinear analysis.*

local crack tip
system z',w',Z'

z,w,Z y,v,Y

global
system x,u,X

b

L

$w_{L\ell}$ $v_{L\ell}$

Z_{Li}

$u_{L\ell}$

Y_{Li}

x',u',X'

$w_{L\ell^*}$

X_{Li}

ℓ

$u_{L\ell^*}$

i

ℓ^*

X,Y,Z: forces
u,v,w: displacements

a   a   a

$G_I = - Z'_i (w'_I - w'_{I^*}) / (2 \ ab)$

$G_{II} = - X'_i (u'_I - u'_{I^*}) / (2 \ ab)$

$G_{III} = - Y'_i (v'_I - v'_{I^*}) / (2 \ ab)$
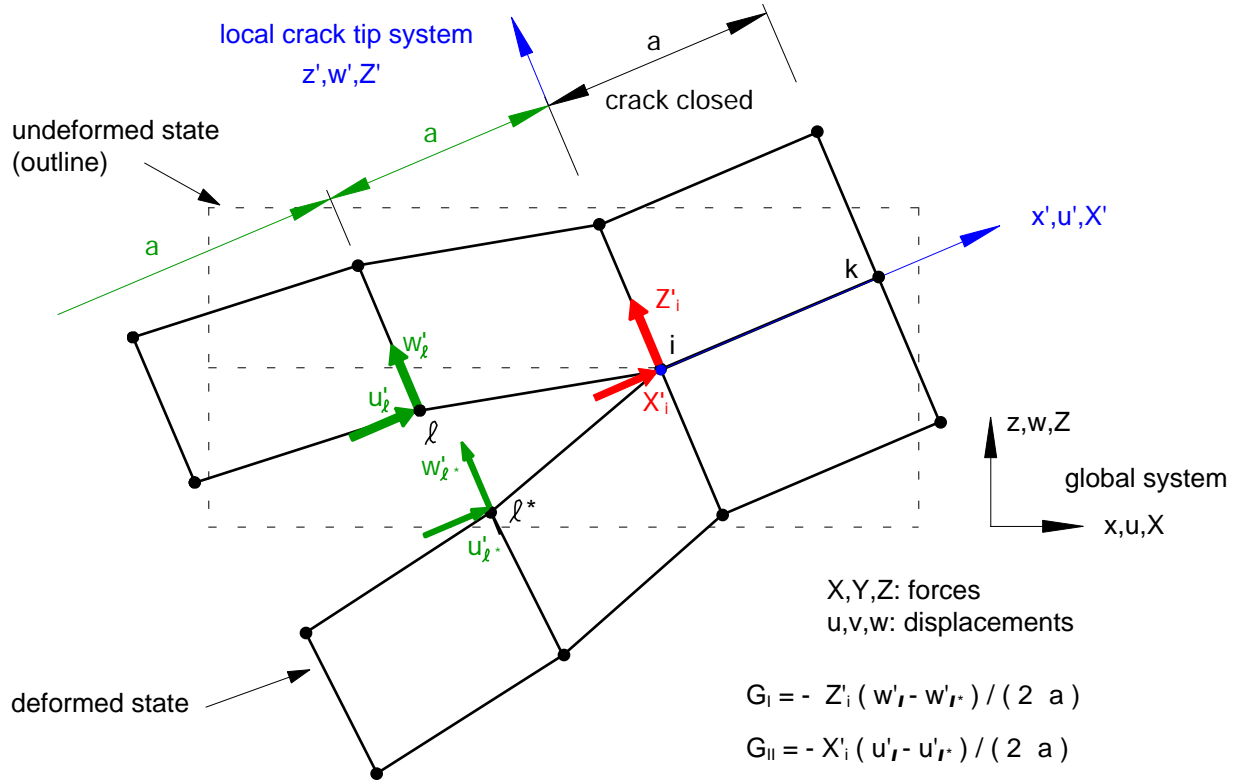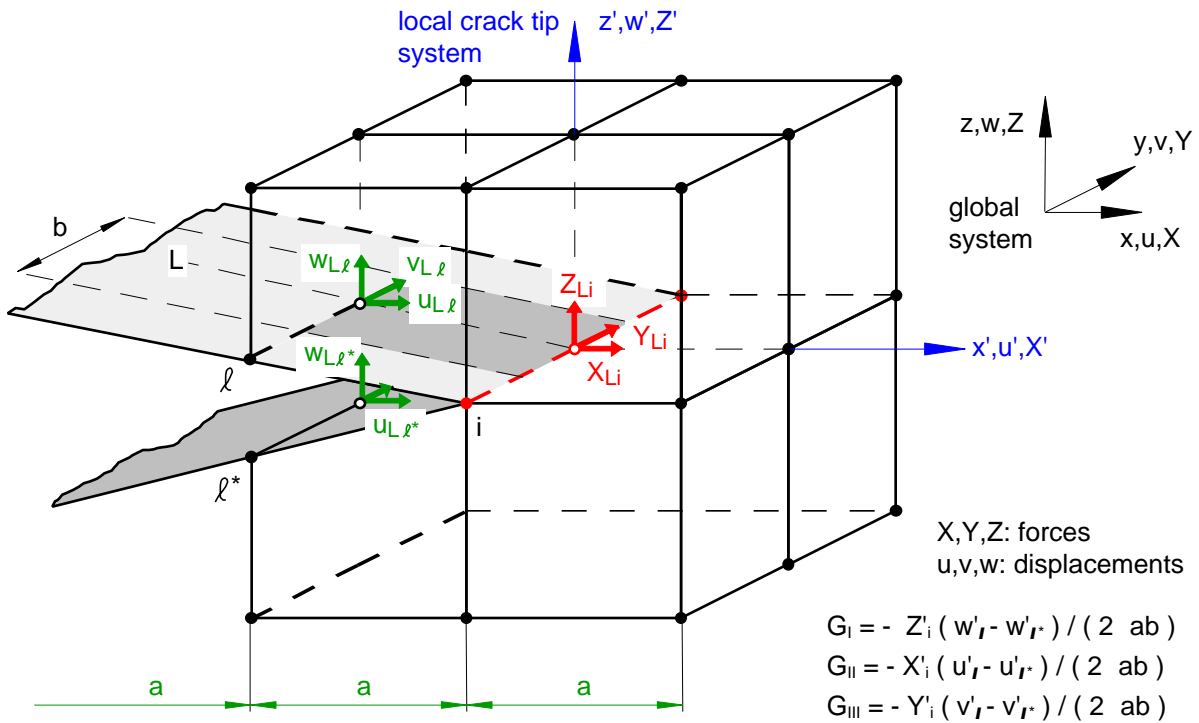
(b). *VCCT for eight noded solid elements.*

Figure 5: *Virtual Crack Closure Technique (VCCT).*
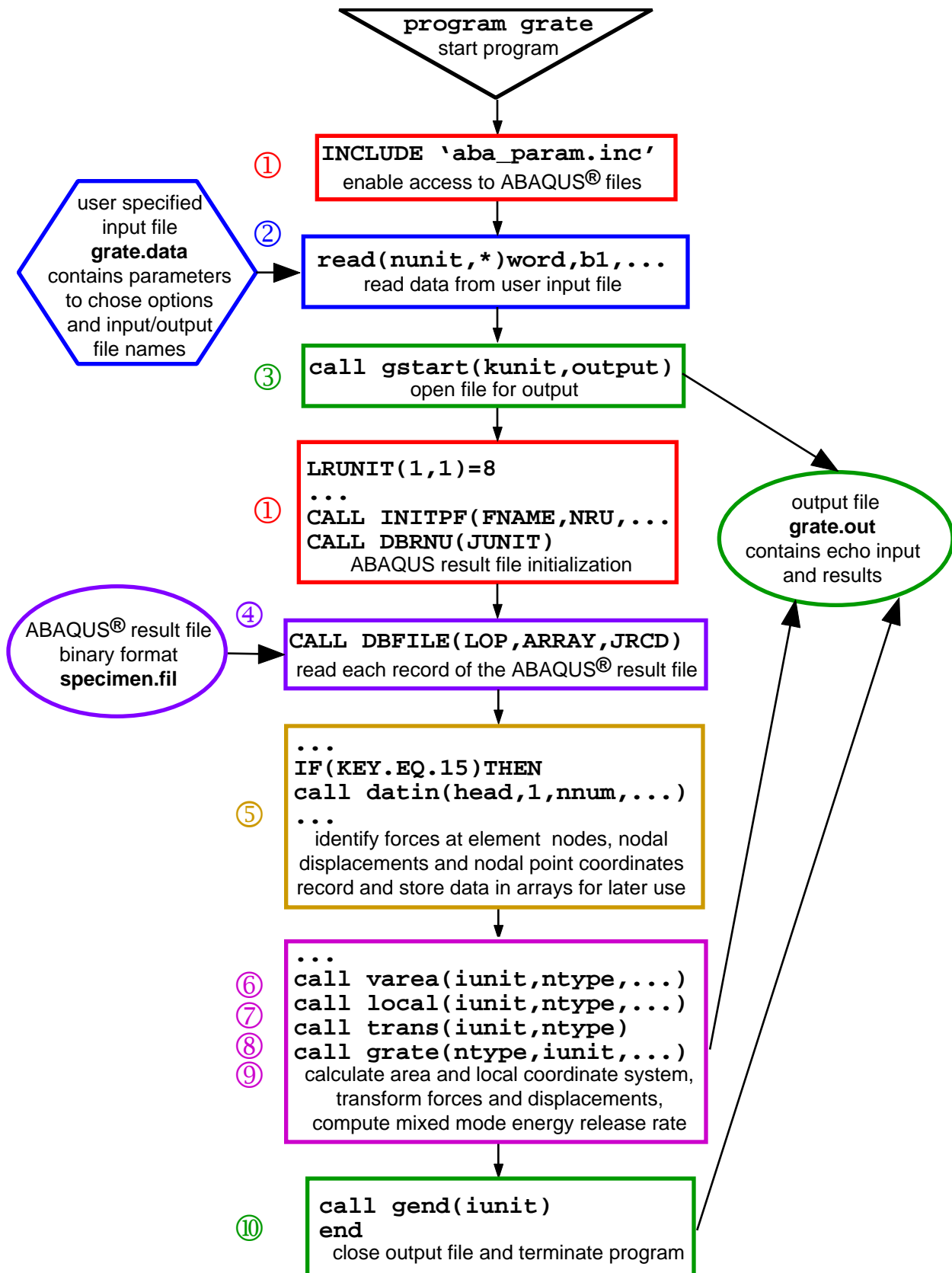
Figure 6. *Flow chart of routine to calculate strain energy release rates from ABAQUS® results*
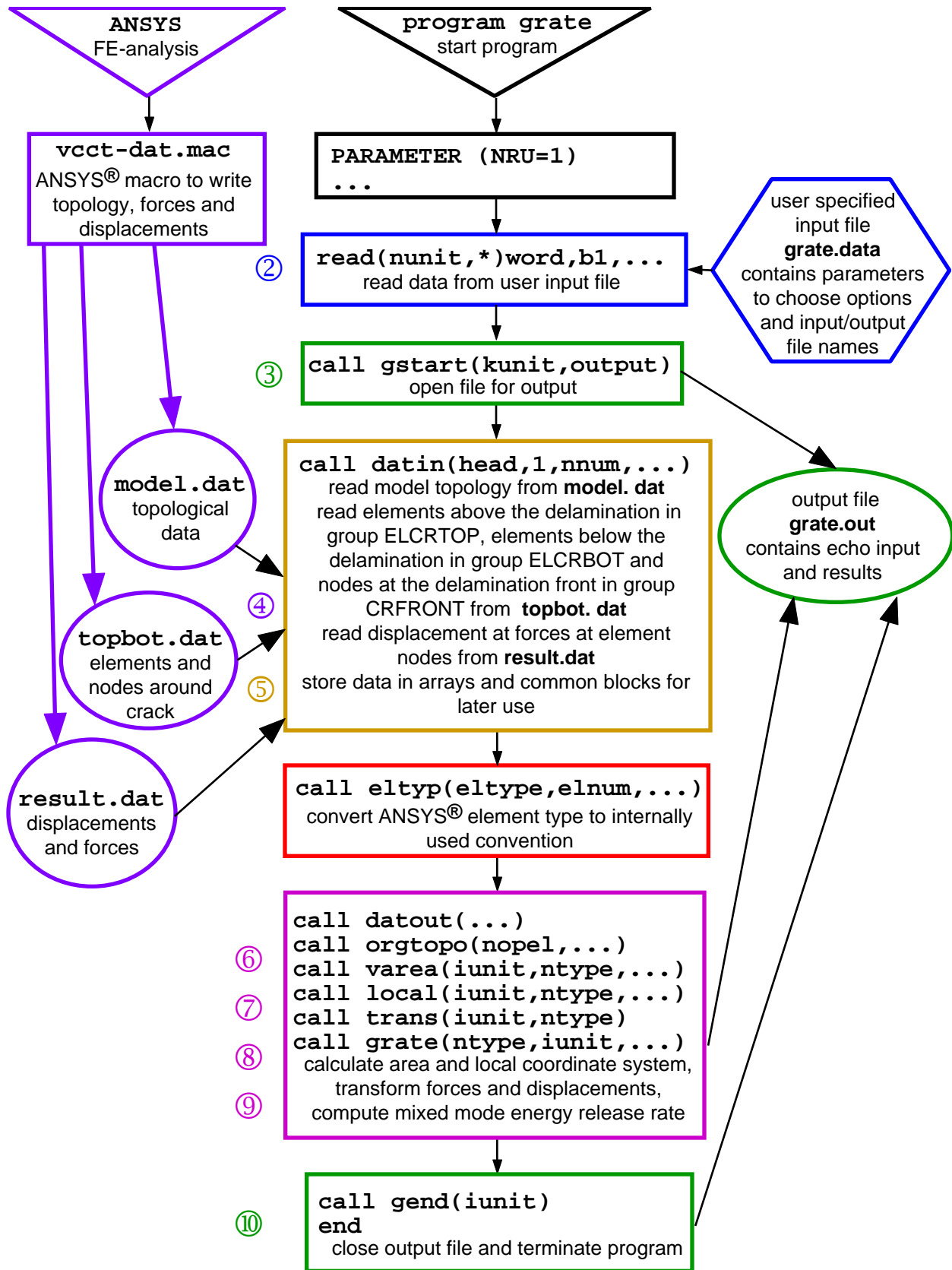
Figure 7. *Flow chart of modified routine to calculate strain energy release rates.*
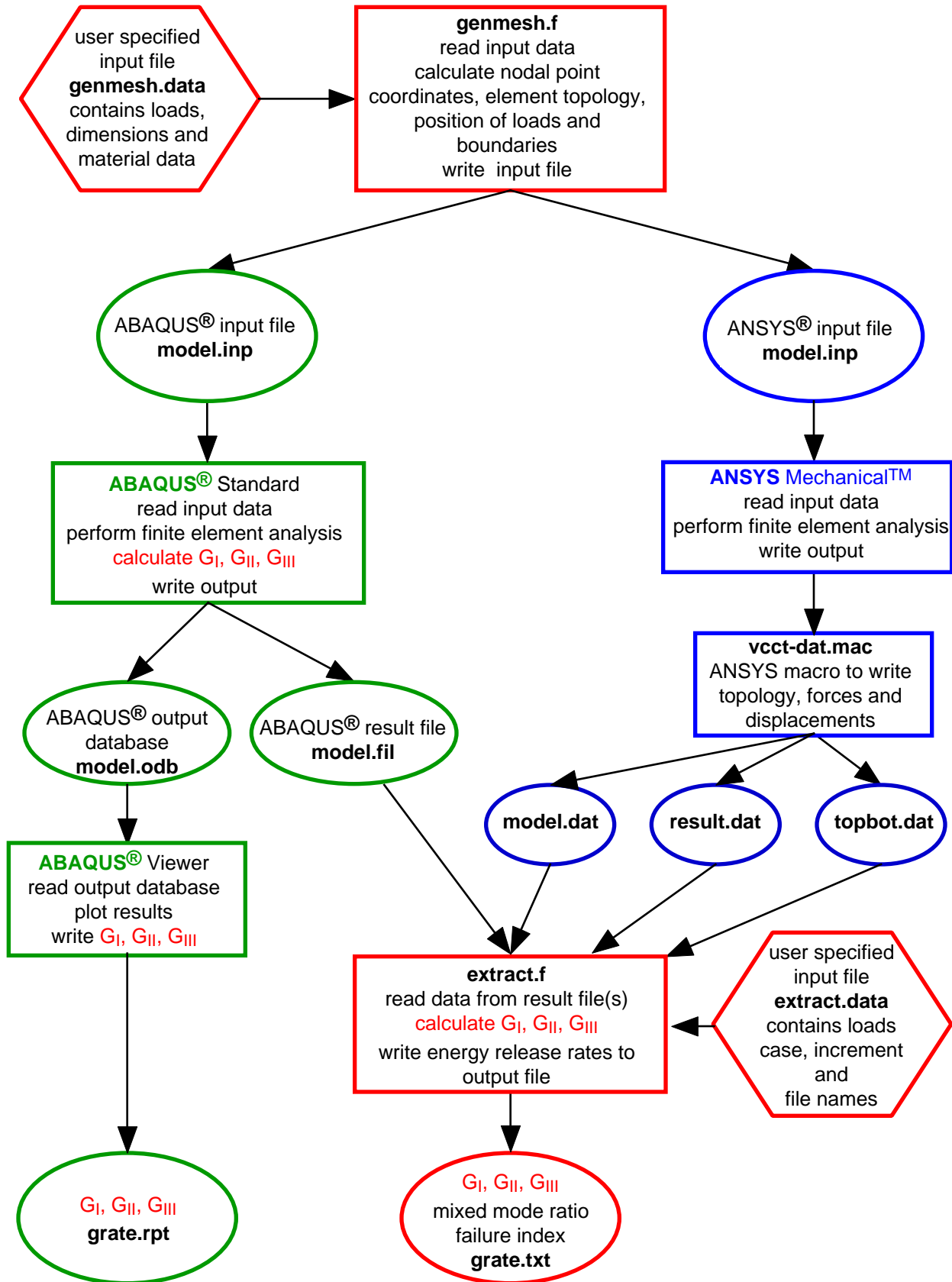
Figure 8. *Flow chart of entire analysis procedure.*

length
B/2   12.5 mm
2L   150.0 mm

2L

B/2

i

g

f

e

d

c

b

	length	element
b	70.0 mm	14
c	36.5 mm	9
d	10.0 mm	20
e	3.5 mm	2
f	10.0 mm	2
g	20.0 mm	4
i	11.5 mm	12

(a) Dimensions

detail of local
model around
delamination front

d

j

2h

delamination front

	length	element
2h	3.0 mm	6
j	1.0 mm	8
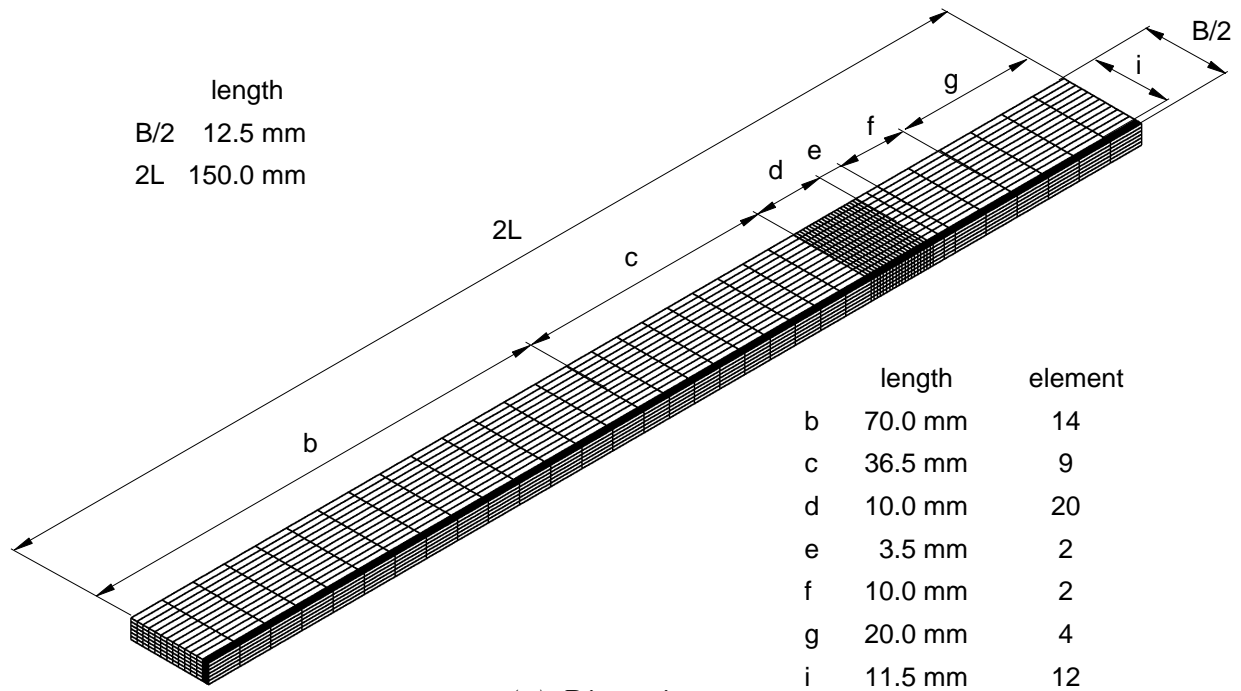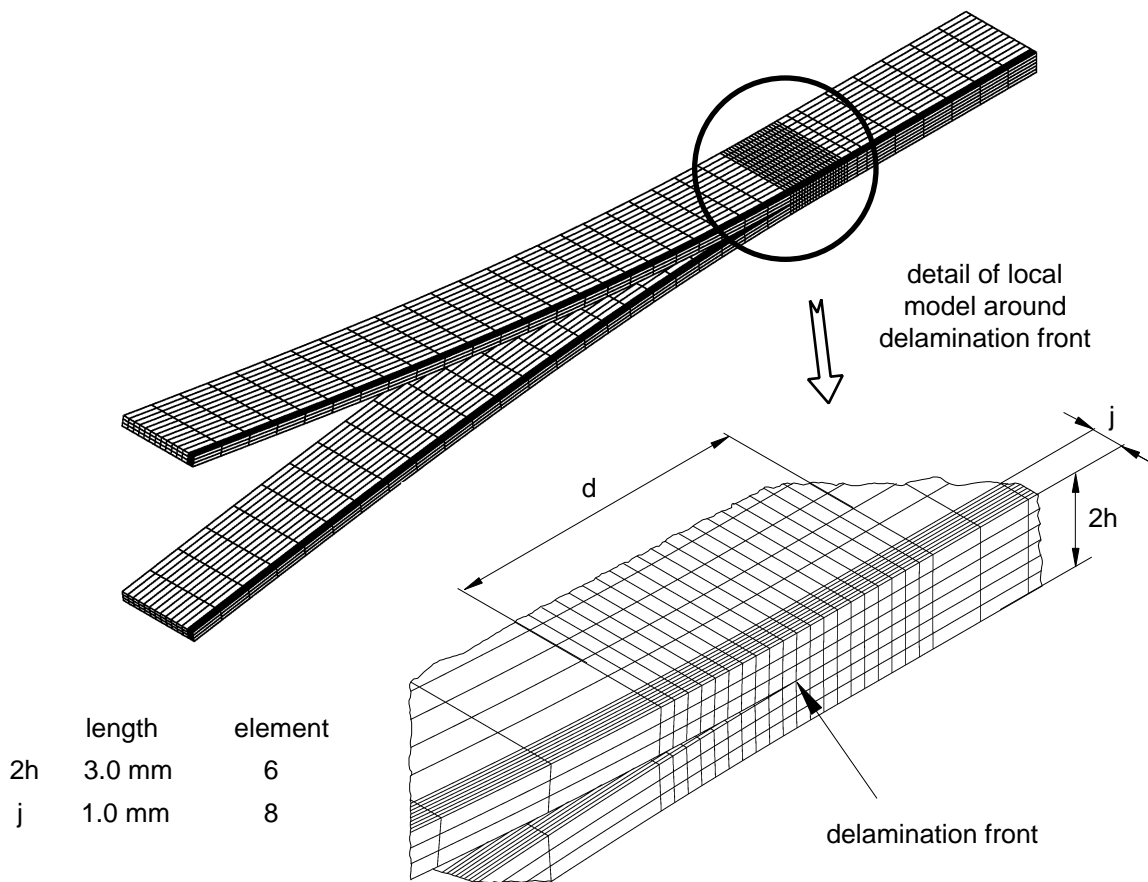
(b) Deformed model of DCB specimen and detail of refined region around delamination front

Figure 9. *Full three-dimensional finite element model of a DCB specimen*

	length	element
B	25.0 mm	
i	23.0 mm	21
2h	3.0 mm	6
j	1.0 mm	8

	length	element
b	70.0 mm	14
c	36.5 mm	9
d	10.0 mm	8
e	3.5 mm	2
f	10.0 mm	3
g	20.0 mm	3
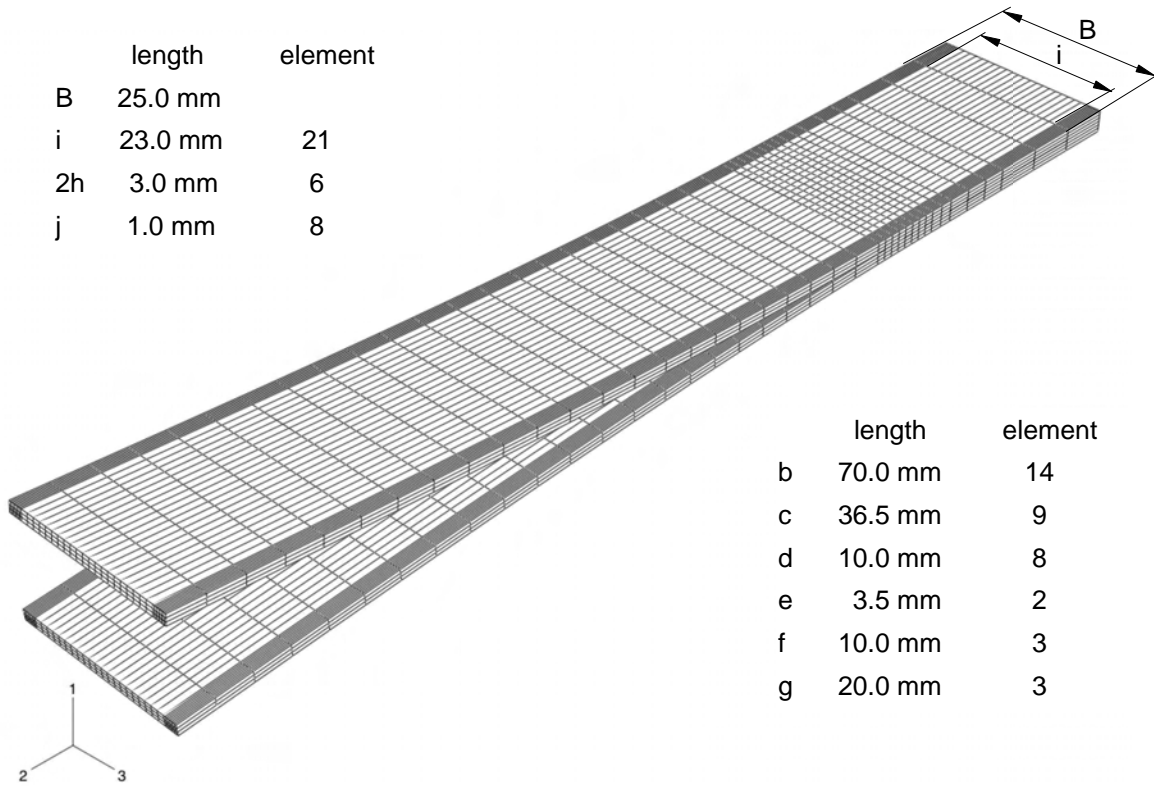
(a) Deformed model of DCB specimen with refined edge

	length	element
B=i	25.0 mm	25
2h	3.0 mm	6

	length	element
b	70.0 mm	14
c	36.5 mm	9
d	10.0 mm	8
e	3.5 mm	2
f	10.0 mm	3
g	20.0 mm	3
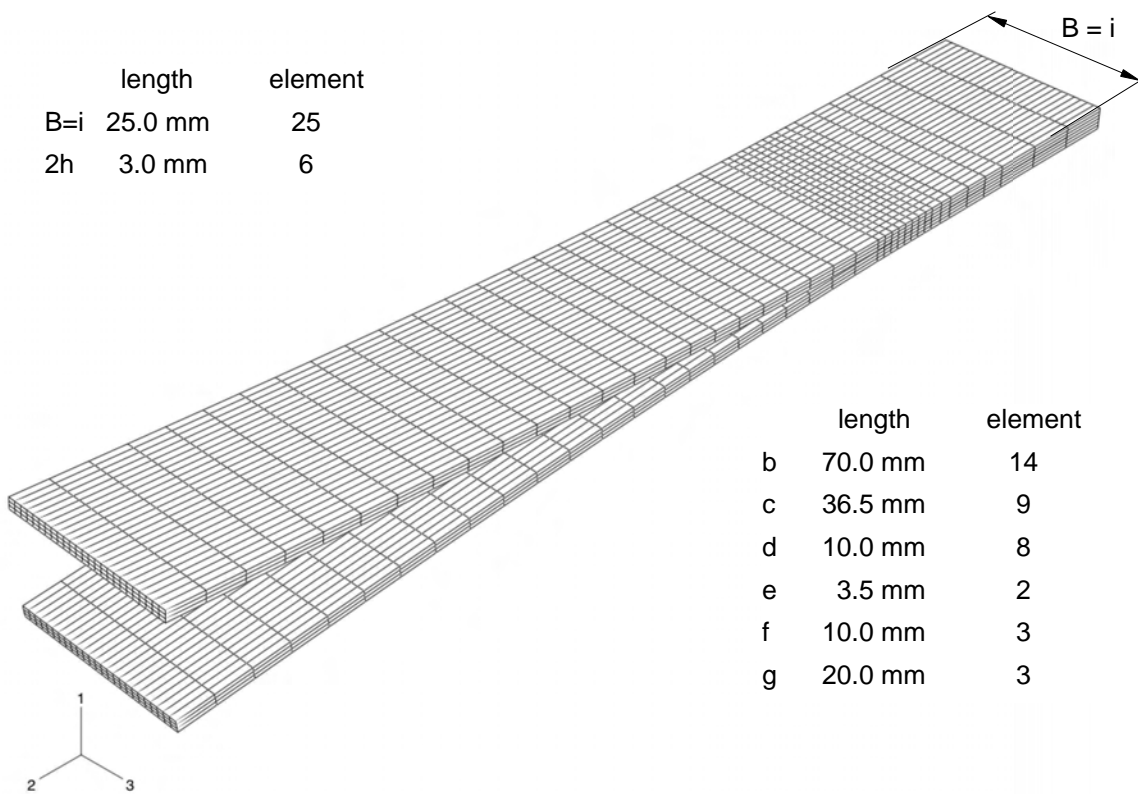
(b) Deformed model of DCB specimen with uniform mesh
Figure 10. *Full three-dimensional finite element model of a DCB specimen*

	length	element
B=i	25.0 mm	25
2h	3.0 mm	6

	length	element
b	70.0 mm	14
c	36.5 mm	9
d	10.0 mm	20
e	3.5 mm	2
f	10.0 mm	3
g	20.0 mm	3
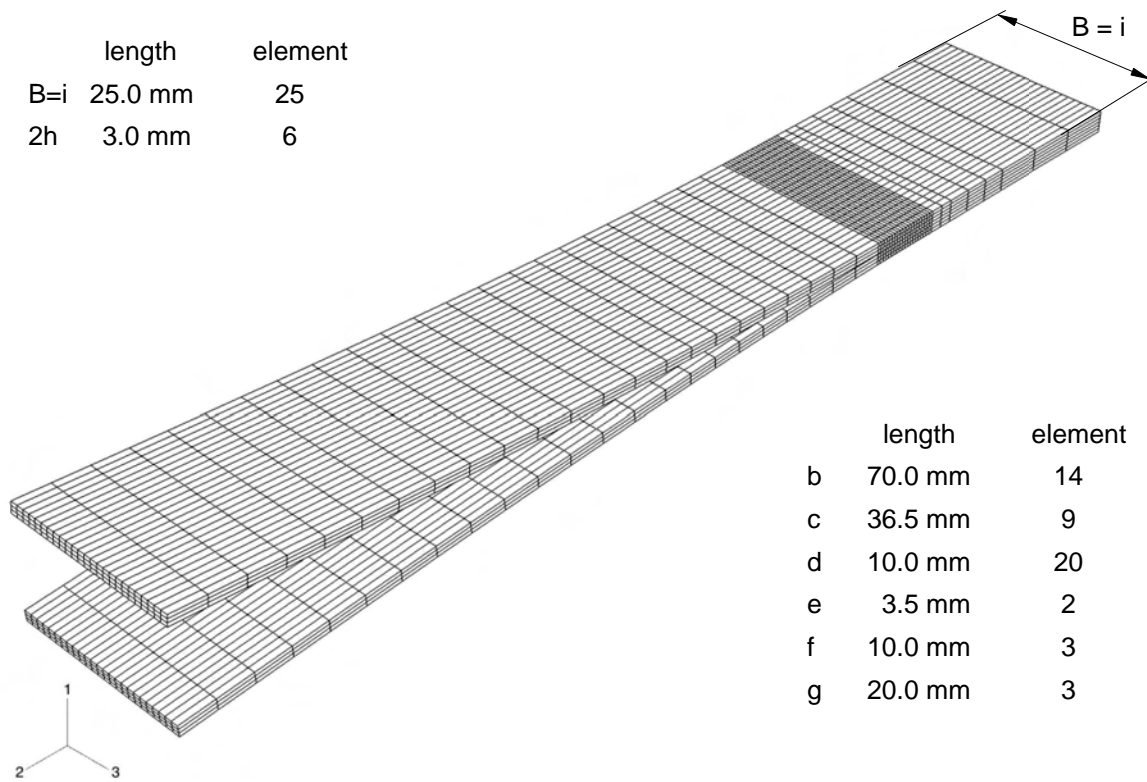
Figure 11. *Full three-dimensional finite element model of a DCB specimen*

	length	element
B	25.0 mm	
i	22.5 mm	10
2h	3.0 mm	6
j	1.25 mm	8

	length	element
b	21.0 mm	2
c	25.0 mm	6
d	10.0 mm	20
e	13.0 mm	3
f	48.0 mm	9
g	33.0 mm	3
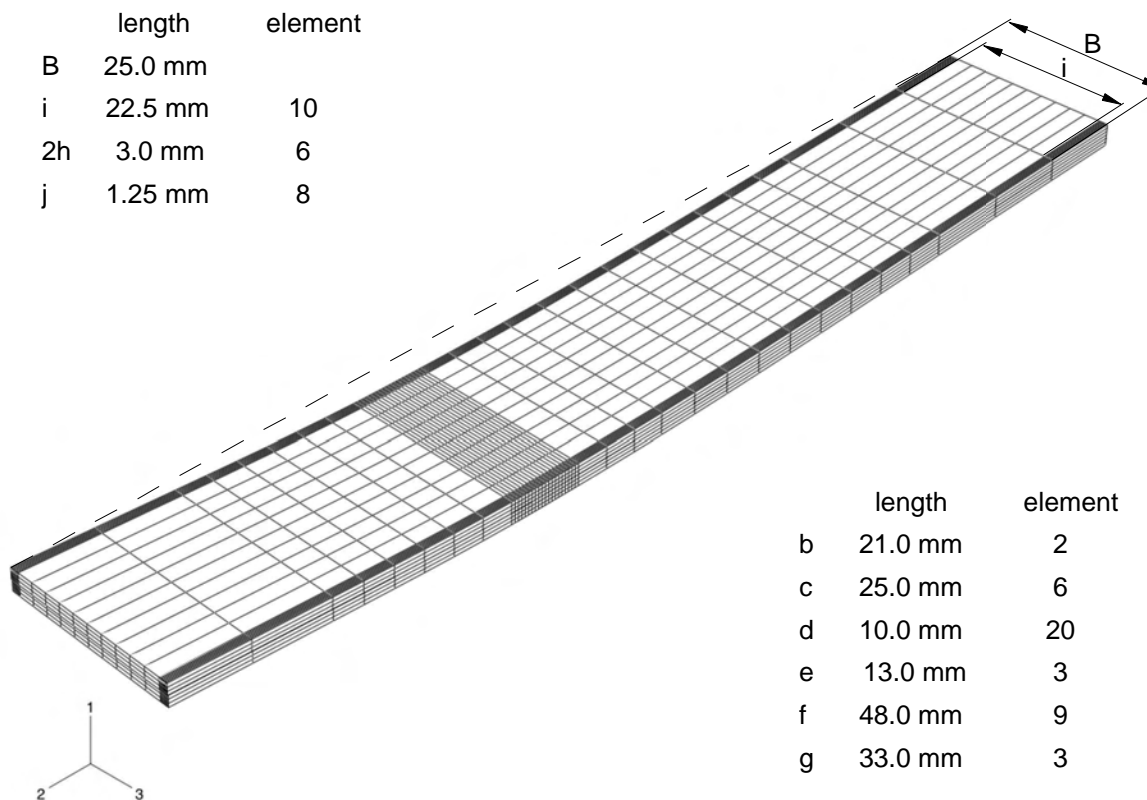
Figure 12. *Full three-dimensional finite element model of an ENF specimen*

$- - - - -$ outline of undeformed configuration

w_c: deflection in the center of the specimen

	length	element
B	25.4 mm	
i	21.4 mm	10

w_c

B

i

	length	element
b	1.0 mm	1
c	32.79 mm	5
d	3.0 mm	12
e	53.11 mm	5
f	88.9 mm	10
g	1.2 mm	1

detail of local
model around
delamination front
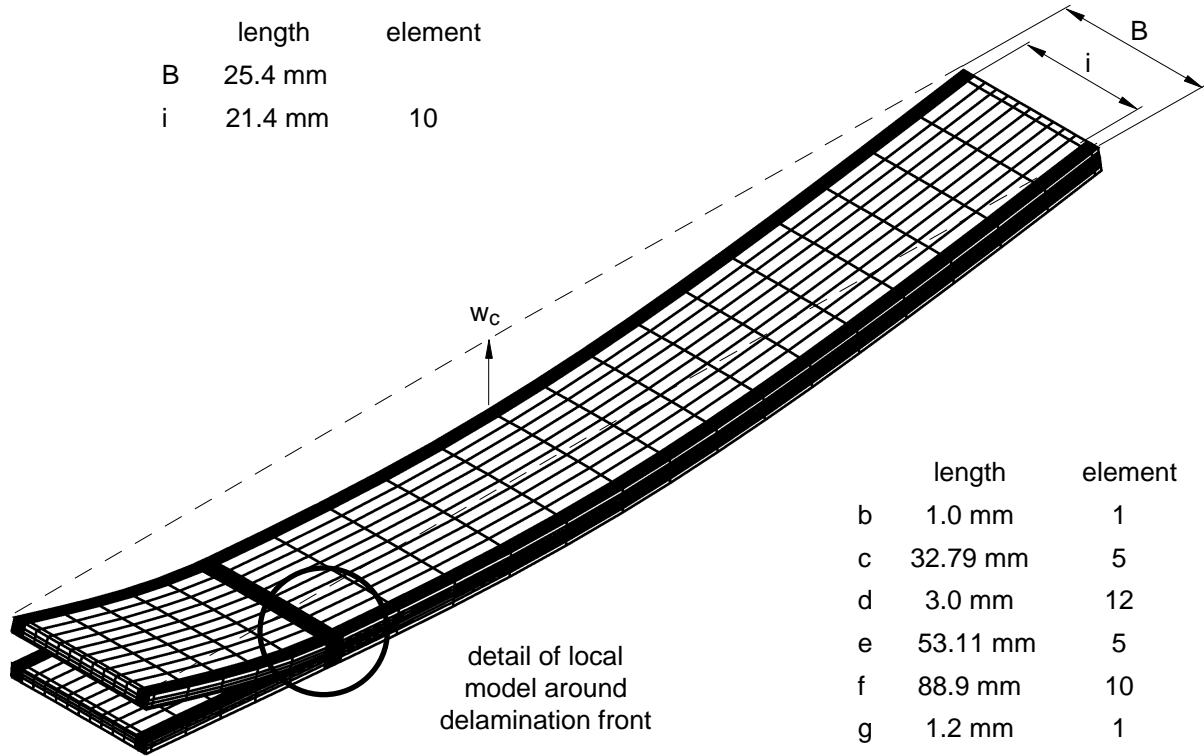
	length	element
d	3.0 mm	12
j	2.0 mm	8
$t_1 = t_2$	2.032 mm	5

d

i

t_1

t_2

±30/0/-30/0/30

0_4

30/0/-30/0

-30

30

delamination front
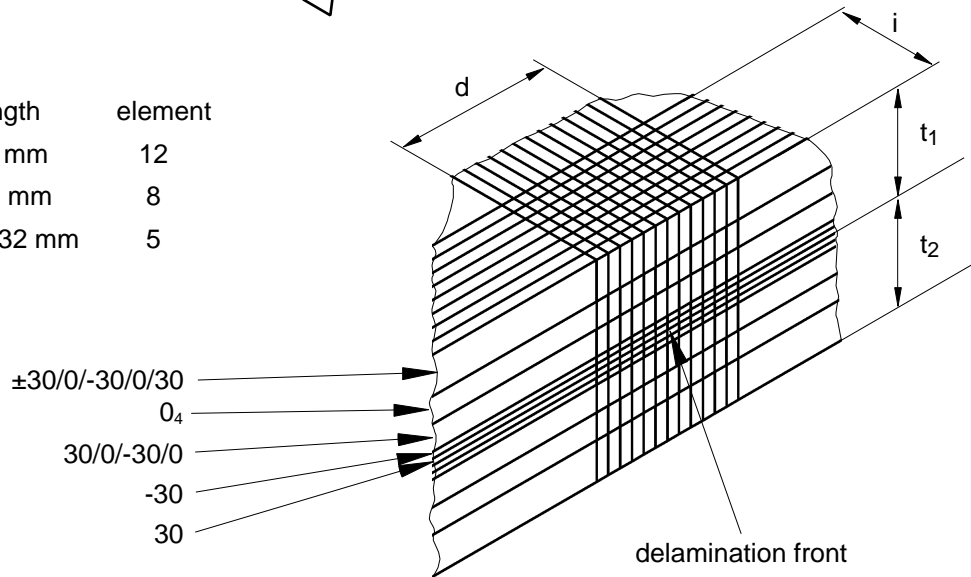
Figure 13. *Finite element model of SLB specimen with D±30 layup*

	length	element
B	25.4 mm	
i	21.4 mm	21
j	2.0 mm	8
$t_1 = t_2$	2.032 mm	5

	length	element
b	1.0 mm	1
c	32.79 mm	5
d	3.0 mm	12
e	53.11 mm	5
f	88.9 mm	10
g	1.2 mm	1
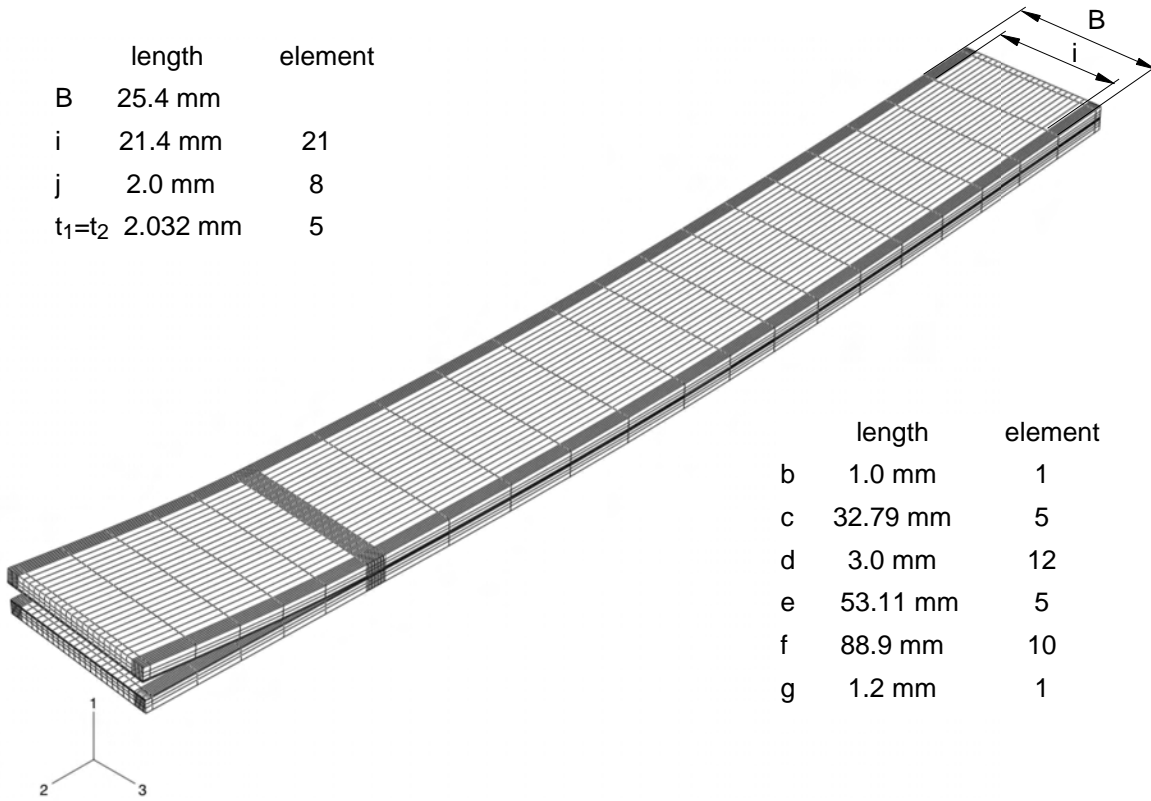
(a) Deformed model of SLB specimen with refined mesh at the edge

	length	element
B	25.4 mm	
i	23.4 mm	23
j	1.0 mm	1
$t_1 = t_2$	2.032 mm	5

	length	element
b	1.0 mm	1
c	32.79 mm	5
d	3.0 mm	12
e	53.11 mm	5
f	88.9 mm	10
g	1.2 mm	1
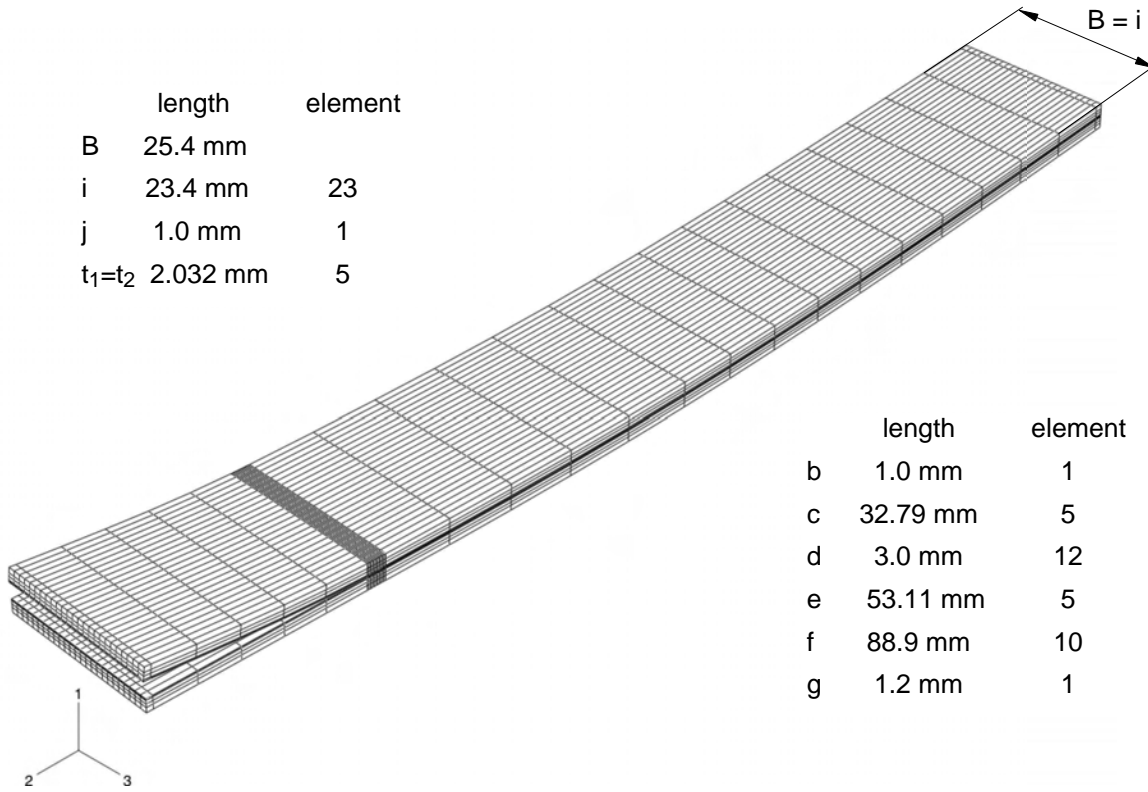
(b) Deformed model of SLB specimen with uniform mesh
Figure 14. *Full three-dimensional finite element model of a SLB specimen*
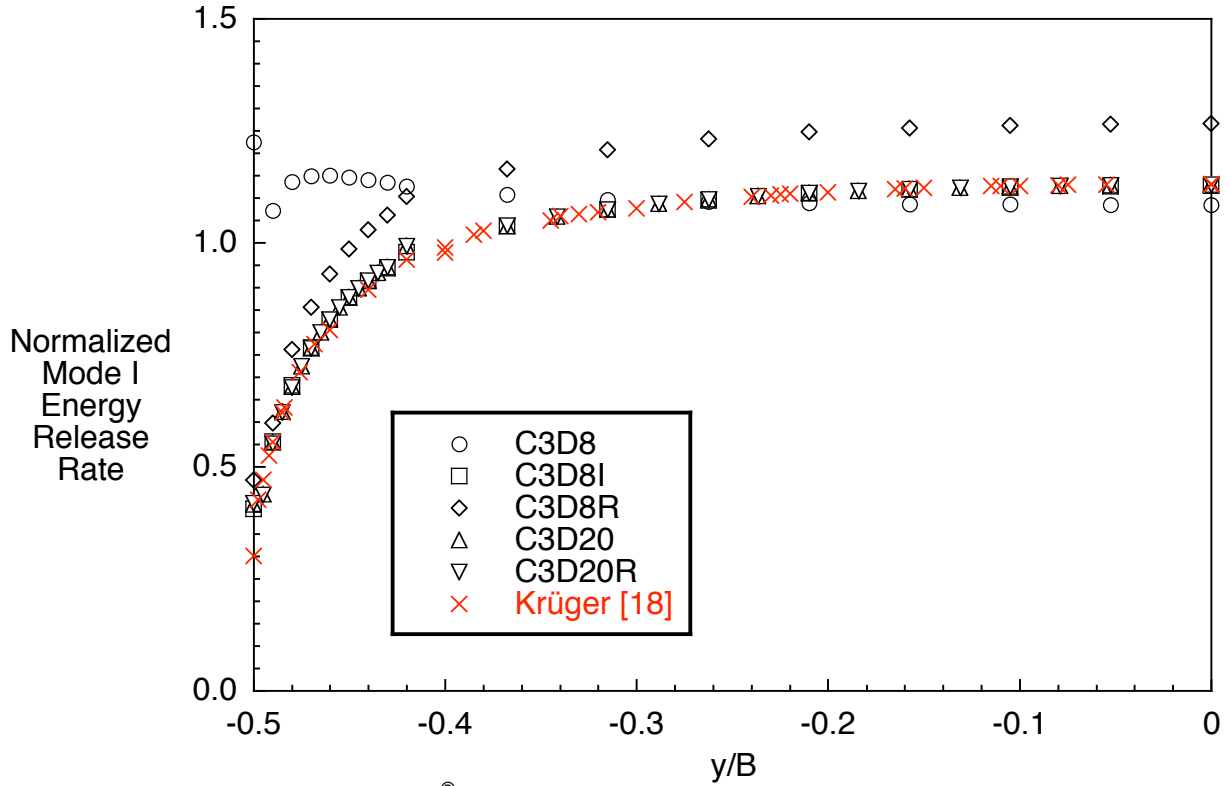
Figure 15. *Influence of ABAQUS® element selection on computed strain energy release rate distribution across the width of a DCB specimen with UD24 layup.*
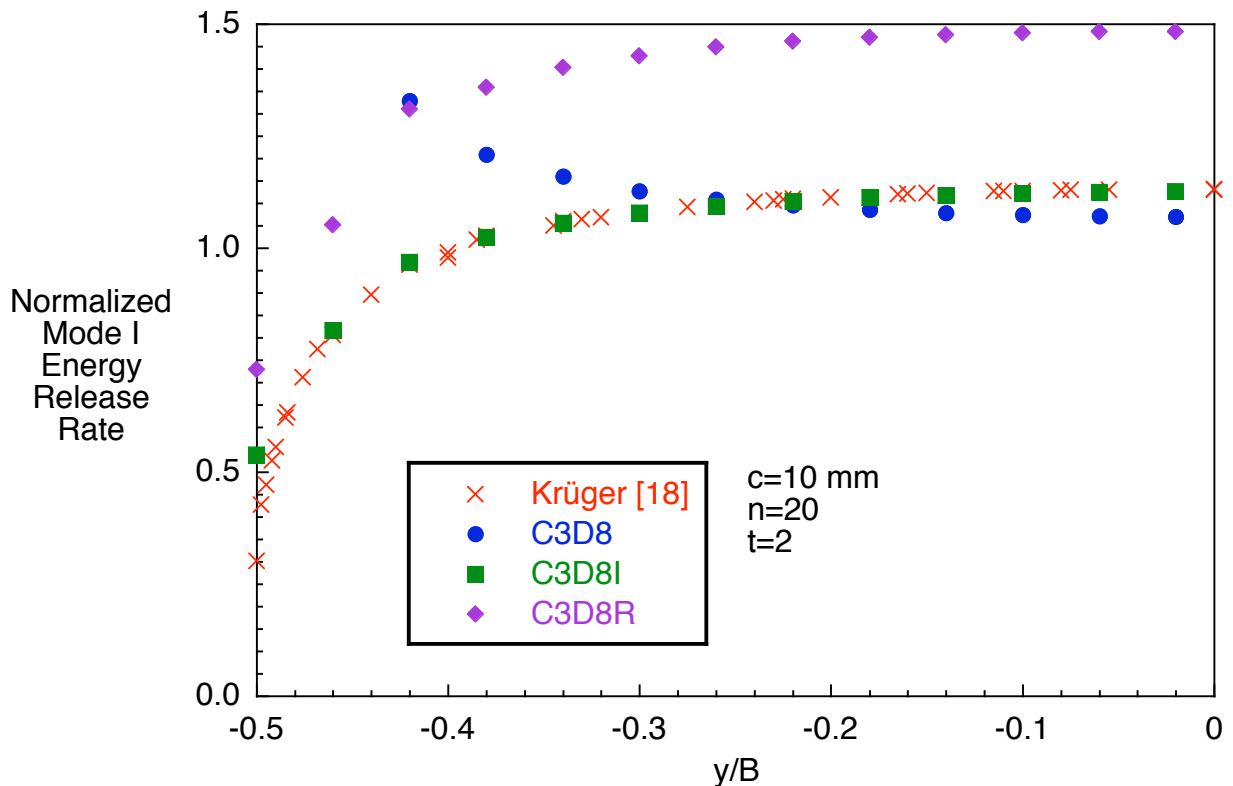
Figure 16. *Influence of element selection on computed strain energy release rate distribution across the width of a DCB specimen with UD24 layup.*
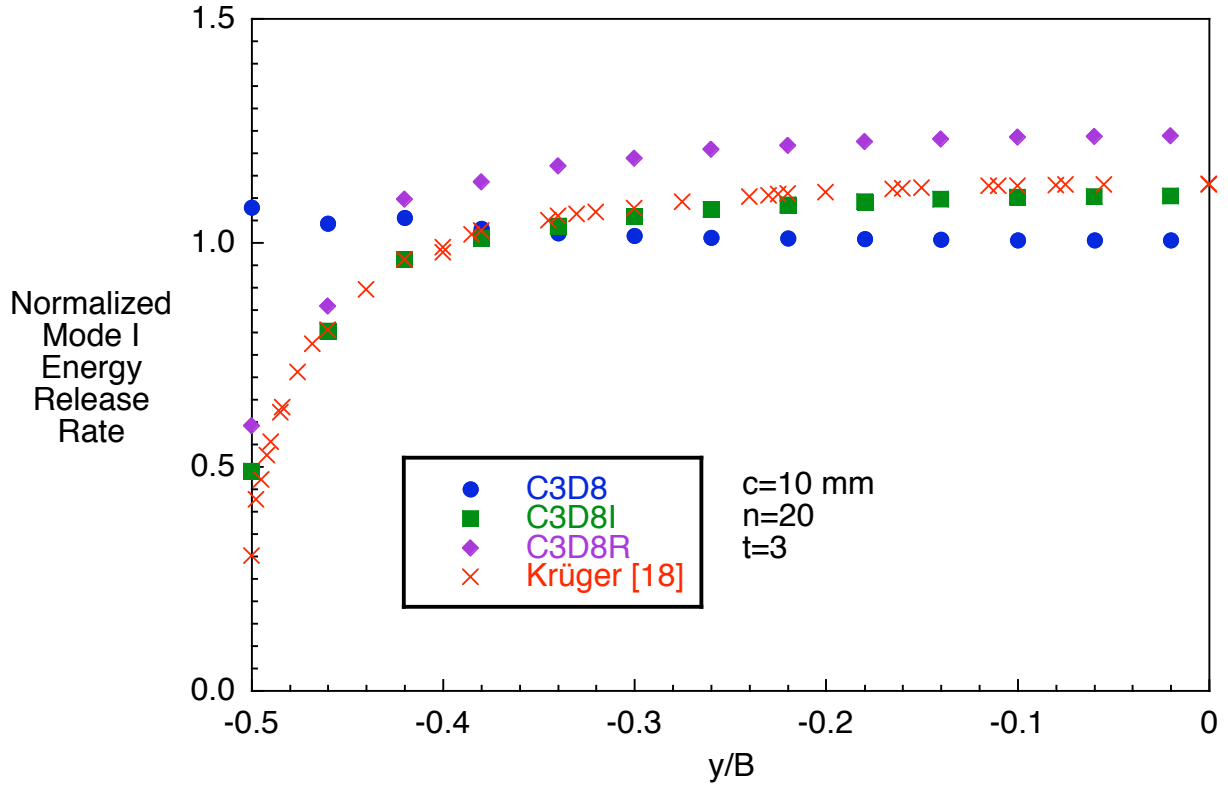
Figure 17. *Influence of element selection on computed strain energy release rate distribution across the width of a DCB specimen with UD24 layup.*
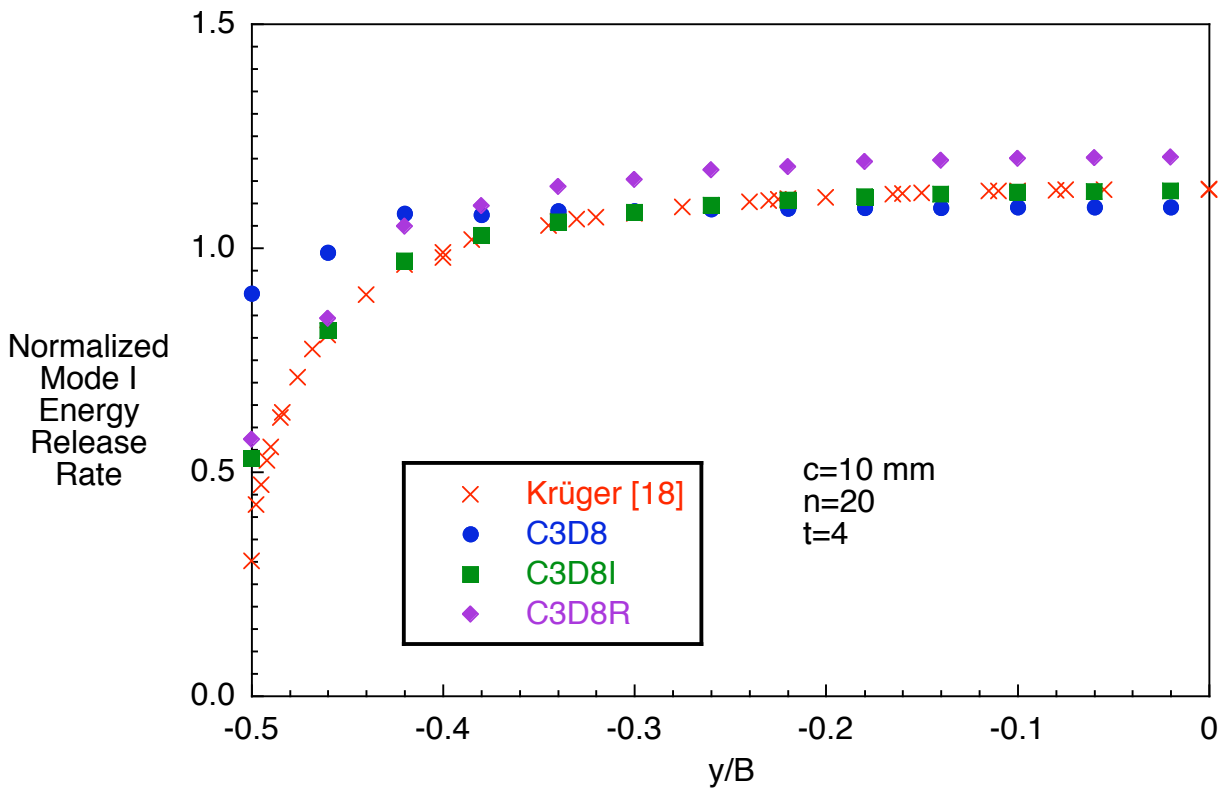
Figure 18. *Influence of element selection on computed strain energy release rate distribution across the width of a DCB specimen with UD24 layup.*
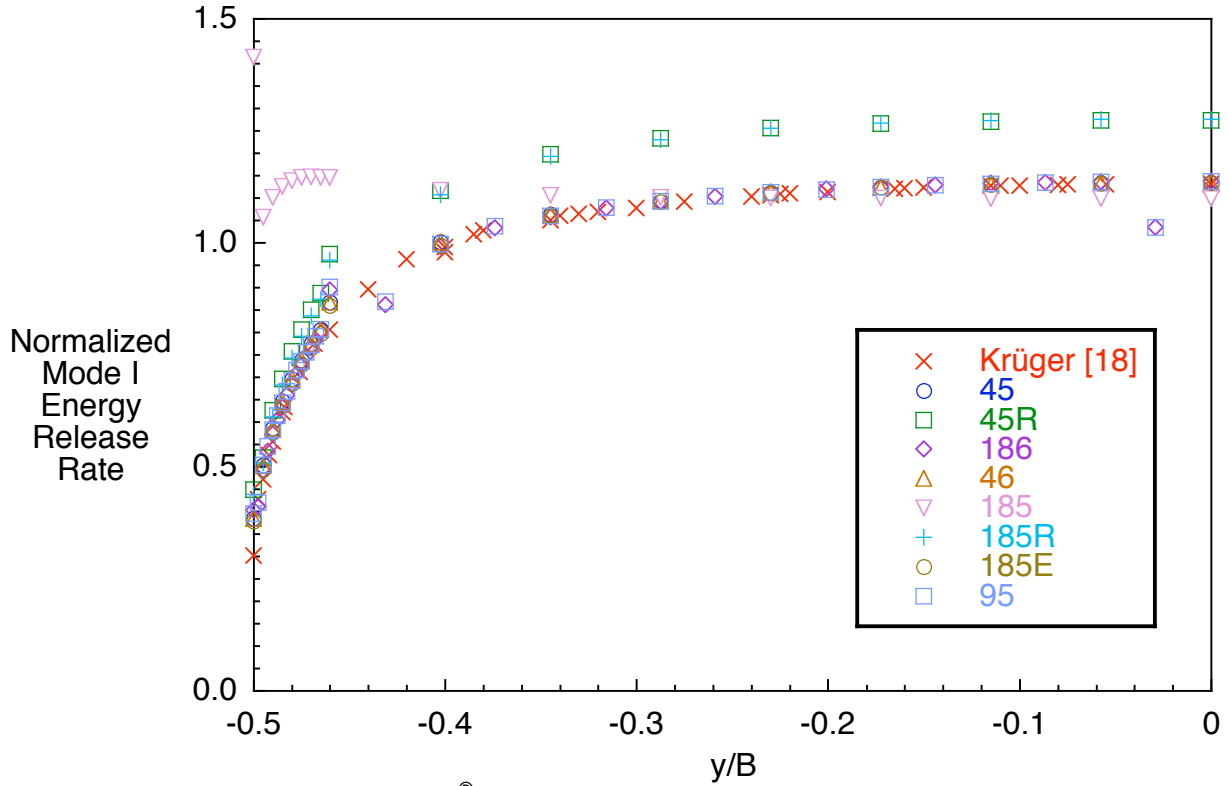
Figure 19. *Influence of ANSYS[®] element selection on computed strain energy release rate distribution across the width of a DCB specimen with UD24 layup.*
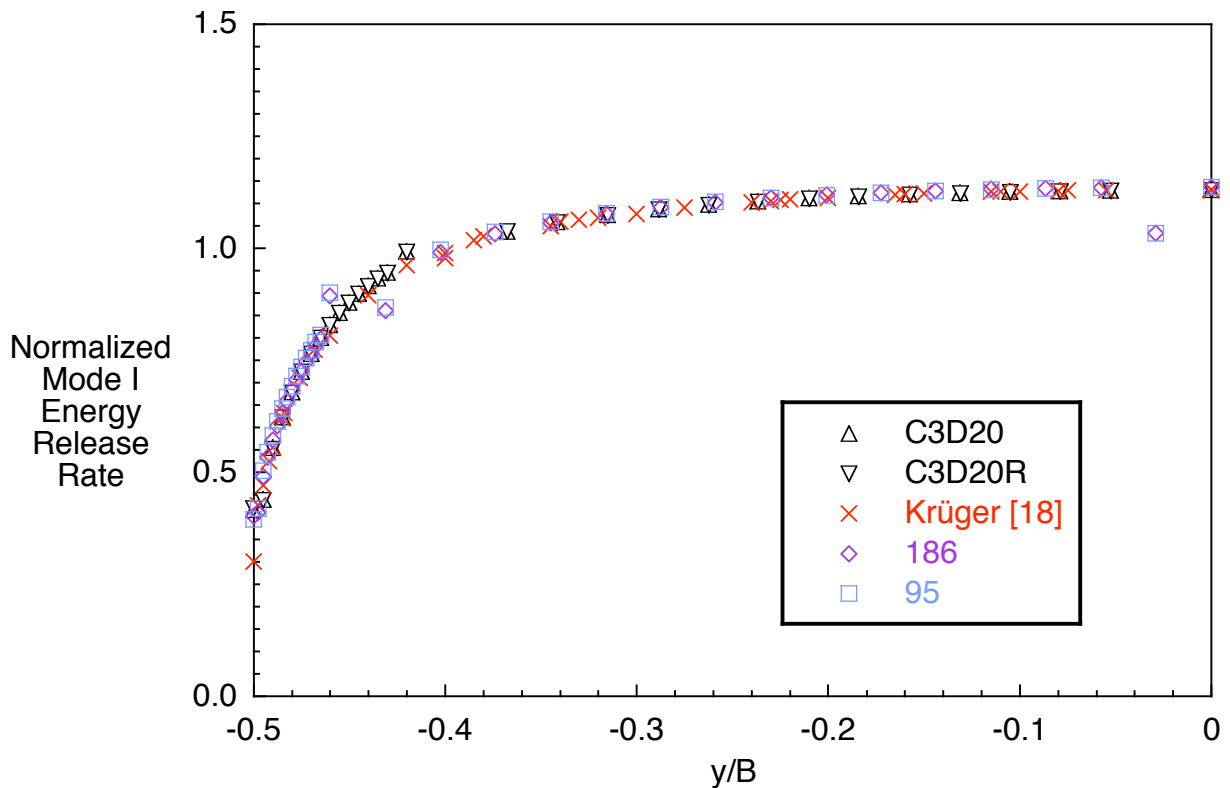
Figure 20. *Computed strain energy release rate distribution across the width of a DCB specimen with UD24 layup modeled with twenty-noded solid elements.*

33
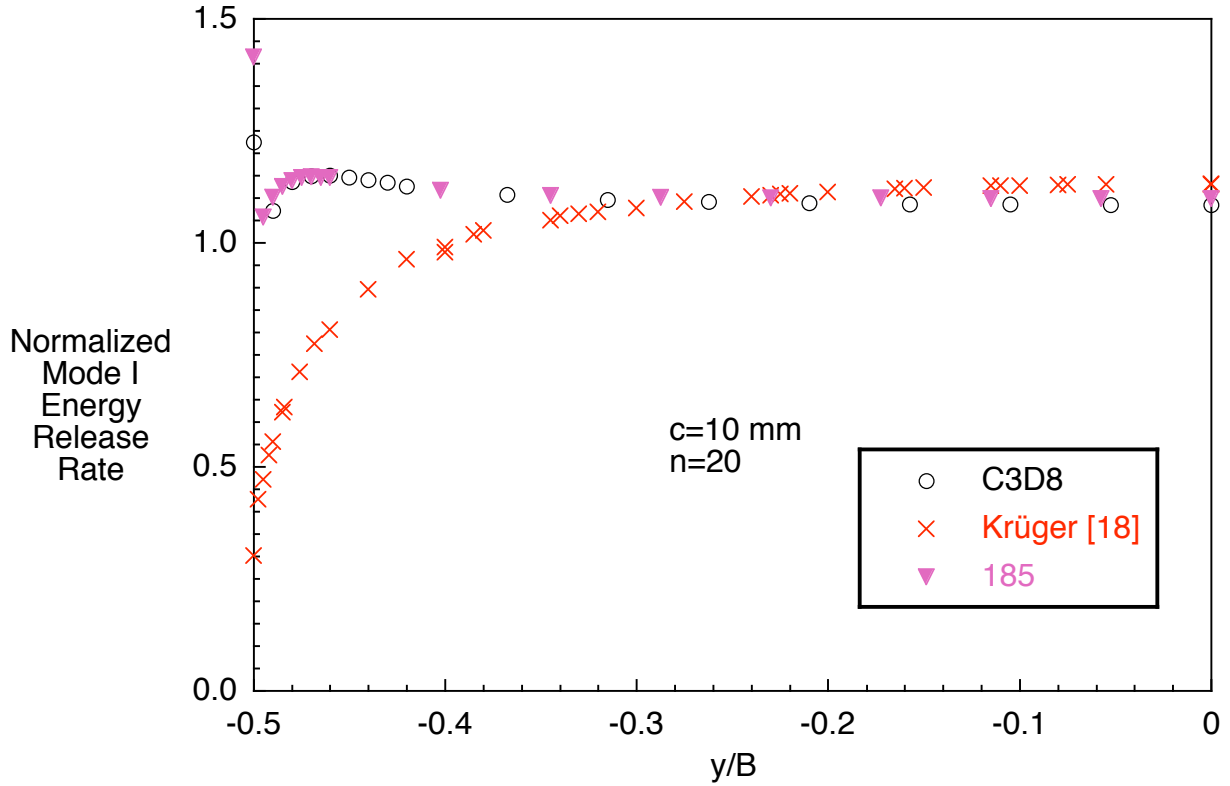
Figure 21. *Computed strain energy release rate distribution across the width of a DCB specimen with UD24 layup modeled with eight-noded brick elements.*
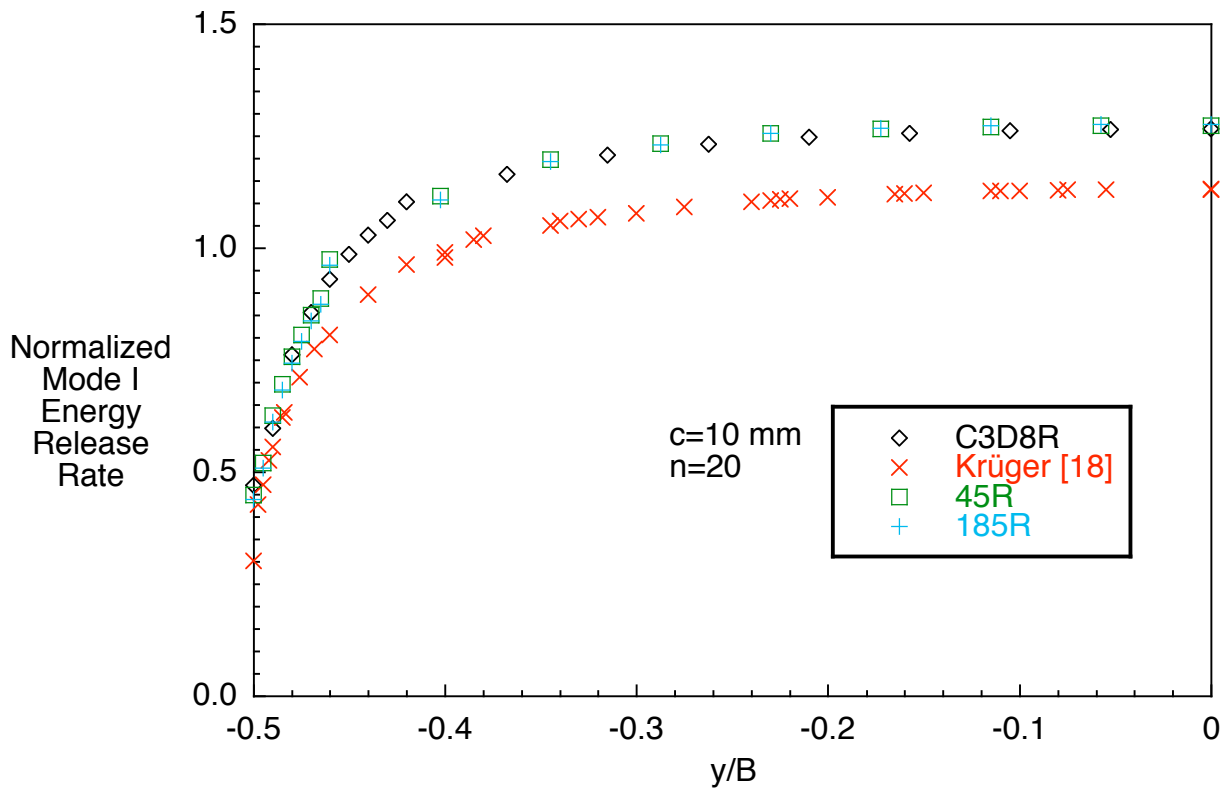
Figure 22. *Computed strain energy release rate distribution across the width of a DCB specimen with UD24 layup modeled with reduced integration eight-noded brick elements.*
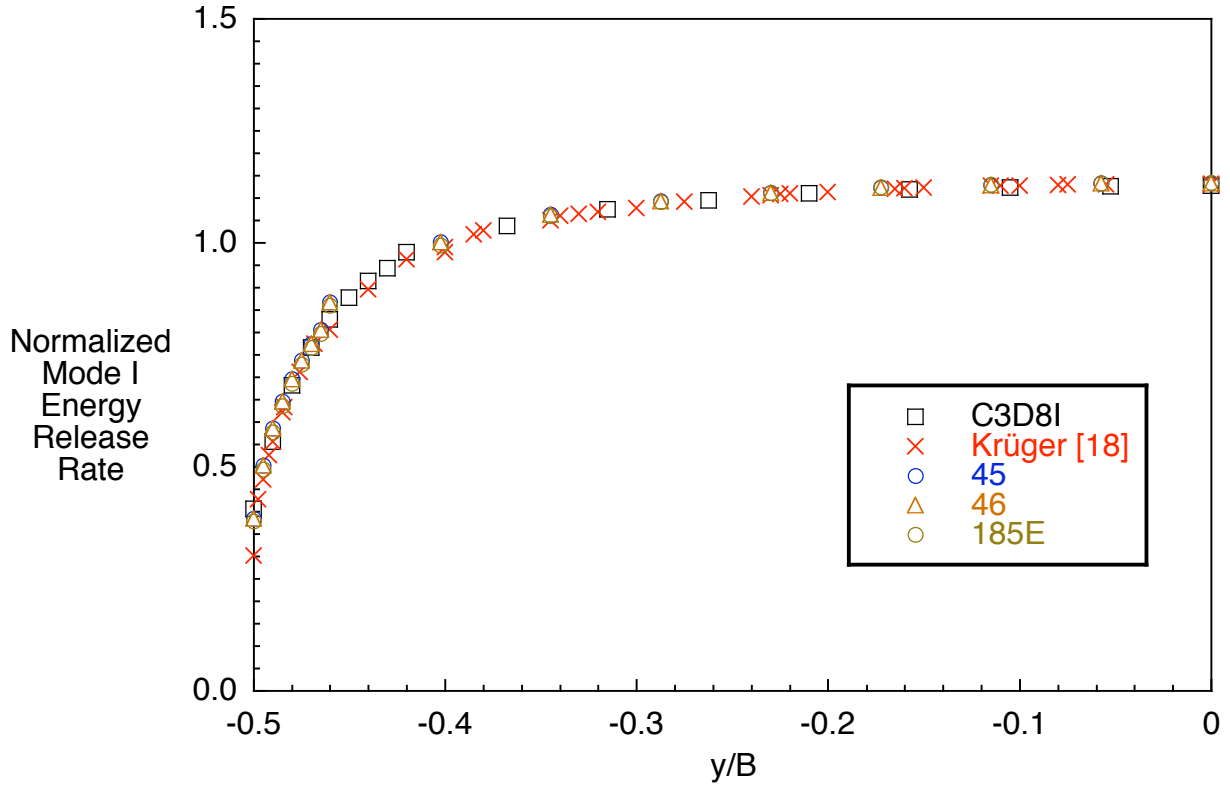
Figure 23. *Computed strain energy release rate distribution across the width of a DCB specimen with UD24 layup modeled with incompatible mode eight-noded brick elements.*
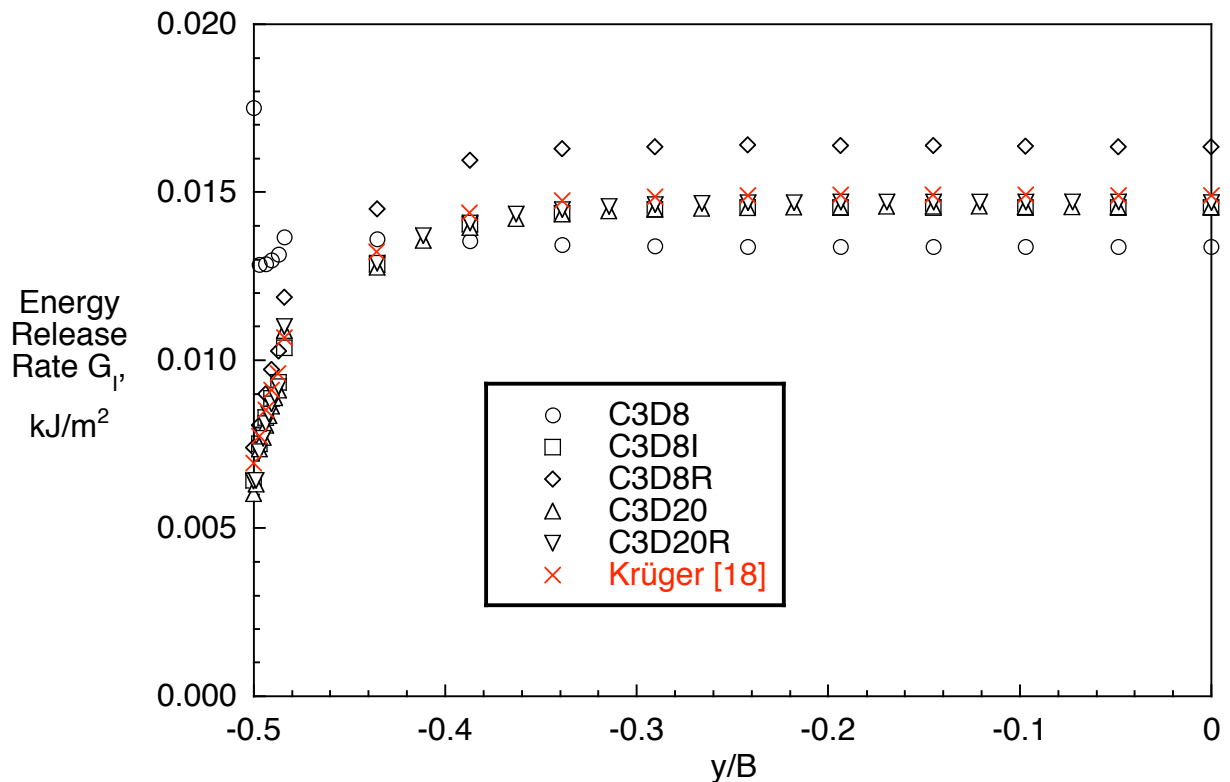
Figure 24. *Influence of ABAQUS® element selection on computed mode I strain energy release rate distribution across the width of a SLB specimen with UD32 layup.*
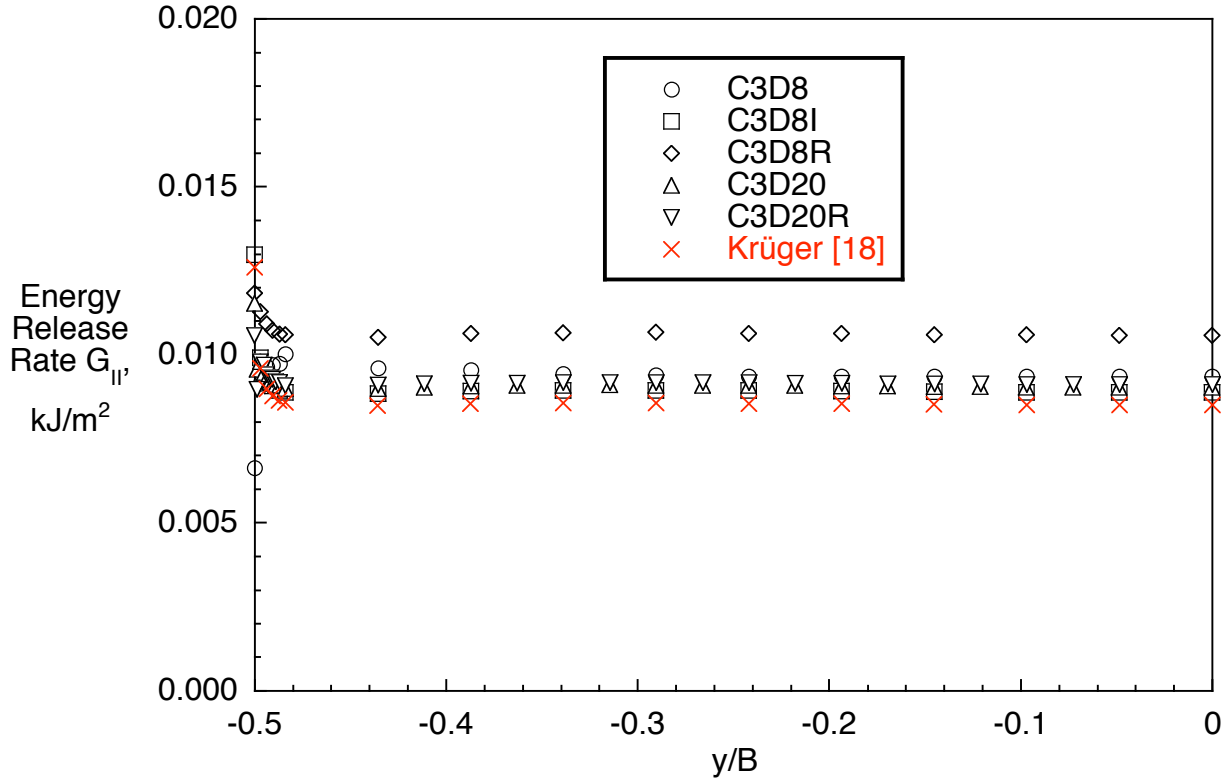
Figure 25. *Influence of ABAQUS® element selection on computed mode II strain energy release rate distribution across the width of a SLB specimen with UD32 layup.*
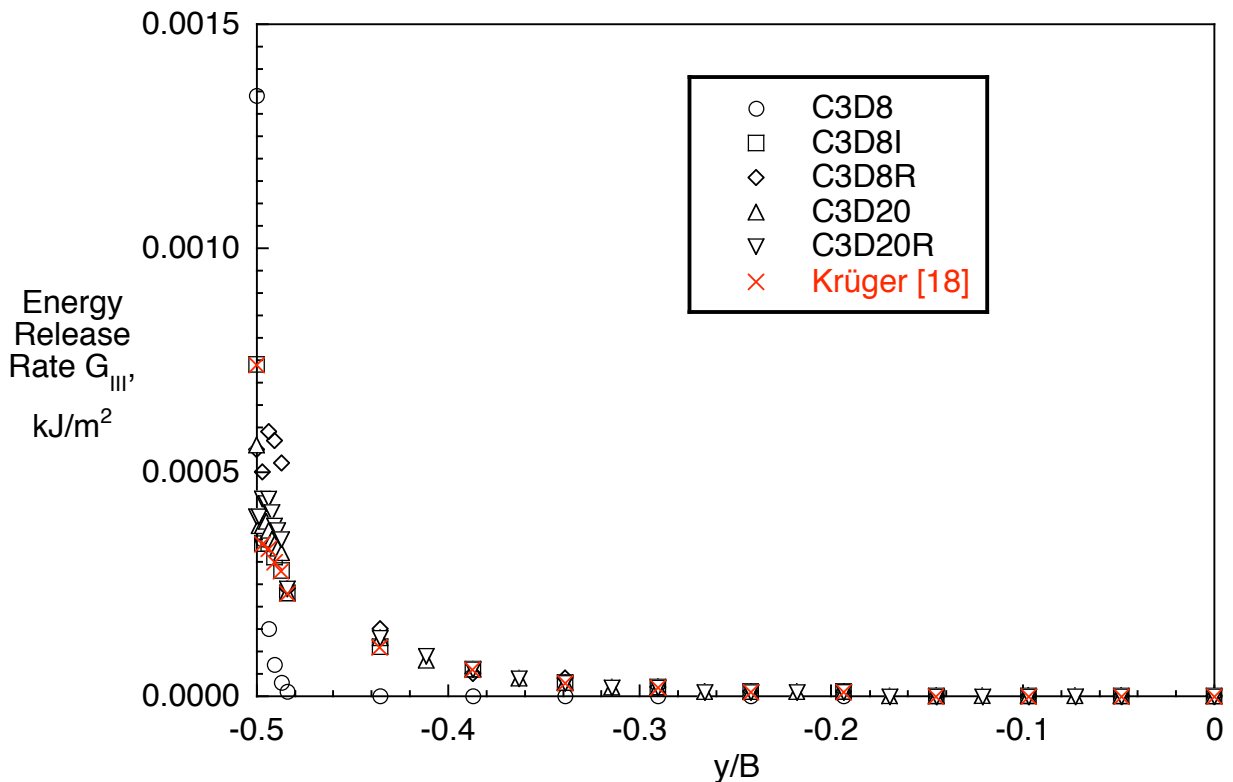
Figure 26. *Influence of ABAQUS® element selection on computed mode III strain energy release rate distribution across the width of a SLB specimen with UD32 layup.*

36
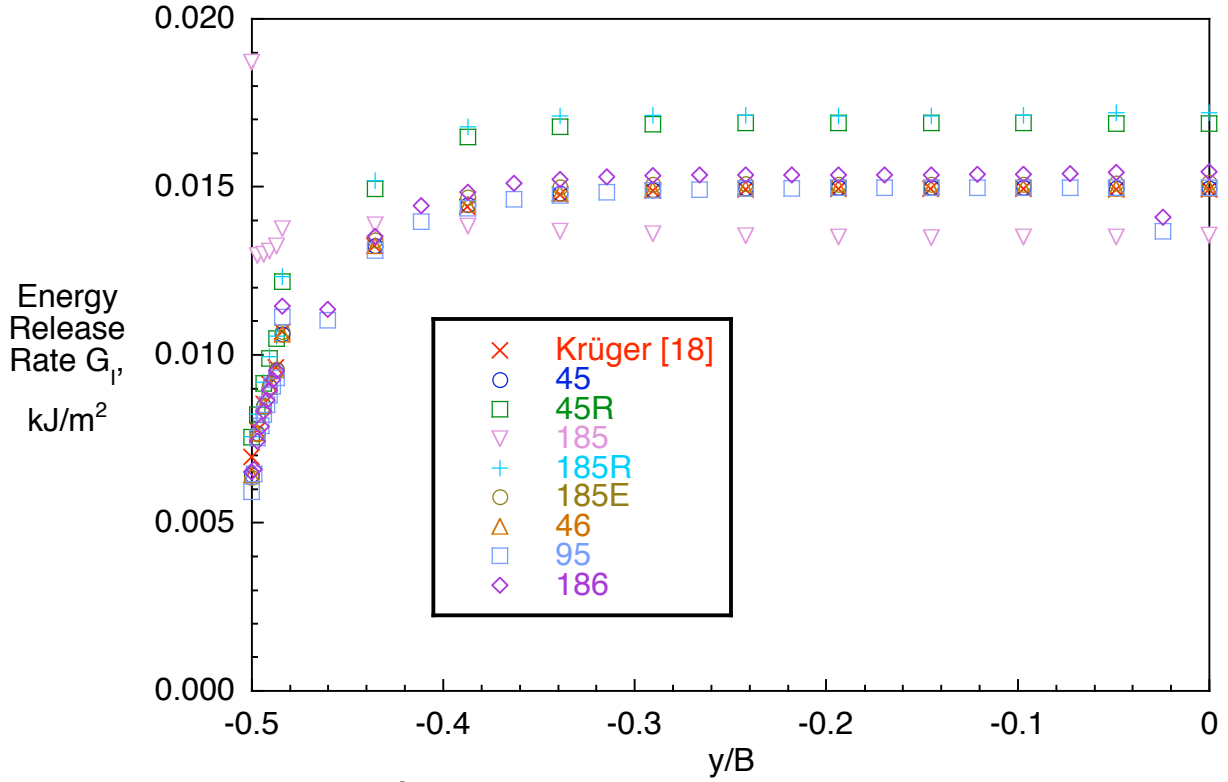
Figure 27. *Influence of ANSYS® element selection on computed mode I strain energy release rate distribution across the width of a SLB specimen with UD32 layup.*
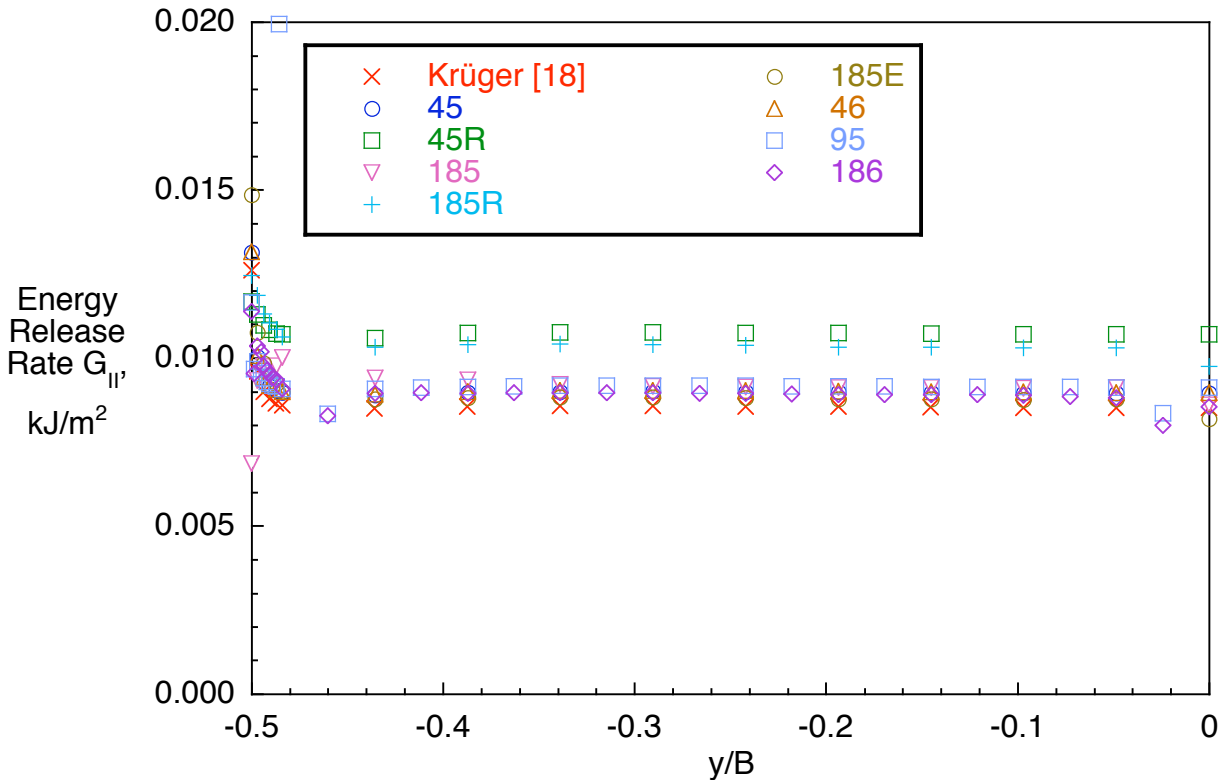
Figure 28. *Influence of ANSYS® element selection on computed mode II strain energy release rate distribution across the width of a SLB specimen with UD32 layup.*
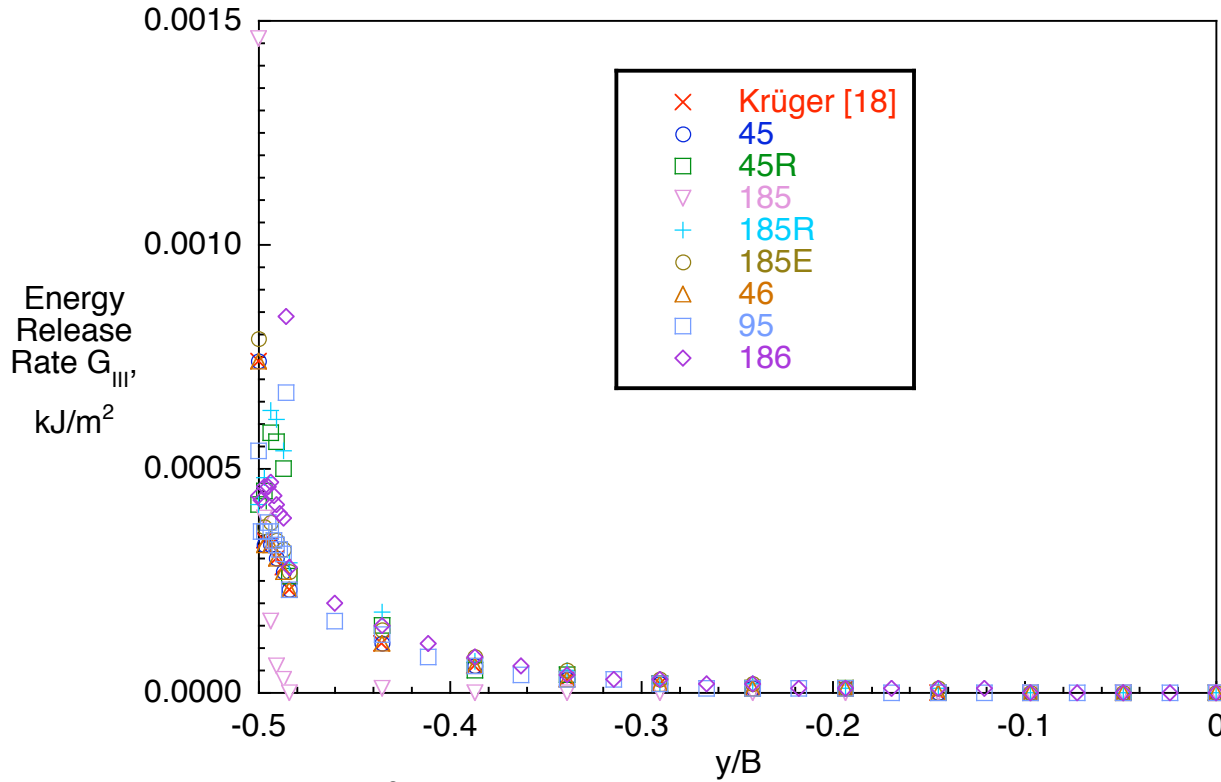
Figure 29. *Influence of ANSYS® element selection on computed mode III strain energy release rate distribution across the width of a SLB specimen with UD32 layup.*
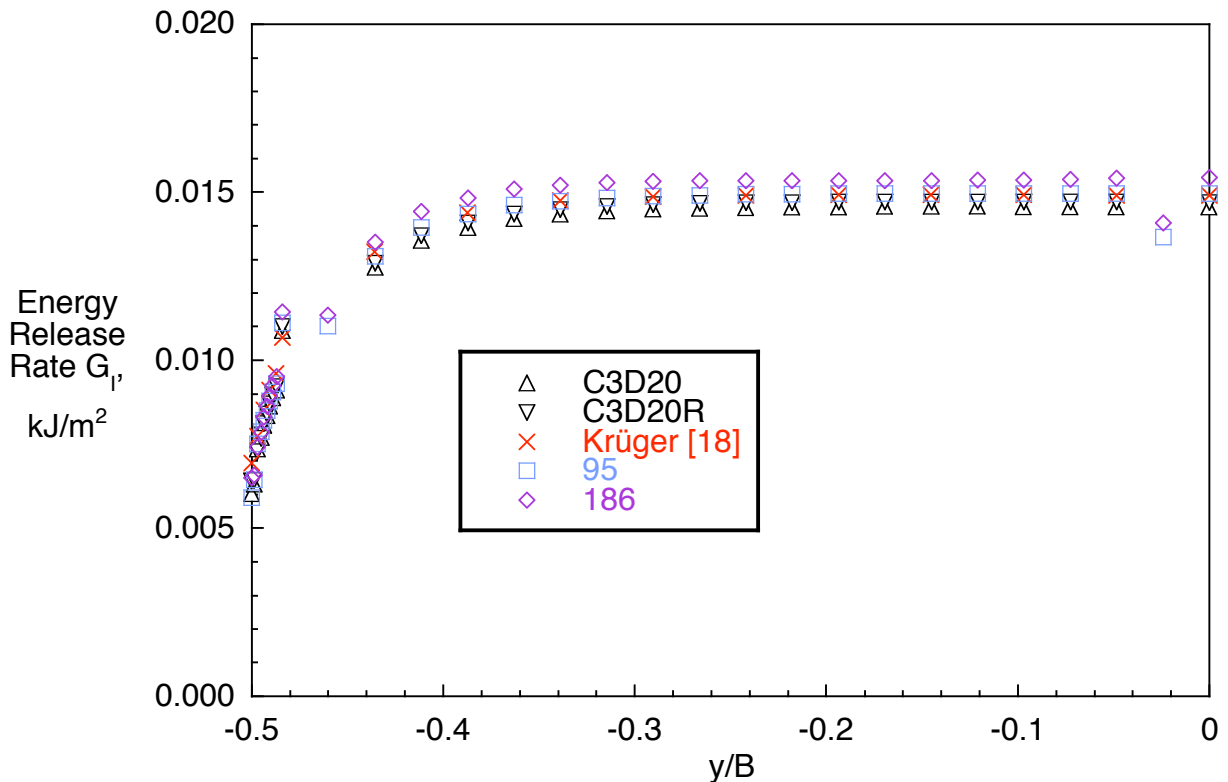
Figure 30. *Computed mode I strain energy release rate distribution across the width of a SLB specimen with UD32 layup modeled with twenty-node solid elements.*
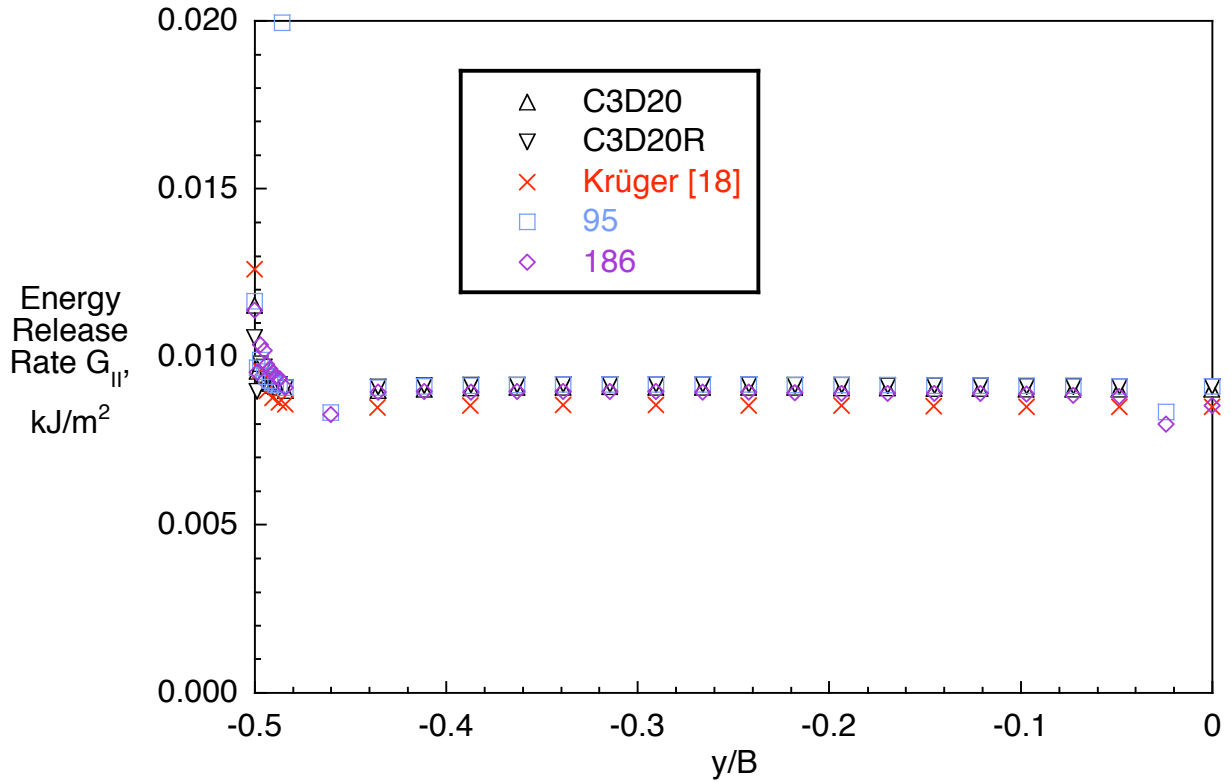
Figure 31. *Computed mode II strain energy release rate distribution across the width of a SLB specimen with UD32 layup modeled with twenty-node solid elements.*
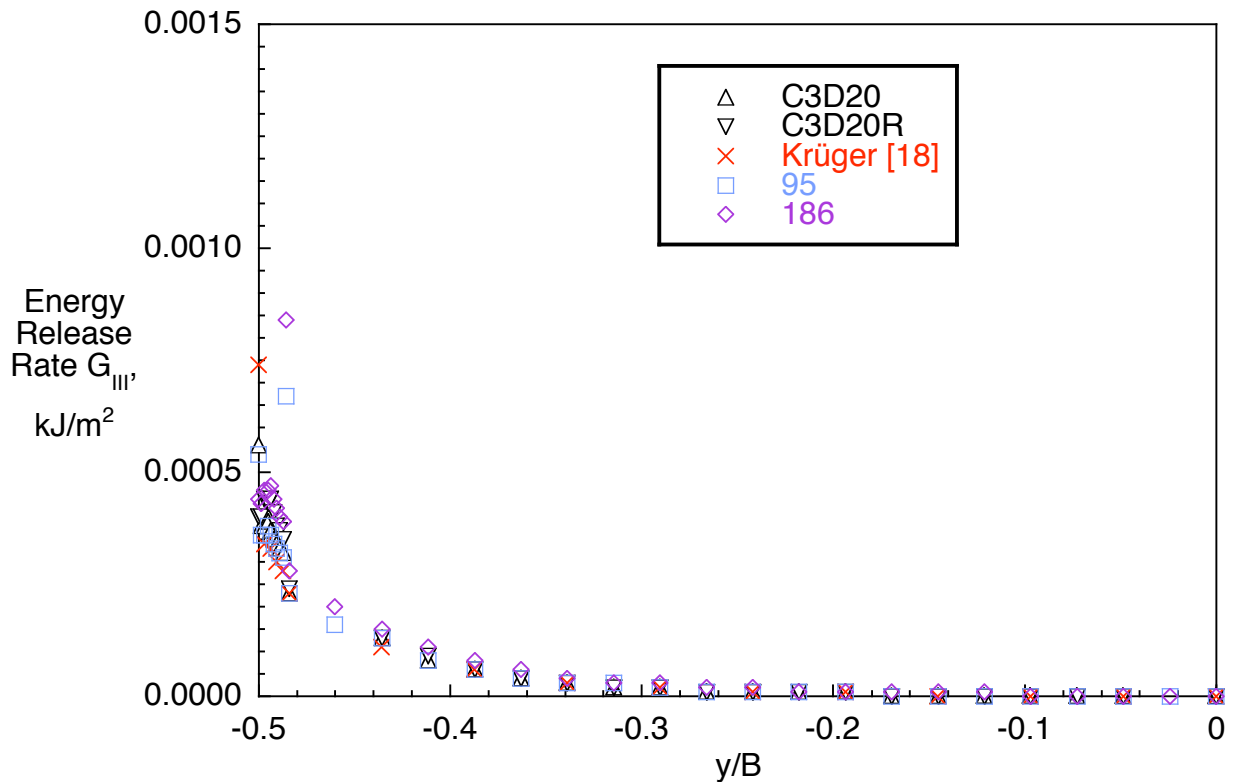
Figure 32. *Computed mode III strain energy release rate distribution across the width of a SLB specimen with UD32 layup modeled with twenty-node solid elements.*
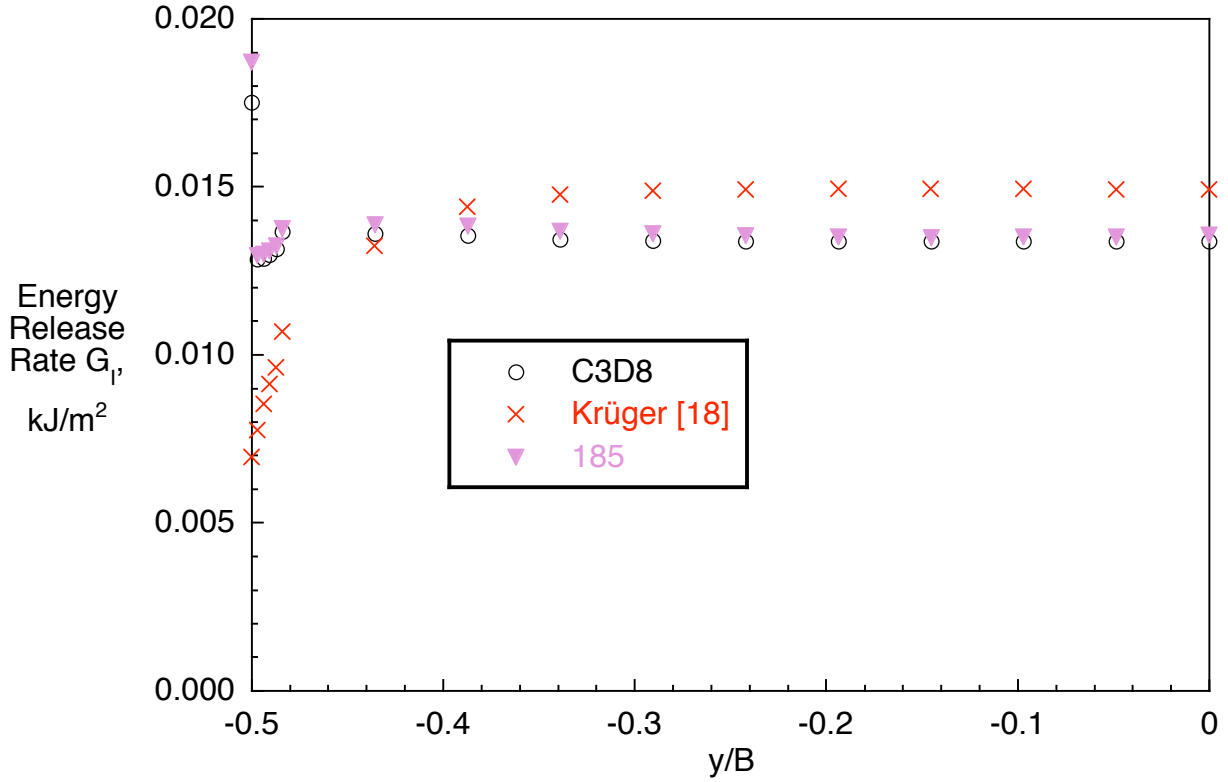
Figure 33. *Computed mode I strain energy release rate distribution across the width of a SLB specimen with UD32 layup modeled with solid eight-node brick elements.*
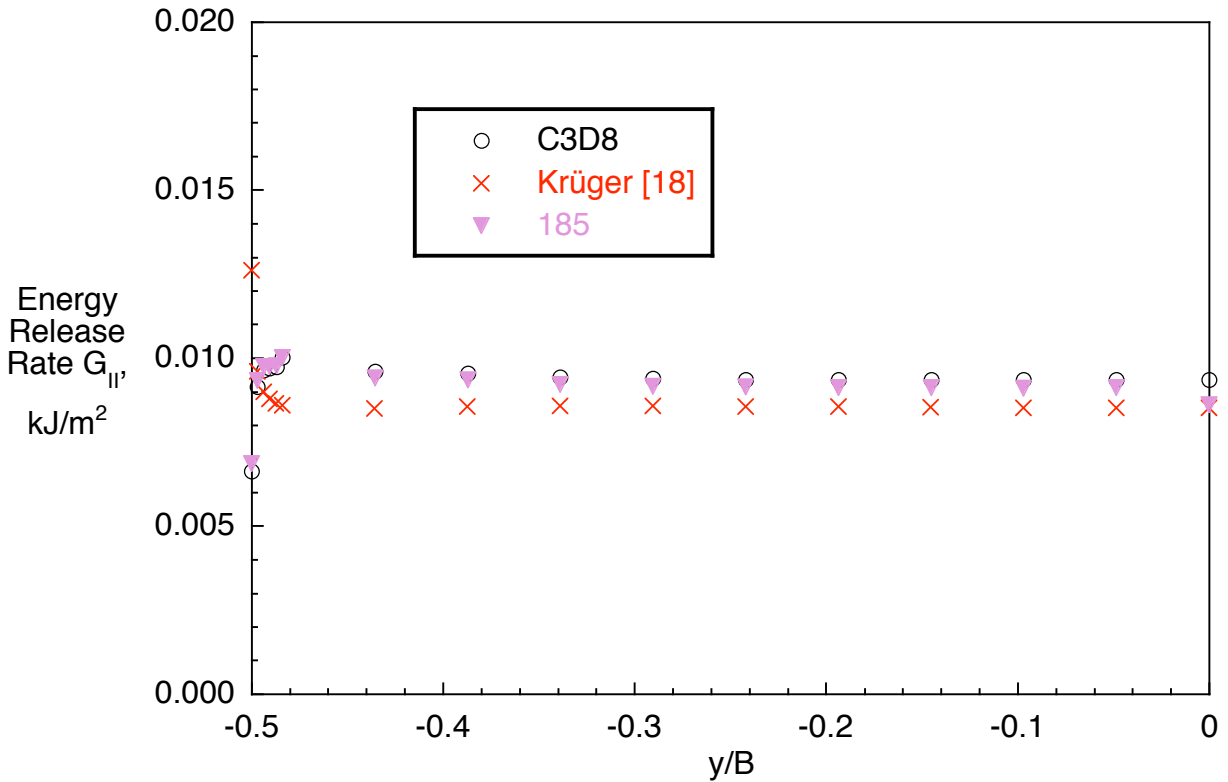
Figure 34. *Computed mode II strain energy release rate distribution across the width of a SLB specimen with UD32 layup modeled with solid eight-node brick elements.*

40
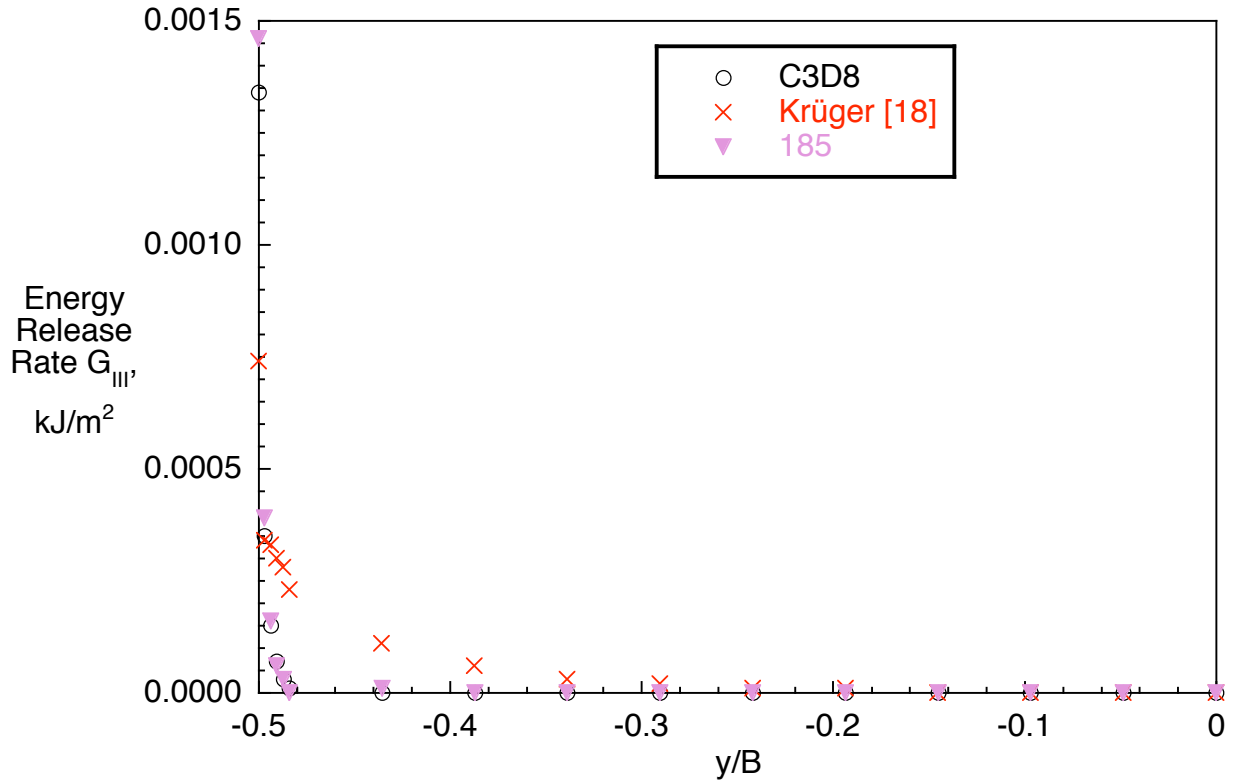
Figure 35. *Computed mode III strain energy release rate distribution across the width of a SLB specimen with UD32 layup modeled with solid eight-node brick elements.*
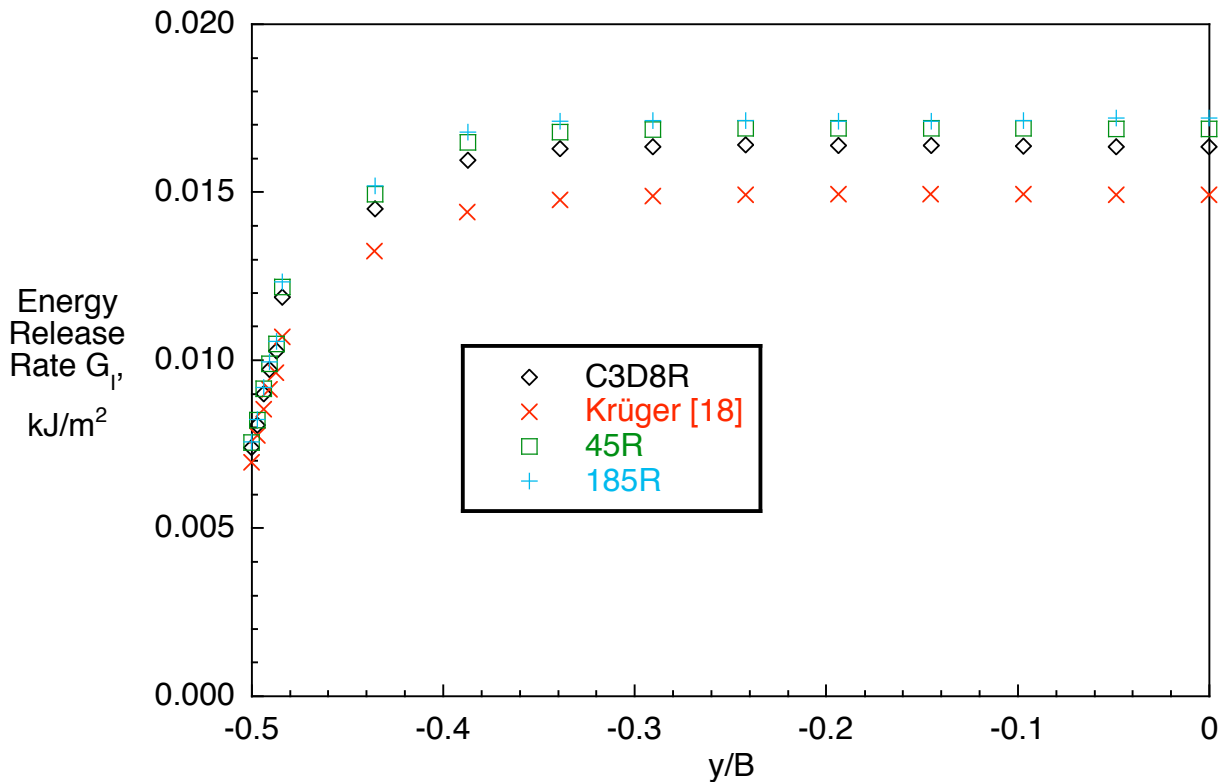
Figure 36. *Computed mode I strain energy release rate distribution across the width of a SLB specimen with UD32 layup modeled with reduced integration eight-node brick elements.*

41
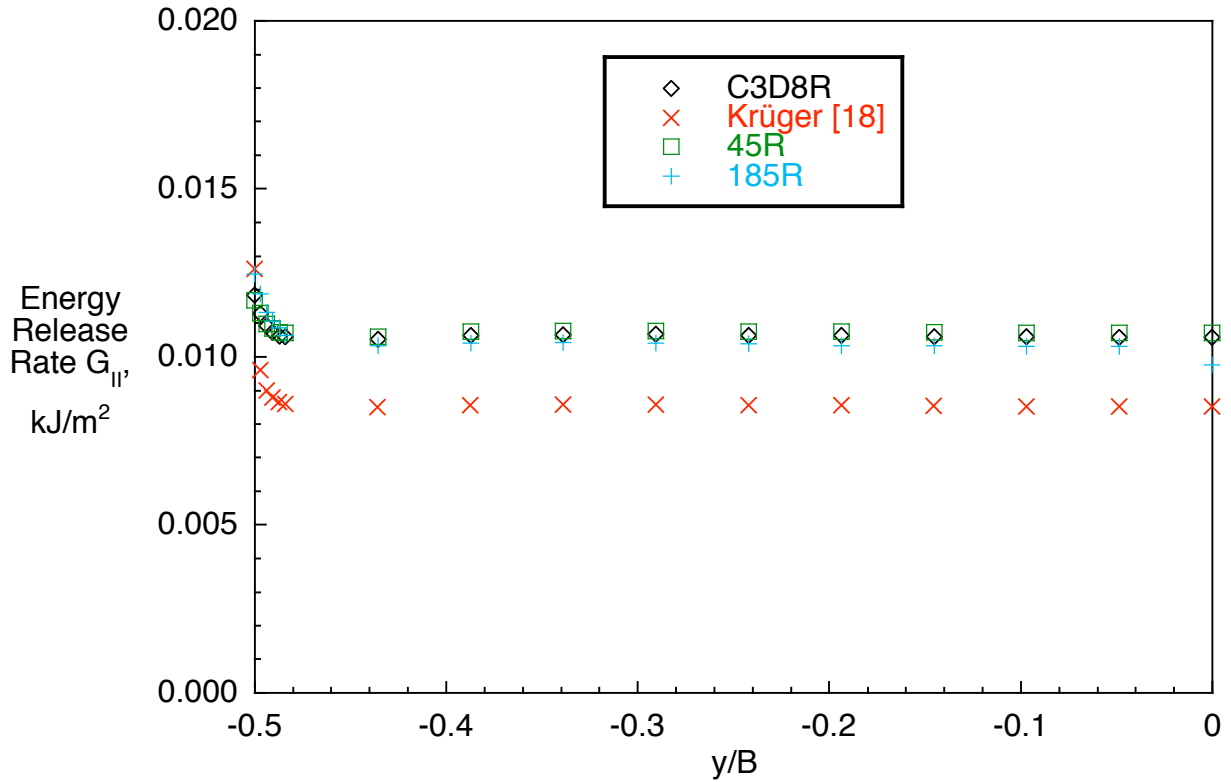
Figure 37. *Computed mode II strain energy release rate distribution across the width of a SLB specimen with UD32 layup modeled with reduced integration eight-node brick elements.*
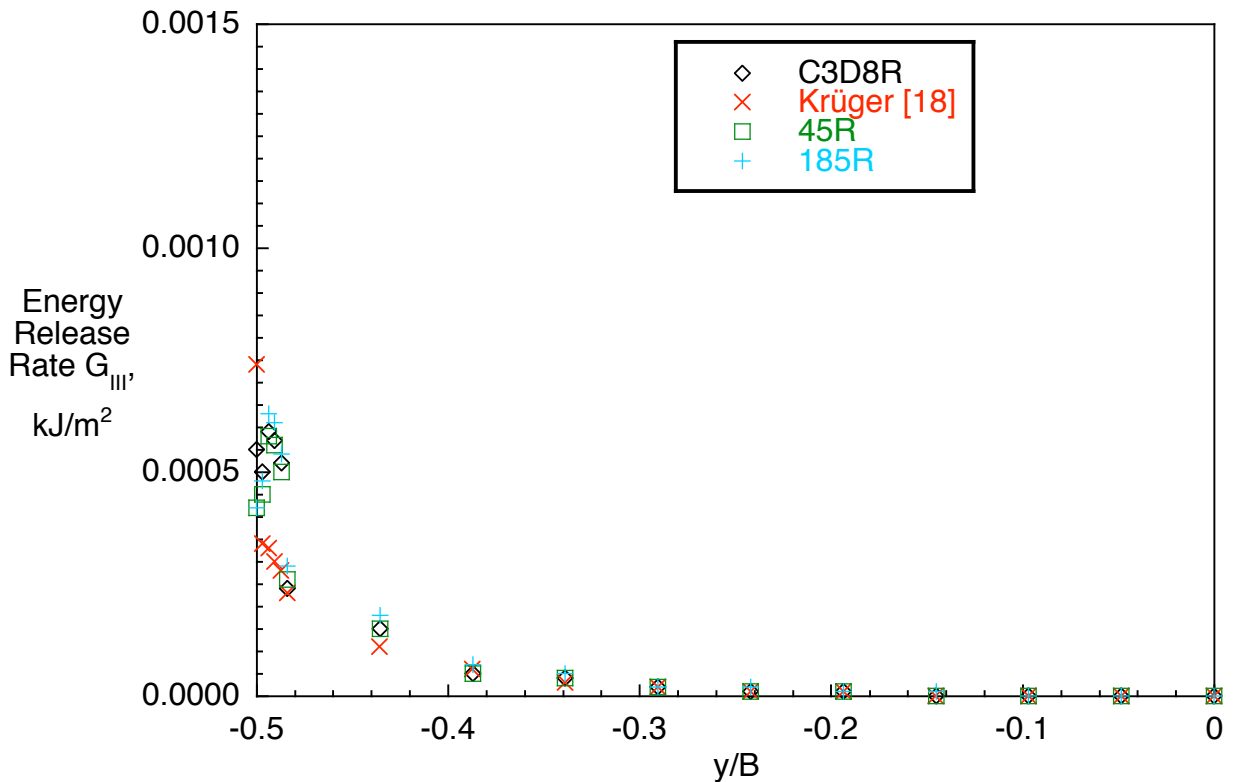
Figure 38. *Computed mode III strain energy release rate distribution across the width of a SLB specimen with UD32 layup modeled with reduced integration eight-node brick elements.*
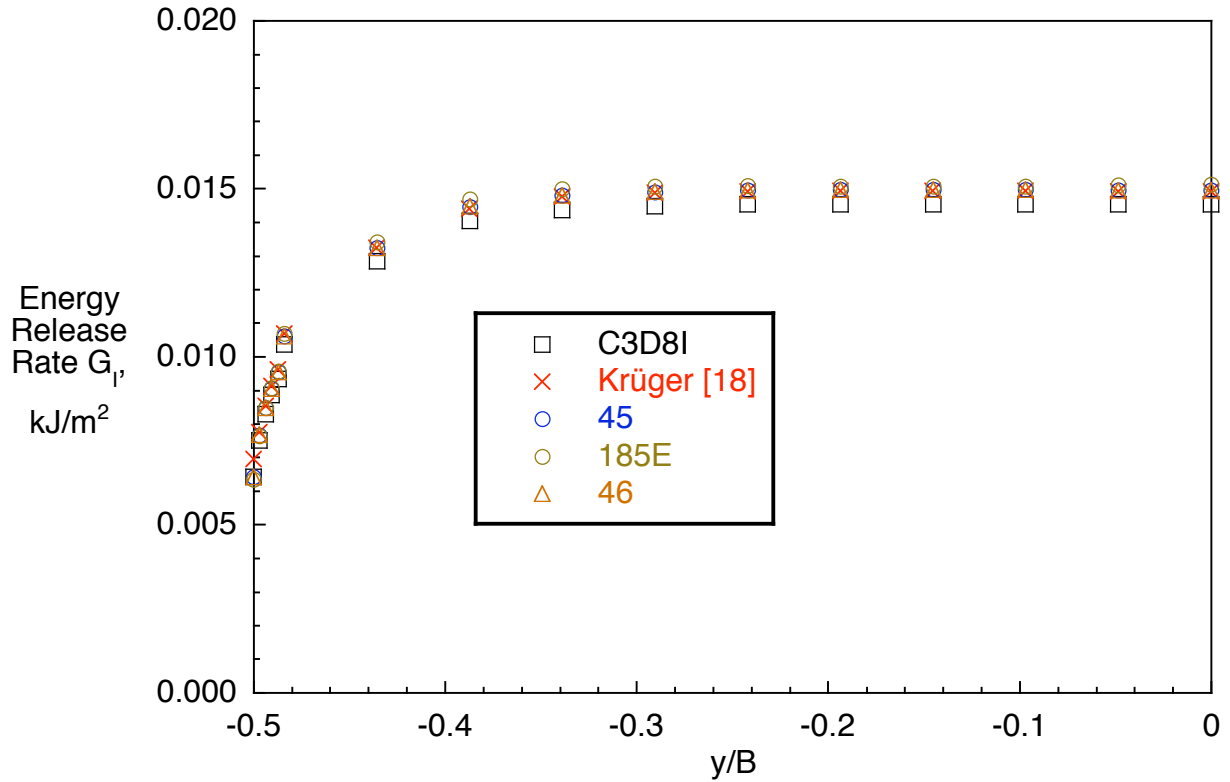
Figure 39. *Computed mode I strain energy release rate distribution across the width of a SLB specimen with UD32 layup modeled with incompatible mode eight-node brick elements.*
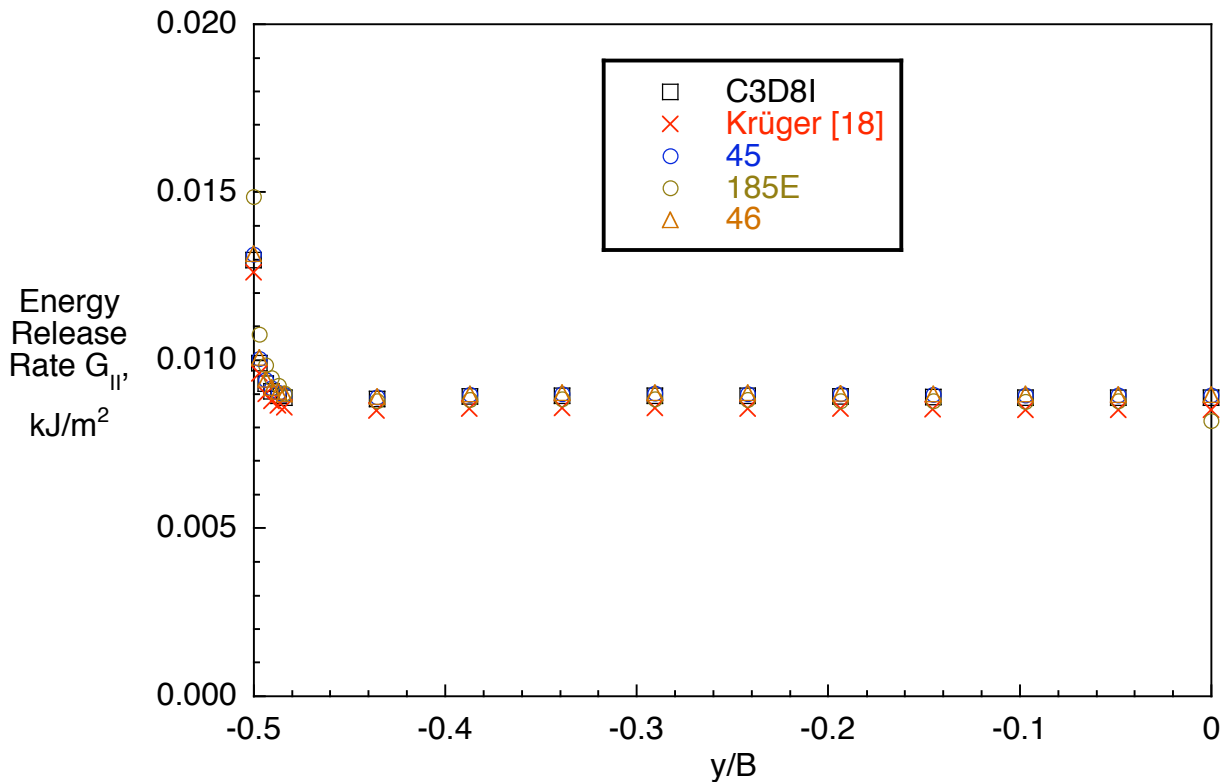
Figure 40. *Computed mode II strain energy release rate distribution across the width of a SLB specimen with UD32 layup modeled with incompatible mode eight-node brick elements.*
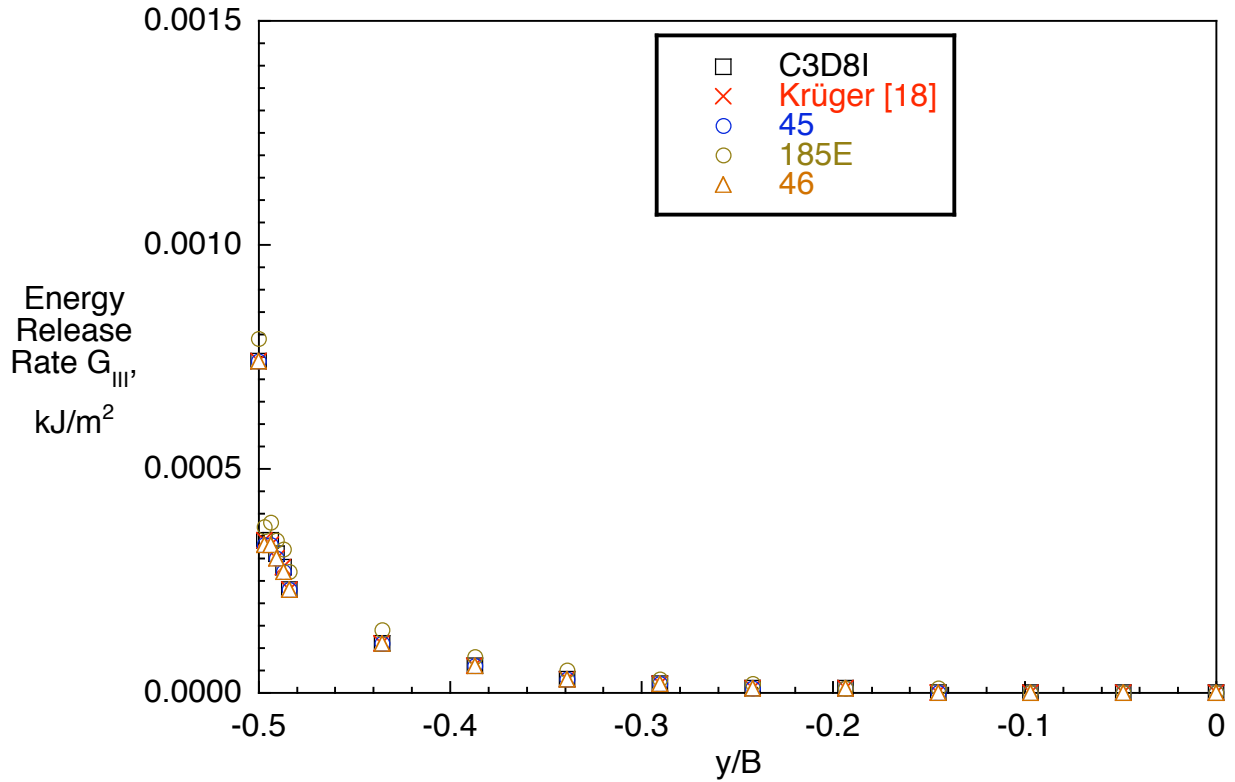
Figure 41. *Computed mode I strain energy release rate distribution across the width of a SLB specimen with UD32 layup modeled with incompatible mode eight-node brick elements.*
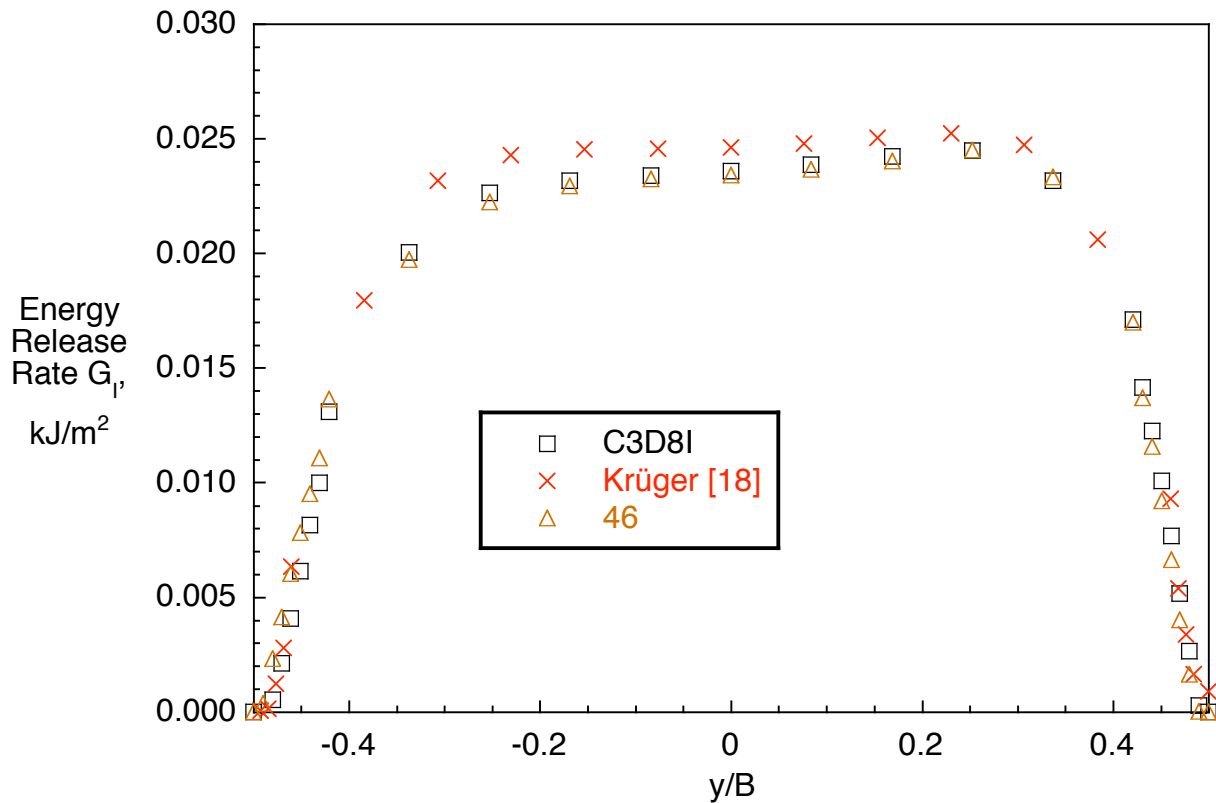
Figure 42. *Influence of FE software on computed mode I strain energy release rate distribution across the width of SLB specimen with D±30 layup.*
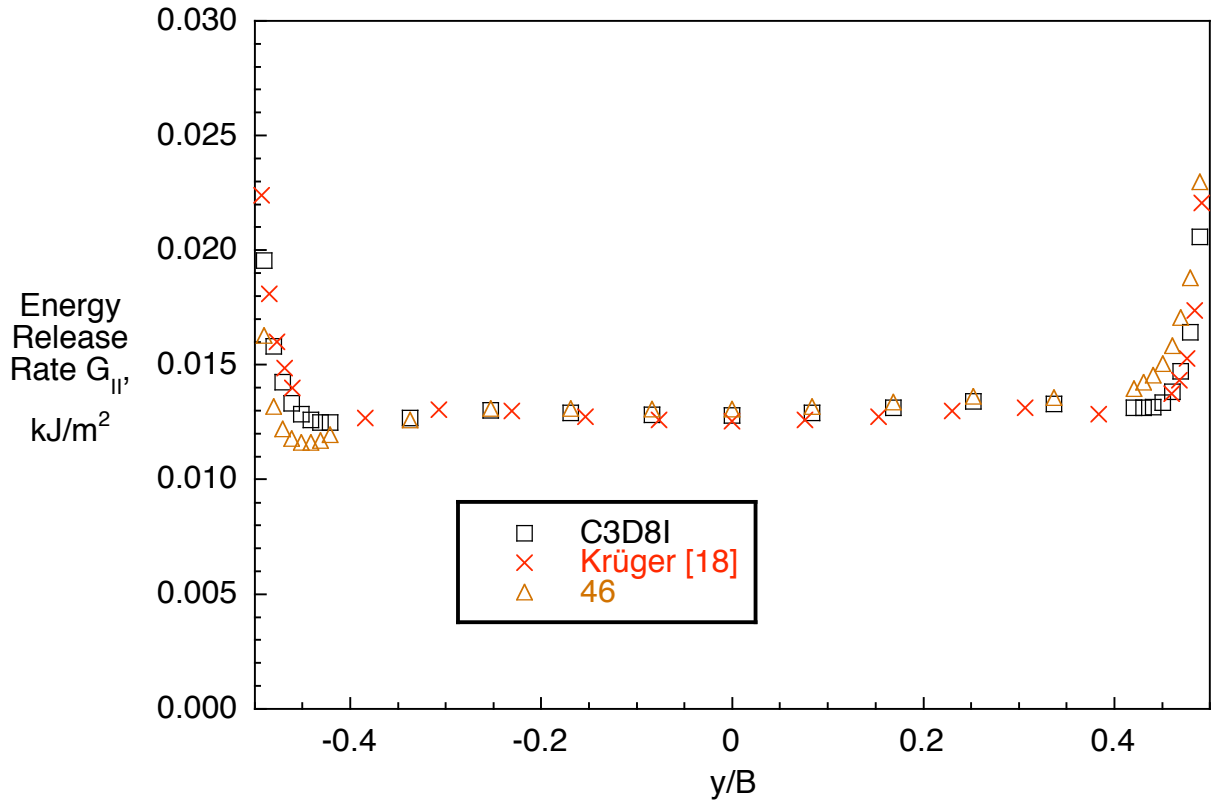
Figure 43. *Influence of FE software on computed mode II strain energy release rate distribution across the width of SLB specimen with D±30 layup.*
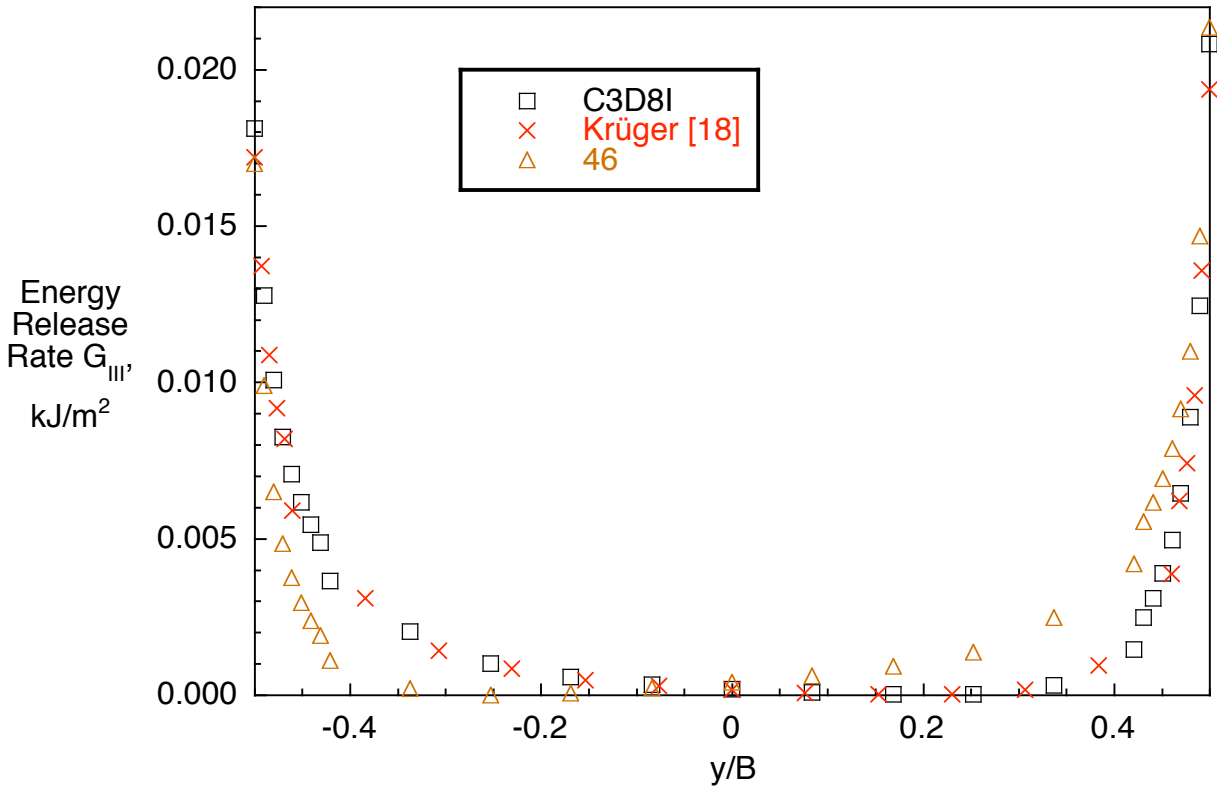
Figure 44. *Influence of FE software on computed mode III strain energy release rate distribution across the width of SLB specimen with D±30 layup.*

45
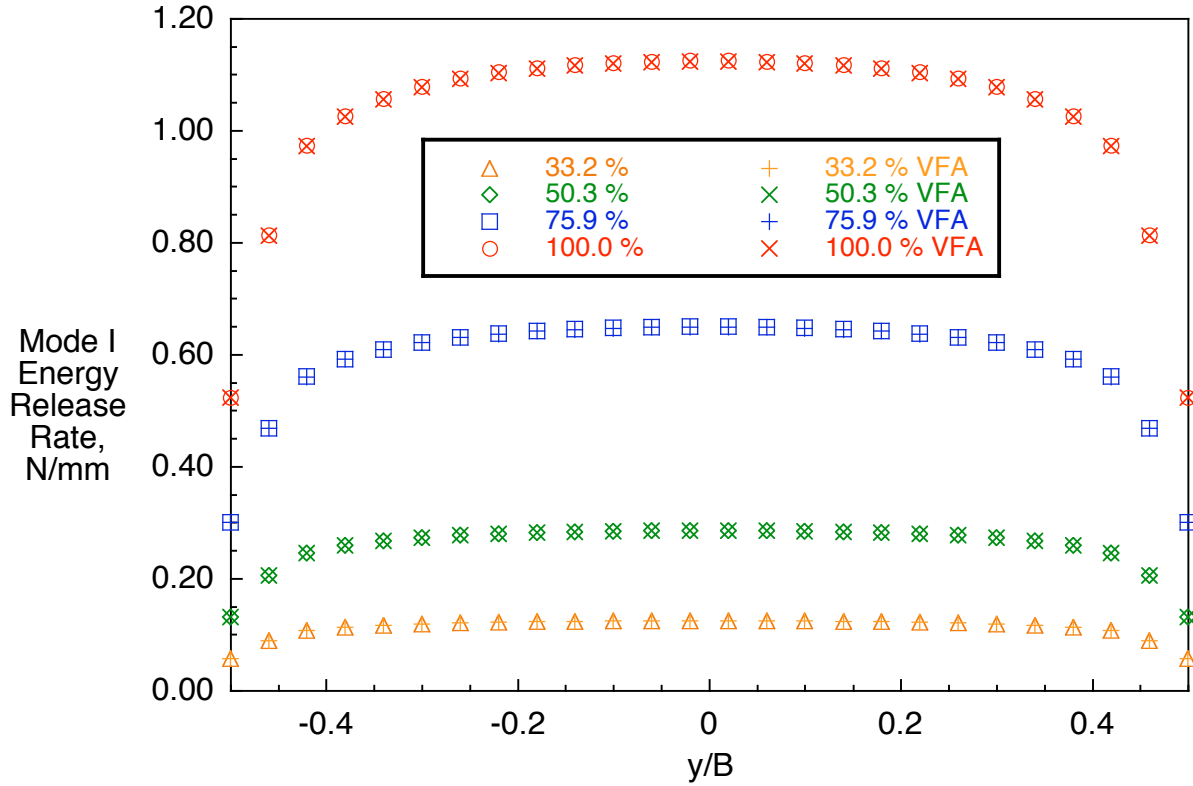
Figure 45. *Computed strain energy release rate distribution across the width of a DCB specimen for different load increments.*
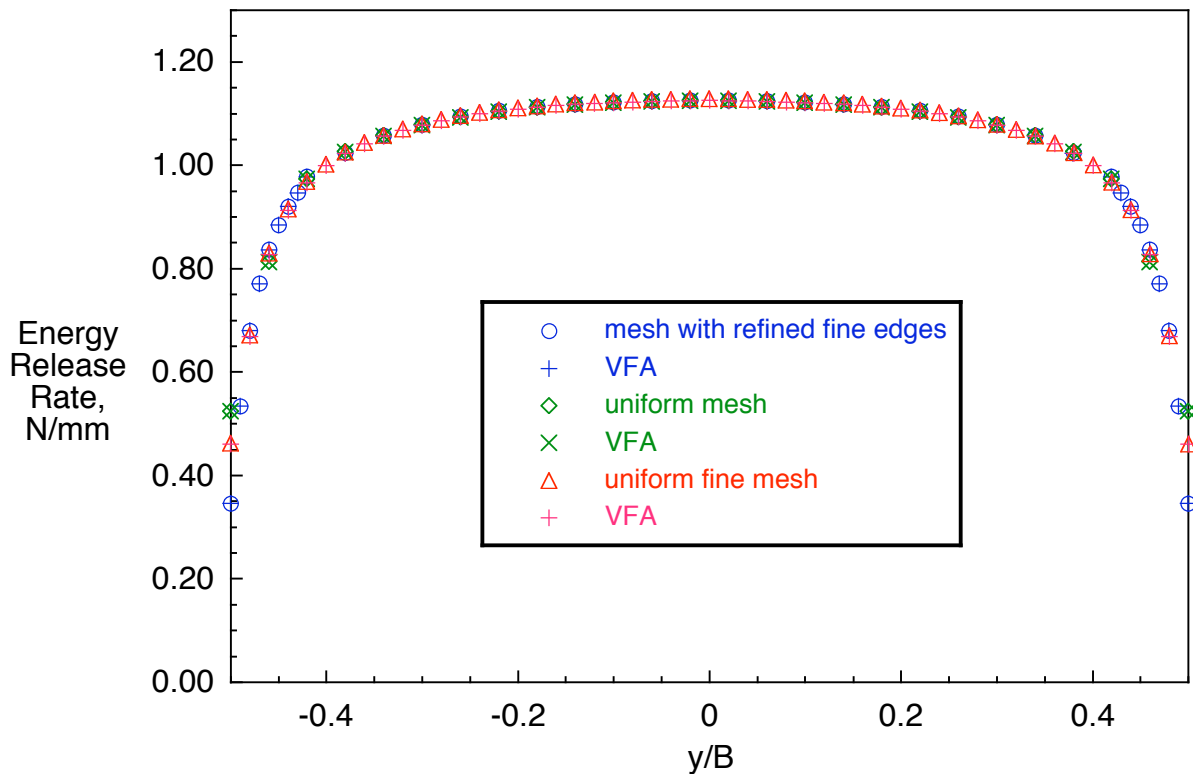
Figure 46. *Computed strain energy release rate distribution across the width of a DCB specimen for different models.*
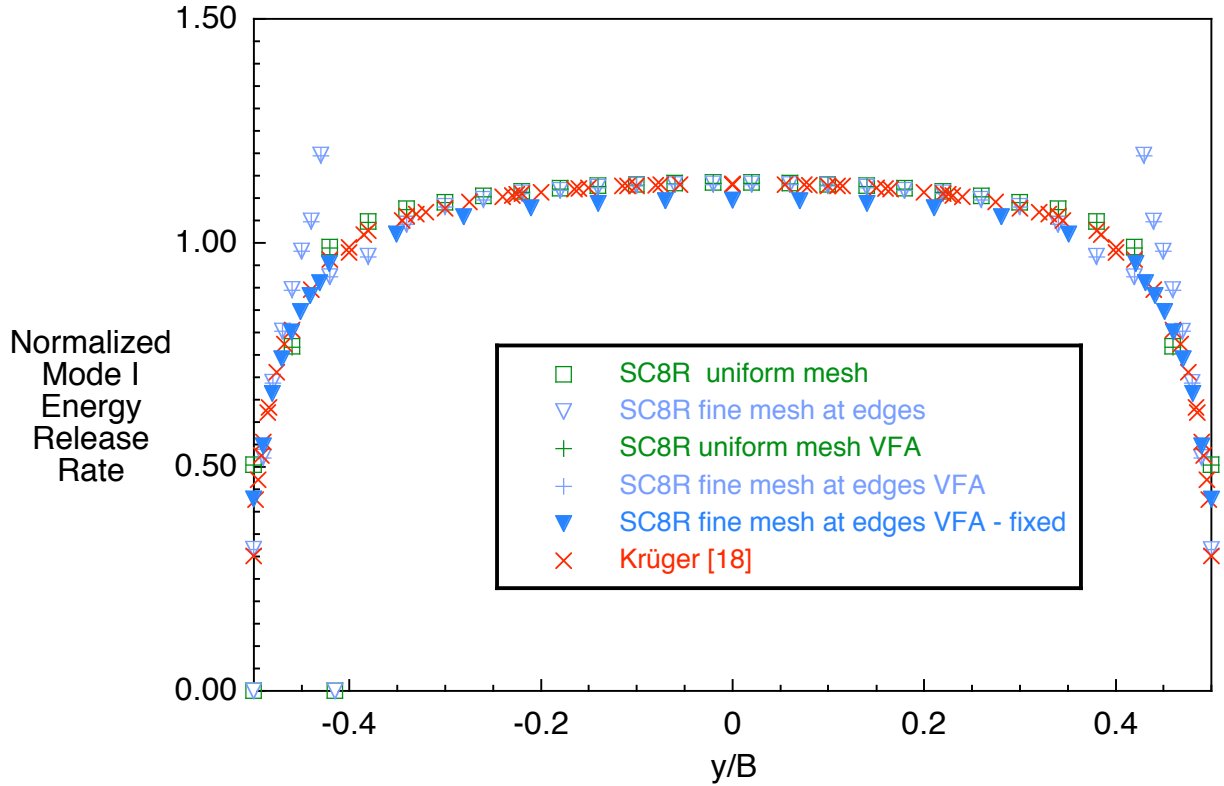
Figure 47. *Computed strain energy release rate distribution across the width of a DCB specimen for continuum shell elements.*
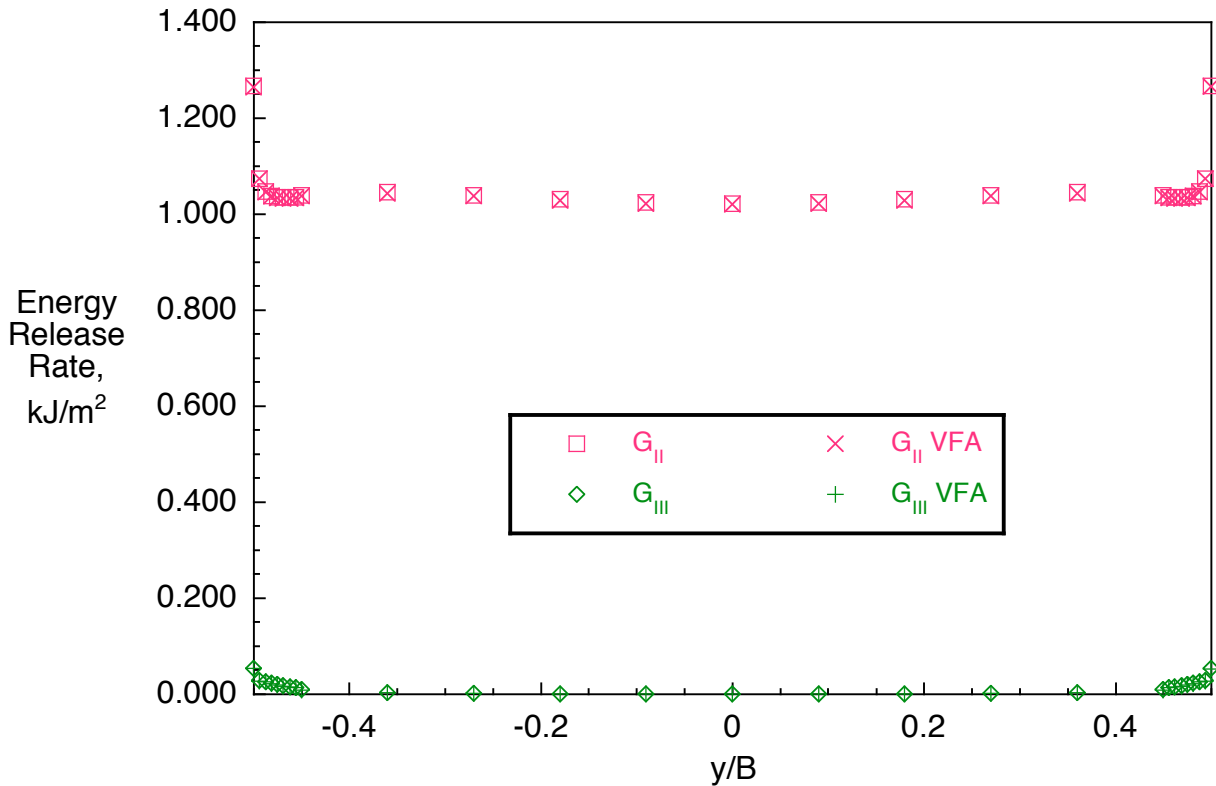
Figure 48. *Computed mixed mode strain energy release rate distributions across the width of an ENF specimen.*
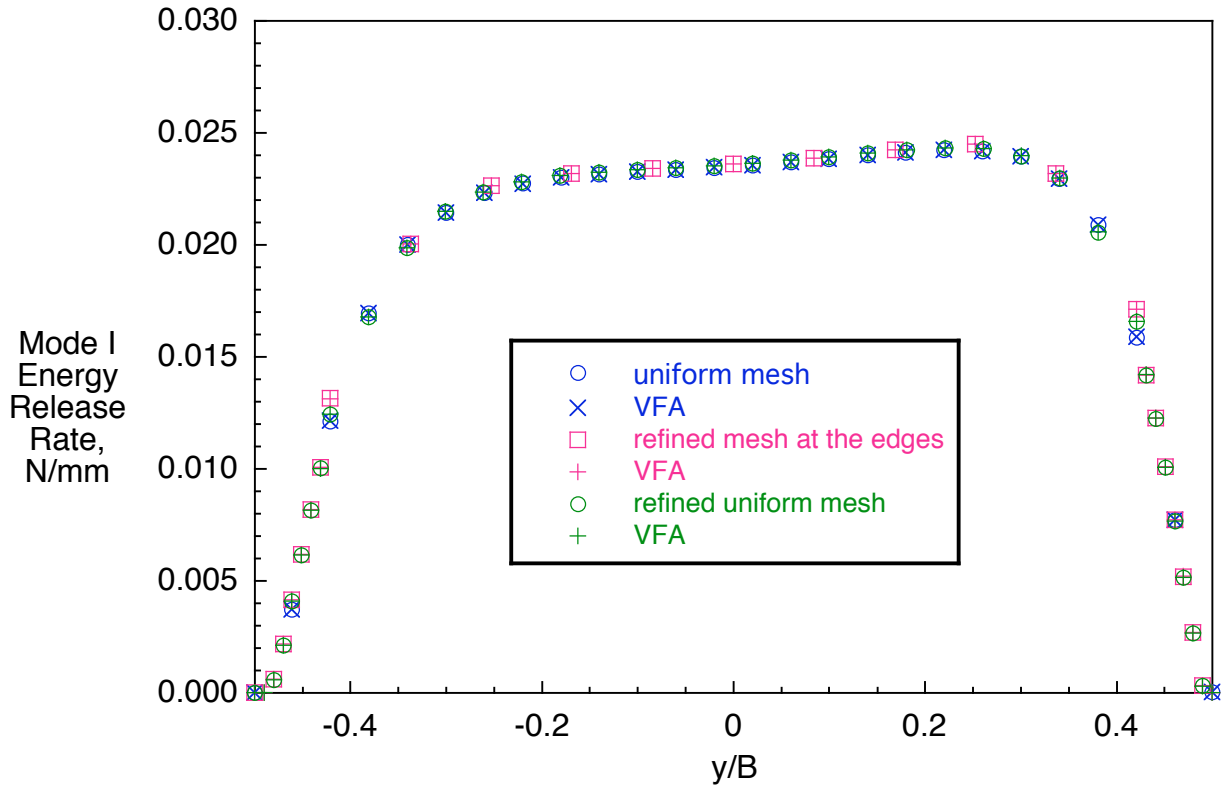
Figure 49. *Computed mode I strain energy release rate distribution across the width of a SLB specimen for different models.*
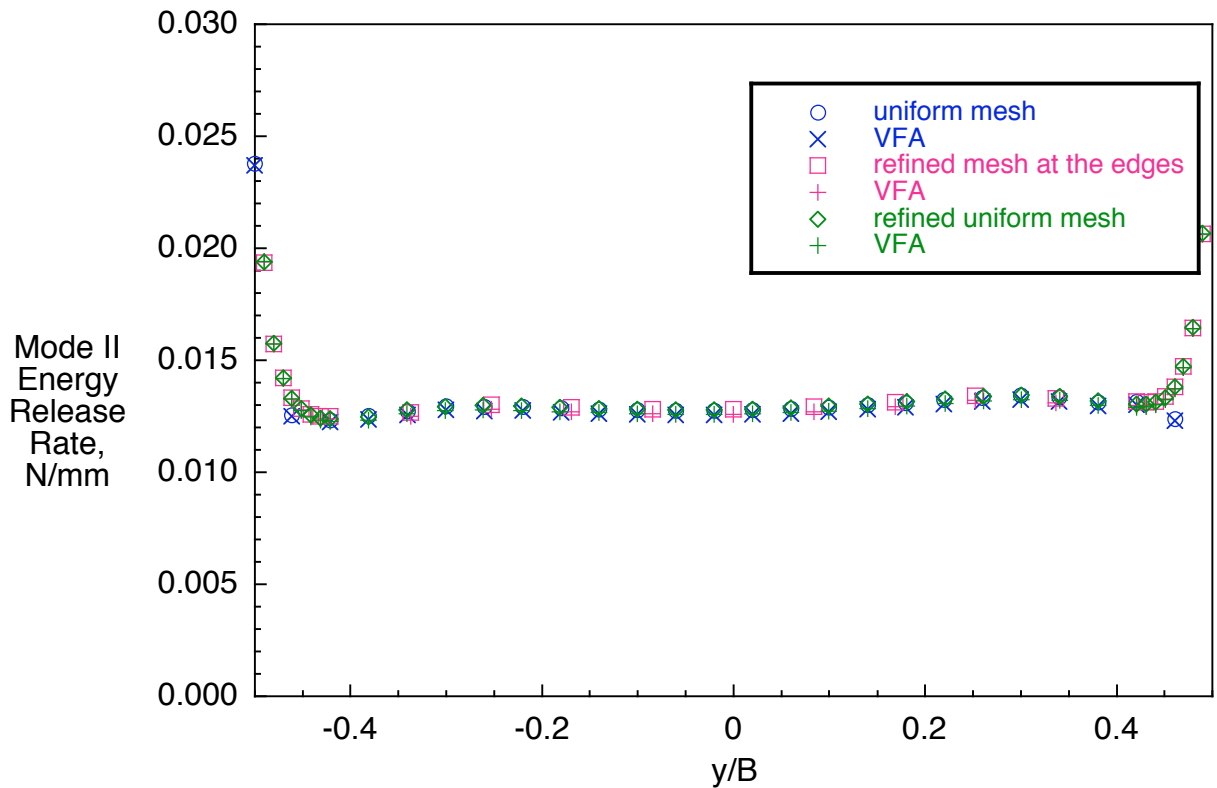
Figure 50. *Computed mode II strain energy release rate distribution across the width of a SLB specimen for different models.*

Figure 51. *Computed moe III strain energy release rate distribution across the width of a SLB specimen for different models.*

1. REPORT DATE *(DD-MM-YYYY)*	2. REPORT TYPE	3. DATES COVERED *(From - To)*
01- 10 - 2006	Contractor Report	

4. TITLE AND SUBTITLE	5a. CONTRACT NUMBER
Influence of Finite Element Software on Energy Release Rates Computed Using the Virtual Crack Closure Technique	NAS1-02117
	5b. GRANT NUMBER
	5c. PROGRAM ELEMENT NUMBER

6. AUTHOR(S)	5d. PROJECT NUMBER
Krueger, Ronald	
Goetze, Dirk	5e. TASK NUMBER
	1002
	5f. WORK UNIT NUMBER

7. PERFORMING ORGANIZATION NAME(S) AND ADDRESS(ES)	8. PERFORMING ORGANIZATION REPORT NUMBER
NASA Langley Research Center National Institute of Aerospace (NIA) Hampton, VA 23681-2199 100 Exploration Way Hampton, VA 23666	NIA Report No. 2006-06

9. SPONSORING/MONITORING AGENCY NAME(S) AND ADDRESS(ES)	10. SPONSOR/MONITOR'S ACRONYM(S)
National Aeronautics and Space Administration Washington, DC 20546-0001	NASA
	11. SPONSOR/MONITOR'S REPORT NUMBER(S)
	NASA/CR-2006-214523

12. DISTRIBUTION/AVAILABILITY STATEMENT
Unclassified - Unlimited
Subject Category 24
Availability: NASA CASI (301) 621-0390

13. SUPPLEMENTARY NOTES
Langley Technical Monitor: Jonathan Ransom
An electronic version can be found at http://ntrs.nasa.gov

14. ABSTRACT

Strain energy release rates were computed along straight delamination fronts of Double Cantilever Beam, End-Notched Flexure and Single Leg Bending specimens using the Virtual Crack Closure Technique (VCCT). The results were based on finite element analyses using ABAQUS® and ANSYS® and were calculated from the finite element results using the same post-processing routine to assure a consistent procedure. Mixed-mode strain energy release rates obtained from post-processing finite element results were in good agreement for all element types used and all specimens modeled. Compared to previous studies, the models made of solid twenty-node hexahedral elements and solid eight-node incompatible mode elements yielded excellent results. For both codes, models made of standard brick elements and elements with reduced integration did not correctly capture the distribution of the energy release rate across the width of the specimens for the models chosen. The results suggested that element types with similar formulation yield matching results independent of the finite element software used. For comparison, mixed-mode strain energy release rates were also calculated within ABAQUS®/Standard using the VCCT for ABAQUS® add on. For all specimens modeled, mixed-mode strain energy release rates obtained from ABAQUS® finite element results using post-processing were almost identical to results calculated using the VCCT for ABAQUS® add on.

15. SUBJECT TERMS

Finite Element Analysis; Computational Fracture Mechanics; Virtual Crack Closure Technique; Composite Material; Fracture Toughness Specimens

16. SECURITY CLASSIFICATION OF:			17. LIMITATION OF ABSTRACT	18. NUMBER OF PAGES	19a. NAME OF RESPONSIBLE PERSON
a. REPORT	b. ABSTRACT	c. THIS PAGE			STI Help Desk (email: help@sti.nasa.gov)
					19b. TELEPHONE NUMBER *(Include area code)*
U	U	U	UU	54	(301) 621-0390